Davies, P. J., McKenzie, J. A., Palmer-Julson, A., et al., 1991
Proceedings of the Ocean Drilling Program, Initial Reports, Vol. 133

14. SITE 821[1]

Shipboard Scientific Party[2]

HOLE 821A

Date occupied: 15 September 1990

Date departed: 16 September 1990

Time on hole: 1 day, 13 hr, 40 min

Position: 16°38.793′S, 146°17.376′E

Bottom felt (rig floor; m, drill-pipe measurement): 224.1

Distance between rig floor and sea level (m): 11.35

Water depth (drill-pipe measurement from sea level, m): 212.7

Total depth (rig floor; m): 624.1

Penetration (m): 400.0

Number of cores (including cores with no recovery): 43

Total length of cored section (m): 400.0

Total core recovered (m): 382.9

Core recovery (%): 95.7

Oldest sediment recovered:
Depth (mbsf): 400.0
Nature: lithified silty to sandy calcareous clayey mixed sediment
Age: Pleistocene

HOLE 821B

Date occupied: 16 September 1990

Date departed: 17 September 1990

Time on hole: 13 hr

Position: 16°38.794′S, 146°17.366′E

Bottom felt (rig floor; m, drill-pipe measurement): 222.7

Distance between rig floor and sea level (m): 11.35

Water depth (drill-pipe measurement from sea level, m): 211.6

Total depth (rig floor; m): 388.9

Penetration (m): 165.9

Number of cores (including cores with no recovery): 20

Total length of cored section (m): 165.9

Total core recovered (m): 167.4

Core recovery (%): 100.9

Oldest sediment recovered:
Depth (mbsf): 165.9
Nature: bioclastic wackestone
Age: Pleistocene

Principal results: Site 821 is located in 212 m of water in Grafton Passage, on the continental slope to the east of Cairns. This site is the proximal and shallowest end-member of a shelf-edge transect aimed at defining [1]the relationships among changes in sea level, sediment [2]sequences, and seismic geometries and, in particular, the response of a slope sequence to rapid global changes in sea level. Hole 821A was cored with the advanced piston corer (APC) to 145.9 mbsf and the extended-core barrel (XCB) corer to 400 mbsf and had a final average recovery of 95%; Hole 821B was cored with the APC to 165.9 mbsf, with 100% recovery. As at Sites 819 and 820, the section to 400 mbsf at Site 821 is an expanded Pleistocene section. Nannofossils indicate an age of 1.27–1.48 Ma for the bottom of the hole. Preservation of planktonic foraminifers and nannofossils varies from near pristine in clayey intervals to overgrown in sandy intervals. Benthic foraminifers indicate a depth range of neritic to upper bathyal for the sequence at Site 821. The pattern of variation in sedimentation rates at Site 821 is similar to that at Site 820. Middle Pleistocene rates of 28.2 cm/k.y. are succeeded by 12.2 cm/k.y. between 0.930 and 0.465 Ma, 49.2 cm/k.y. in the succeeding 190 k.y., and 10.2 cm/k.y. from 0.275 Ma to the present. However, in comparison to Site 820, the locus of increased sedimentation had shifted to Site 821 by the late Pleistocene, coincident with the aggradation phase of sedimentation.

Drilling at Site 821 has led to the identification of five lithostratigraphic units. Units I and II are aggradational while Units III to V are thought to be progradational.

1. *Unit I:* depth, 0–145.5 mbsf; age, <0.93 Ma, Holocene to late Pleistocene. Principal sediment types include mixed sediments of siliceous and bioclastic components, calcareous silts and clays, bioclastic and nannofossil oozes and chalks, bioclastic packstones, and *Halimeda* rudstones. With the exception of the uppermost part, the unit is thought to represent a series of rapidly deposited aggradational packages. It is divided into seven subunits.

Subunit IA: Depth, 0–16.5 mbsf; age, <0.275 Ma, Holocene to late Pleistocene. An upward-fining sequence that is a fine to coarse sandy bioclastic/siliciclastic mixed sediment containing large benthic foraminifers, coralline algae, and bryozoans at the base and grades upward into clays with bioclasts and nannofossils.

Subunit IB: depth, 16.5–40.3 mbsf; age, <0.465 Ma, late Pleistocene. Two facies make up the subunit in ascending order: (1) silt to fine sand mixed sediment with bioclasts and molluscan/bryozoan fragments; sometimes the facies is a coarse sandy bioclastic/siliciclastic mixed sediment with large benthic foraminifers, *Halimeda,* coralline algae, and pectinids and other mollusks; and (2) calcareous clayey and silty mixed sediment with some bioclasts.

Subunit IC: depth, 40.3–66.5 mbsf; age, 0.275–0.465 Ma, late Pleistocene. An upward-fining sequence composed of clay or silty fine to medium bioclastic and siliciclastic sands grading upward into a homogeneous silty bioclastic or nannofossil clay.

Subunit ID: depth, 66.5–88.7 mbsf; age, 0.275–0.465 Ma, late Pleistocene. A rhythmic alternation of calcareous silty clays and clayey silts above and below a lithified and dolomitized mixed sediment unit.

Subunit IE: depth, 88.7–99.2 mbsf; age, 0.275–0.465 Ma, late Pleistocene. Dolomitized calcareous fine to medium bioclastic sand.

Subunit IF: depth, 99.2–132.1 mbsf; age, 0.275–0.93 Ma, late Pleistocene. The basis of the subunit is a poorly sorted fine to coarse bioclastic sand and bioclastic-nannofossil ooze or chalk. The sequence is repeated three times.

Subunit IG: depth, 132.1–145.5 mbsf; age, 0.475–0.93 Ma, late Pleistocene. This subunit is divided into three parts: (1) a lower lithified *Halimeda* rudstone with molluscan and bryozoan fragments, large benthic foraminifers, and lithoclasts of packstone and wackestone in a mud matrix; (2) calcareous mudstone containing

[1] Davies, P. J., McKenzie, J. A., Palmer-Julson, A., et al., 1991. *Proc. ODP, Init. Repts.,* 133: College Station, TX (Ocean Drilling Program).

[2] Shipboard Scientific Party is as given in list of participants preceding the contents.

sand-sized siliciclastic grains; and (3) at the top a medium to fine sand-sized bioclastic packstone.

2. *Unit II:* depth, 145.5–172.0 mbsf; age, 0.465–0.93 Ma, late Pleistocene. An upward-fining siliciclastic-dominated packstone at the base and a glauconitic and siliciclastic lithified mudstone at the top, perhaps representing a hardground. Sedimentation throughout the unit is low (12 cm/k.y.) compared with the units above and below. The unit is divided into two subunits:

Subunit IIA: depth, 145.5–156.3 mbsf; age, 0.465–0.93 Ma, late Pleistocene. Partially to well-lithified bioclastic packstones are overlain by lithified chalk/mudstone containing glauconite and detrital grains.

Subunit IIB: depth, 156.3–172.0 mbsf; age, 0.465–0.93 Ma, late Pleistocene. Lithified bioclastic/siliciclastic packstones exhibit upward-fining textures and are overlain by a 7-m-thick unit of bioclastic mudstones.

3. *Unit III:* depth, 172.0–215.0 mbsf; age 0.465–1.27 Ma, early Pleistocene. Dolomitized bioclastic wackestone/chalk and bioclastic packstone. Sedimentation rates are relatively high (28.2 cm/k.y.). The unit is composed of two subunits.

Subunit IIIA: depth, 172.0–184.3 mbsf; age, 0.465–0.93 Ma, early Pleistocene. The subunit changes from a lithified dolomitized bioclastic wackestone at the base through a 3-m-thick dolomitized bioclastic packstone to a nannofossil-rich chalk at the top.

Subunit IIIB: depth, 184.3–215.8 mbsf; age, 0.93–1.27 Ma, early Pleistocene. At the base, the subunit is composed of 50 cm of a coarse-grained dolomitized packstone/mixed sediment, which is overlain by bioclastic and nannofossil chalky wackestones with occasional dolomitized packstone/mixed sediment intercalations.

4. *Unit IV:* depth, 215.8–298.8 mbsf; age, between 0.93 and 1.48 Ma, early Pleistocene. Thickly bedded subunits of dolomitized chalk and bioclastic packstones and wackestones. The unit was deposited at a rate of 28 cm/k.y. Four subunits have been recognized.

Subunit IVA: depth, 215.8–246.3 mbsf; age, 0.93–1.27 Ma, early Pleistocene. A basal dolomitized micritic to nannofossil chalk containing siliciclastics is overlain by 6 m of dolomitized bioclastic packstone/wackestone that exhibits an upward-fining texture over the basal 1.5 m.

Subunit IVB: depth, 246.3–279.0 mbsf; age, 0.93–1.27 Ma, early Pleistocene. A coarse to very coarse bioclastic clay at the base and dolomitized micritic to nannofossil chalk throughout the rest of the subunit.

Subunit IVC: depth, 279.0–298.8 mbsf; age, 1.27–1.48 Ma, early Pleistocene. The base of the subunit is defined by a 30-cm-thick dark glauconitic packstone, which is replaced upward by a dolomitized micritic to nannofossil-rich chalk.

5. *Unit V:* depth, 298.8–400.0 mbsf; age, 1.27–1.48 Ma, early Pleistocene. Dolomitized bioclastic packstones and chalky mixed sediments interbedded with less calcareous sandy, silty, and clayey mudstones. The unit was deposited at an extremely rapid rate. Five subunits have been recognized.

Subunit VA: depth, 298.8–322.0 mbsf; age, 1.27–1.48 Ma, early Pleistocene. Chalk with bioclasts and siliciclasts.

Subunit VB: depth, 322.0–350.0 mbsf; age, 1.27–1.48 Ma, early Pleistocene. Upward-coarsening dolomitized bioclastic packstone and chalk with siliciclastic mudstones.

Subunit VC: depth, 350.0–360.0 mbsf; age, 1.27–1.48 Ma, early Pleistocene. Dolomitized calcareous silt to medium-grained sands.

Subunit VD: depth, 360.0–377.0 mbsf; age, 1.27–1.48 Ma, early Pleistocene. Upward-coarsening dolomitized bioclastic packstones and chalks with siliciclastic-rich muds.

Subunit VE: depth, 377.0–400.0 mbsf; age, 1.27–1.48 Ma, early Pleistocene. Dolomitic calcareous silt to medium sand intercalated with a central section of clayey to silty mud.

Interstitial water sampling at Site 821 shows that calcium, magnesium, and potassium decrease with depth to 144.8 mbsf. This occurs mainly because of the precipitation of calcite and dolomite and clay diagenesis, that leads to the formation of illite. An increase in strontium throughout much of the hole is due to dissolution of aragonite and high-magnesium calcite combined with precipitation of low-magnesium calcite and dolomite; decreases in strontium in the lower part of the core reflect clay mineral diagenesis and a lower rate of recrystallization of carbonates. Alkalinity increases to 11 mbsf and peaks again at 116.35 mbsf, coincident with the removal of sulfate. Chlorinity decreases are tied to salinity changes effected by the precipitation of carbonates and the removal of sulfate.

X-ray diffraction analysis indicates that the sediments at Site 821 are composed of aragonite, low-magnesium calcite, high-magnesium calcite, dolomite, quartz, kaolinite, albite, and illite. Variations in carbonate content are due to dilution by terrigenous material and may reflect alternations of sea level. Dolomite occurs at ~10% between 40 and 398.5 mbsf coincident with the depth of removal of high-magnesium calcite. As at Sites 819 and 820, it is proposed that high-magnesium calcite provides the magnesium source for dolomitization.

Organic carbon at Site 821 was generally low, varying between 0.15% and 0.45%. This is thought to be of mixed terrigenous/marine origin above 120 mbsf and of marine origin below this depth. Methane concentrations reached a maximum of 74,000 ppm at 220 mbsf, whereas the C_1/C_2 ratio varied with depth and temperature between 3600 and 800, showing no anomalous trend. There were no safety or pollution problems at this site; total ethane and propane never exceeded 40 ppm, with ethane greater than propane above 310 mbsf. Methane and propane above 250 mbsf are of bacterial origin.

Downhole measurements at Site 821 included runs with the seismic stratigraphy logging tool combination and the formation microscanner. The velocity, density, and resistivity are strongly correlated because of the dominance of porosity in all three logs. Three log units have been identified. Log Unit 1 occurs from the base of the pipe (65 mbsf) to 210 mbsf and is considered as equivalent to lithologic Units I, II, and III. The resistivity log suggests upward-fining sequences 4– to 14-m thick caused by increases in the proportions of clay and decreases in carbonate. Log Unit 2 occurs between 210 and 293 mbsf and equates with lithologic Unit IV. Again, the resistivity log exhibits a saw-toothed pattern that suggests upward-fining sequences 10– to 20-m thick; however, the gamma-ray log correlates positively with resistivity and velocity, suggesting that clay-rich intervals are low in porosity, perhaps the result of diagenesis. Between 261 and 270 mbsf, a comparison of velocity and resistivity indicates substantial cementation, which is borne out by the lithostratigraphic identification of an increase in dolomitization in the same interval. Log Unit 3 occurs between 293 and 392 mbsf and is considered to be equivalent to lithologic Unit V. Logs indicate four cycles of upward-coarsening sequences, as indicated by upward-decreasing clay contents and porosity, as seen in the gamma-ray, resistivity, and velocity logs.

Paleomagnetic results from Site 821 must await shore-based studies. A large portion of the sediments from the Pleistocene cored sections were found to carry a remanence with a steeply dipping negative inclination. Many of the cores maintained this remanence direction after AF demagnetization with peak fields of 15 mT, the maximum field allowable on the archive half of the cores. Detailed AF demagnetization in peak fields greater than 15 mT, together with thermal treatment, will be required to generate a clear magnetic polarity stratigraphy at this site.

BACKGROUND AND SCIENTIFIC OBJECTIVES

Site 821 is one of three sites in close proximity that were occupied in Grafton Passage. For a summary of the background and overall objectives of these sites the reader is referred to the "Background and Scientific Objectives" section of the "Site 819" chapter.

Site 821 is located on the inner portion of an upper slope terrace (Fig. 2, "Site 819" chapter, this volume) adjacent to the Great Barrier Reef. Of the three sites occupied in Grafton Passage it is the most proximal to the Great Barrier Reef. The pre-drilling prognosis for this site is shown in Figure 1.

The objectives at this site were as follows:

1. To determine the age and facies of the most proximal portions of the aggradational and progradational units immediately in front of the present Great Barrier Reef.

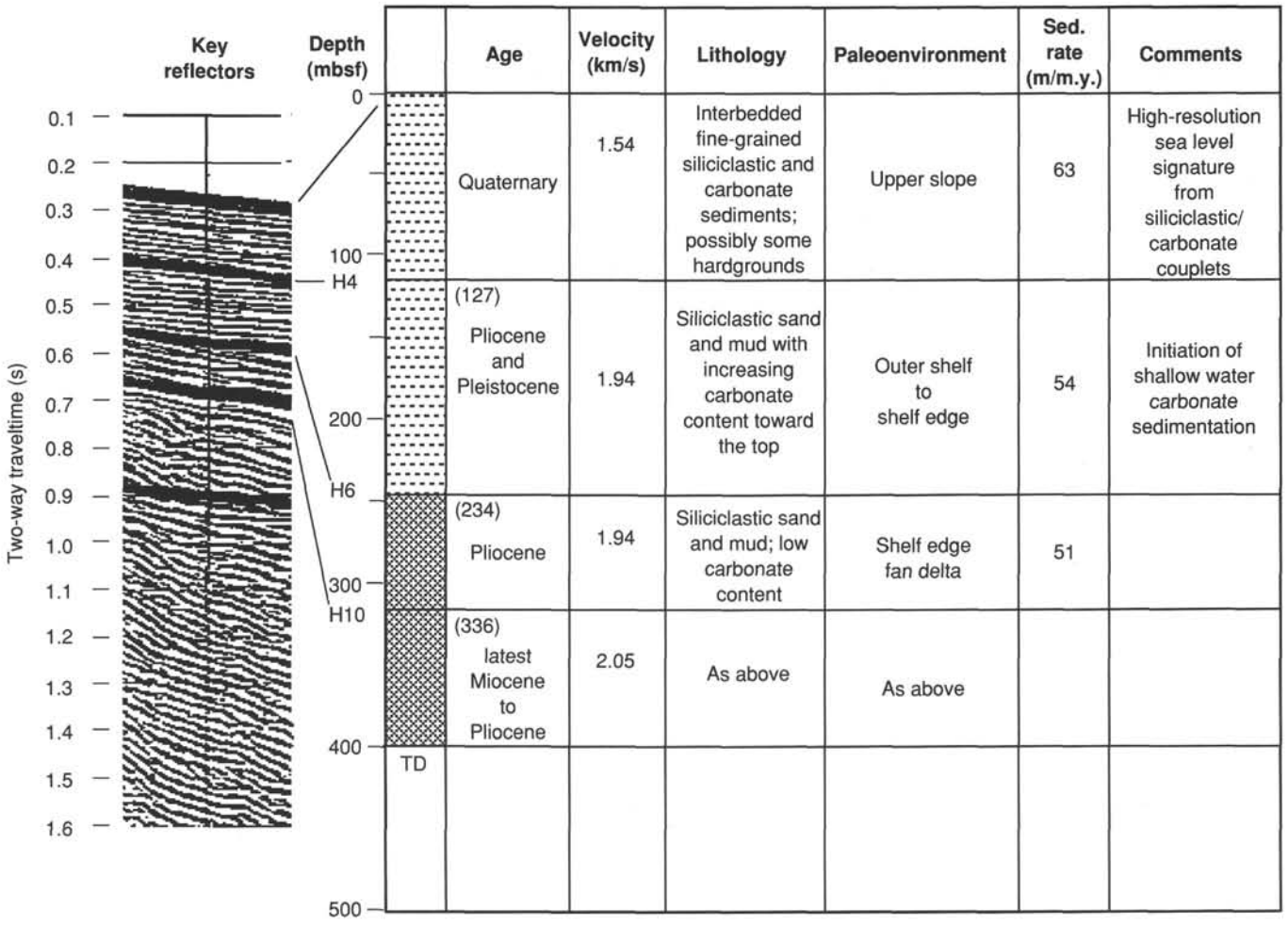

Age	Velocity (km/s)	Lithology	Paleoenvironment	Sed. rate (m/m.y.)	Comments
Quaternary	1.54	Interbedded fine-grained siliciclastic and carbonate sediments; possibly some hardgrounds	Upper slope	63	High-resolution sea level signature from siliciclastic/ carbonate couplets
(127) Pliocene and Pleistocene	1.94	Siliciclastic sand and mud with increasing carbonate content toward the top	Outer shelf to shelf edge	54	Initiation of shallow water carbonate sedimentation
(234) Pliocene	1.94	Siliciclastic sand and mud; low carbonate content	Shelf edge fan delta	51	
(336) latest Miocene to Pliocene	2.05	As above	As above		
TD					

Figure 1. Pre-drilling prognosis for Site 821.

2. To determine the relationship between sea level and depositional facies to extract the sea-level signature.
3. To determine the timing and factors controlling the initiation of reef growth on the central Great Barrier Reef.
4. To understand the factors that control the transition from prograding to aggrading depositional geometries.

In addition to the above, a principal objective that applies equally to all three sites is to define the processes of upper-slope deposition and their relationship with mid-slope processes and products seen at Site 822.

OPERATIONS

Transit to Hole 821A

The ship moved 1.0 nmi from Site 820 to Site 821 (proposed Site NEA-1) in 0.95 hr, in dynamic positioning mode at an average speed of 1.05 kt. The same Benthos low-power beacon used at Sites 819 and 820 was run on the taut wire at 0330L (all times in this section given in local time, or L) 15 September. The location of Site 821 is 16°38.793′S, 146°17.376′E; the precision depth recorder (PDR) indicated that water depth at the site is 212.6 m below sea level (mbsl). The bit was positioned 207.6 mbsl, and the first core shot at 0429L, 15 September. Core 133-821A-1H recovered 4.39 m of sediment, and the mud line was estimated at 212.7 mbsl. Continuous APC cores (Cores 133-821A-1H through -16H) were recovered from 0.0 to 145.9 mbsf, with 145.9 m cored and 149.4 m recovered (102.4% recovery). Core 133-821A-16H hit a layer of coarse-grained bioclastic material, which shattered the liner.

Cores 133-821A-17X through -43X were taken from 145.9 to 400.0 mbsf, with 254.1 m cored and 233.5 m recovered (91.88% recovery). As hole conditions appeared to be excellent, we decided to cancel a hole-conditioning trip in the interest of time. The go-devil was dropped and the bit was pulled to 85.3 mbsf for logging. Logs were run as follows:

1. The induction/density/sonic/caliper/gamma-ray (DITE/HLDT/SDT/MCDG/NGT) logging tool was run into the hole at 1035L, 16 September, where we found 4.5 m of fill on the bottom of the hole. The tool was back out of the hole at 1241L.
2. Owing to the excellent condition of the hole, the formation microscanner/gamma-ray/temperature (FMS/NGT/TCC) logging tool was run. The tool was sent into the hole at 1330L, 16 September, where we found 8.4 m of fill at the bottom of the hole. This tool was back out of the hole at 1500L.

Hole 821A was filled with heavy mud; we pulled the bit clear of the seafloor at 1710L, 16 September to begin Hole 821B.

Hole 821B

The ship moved 25 m west to Hole 821B at 16°38.794′S, 146°17.366′E. The mud line was estimated to occur at a water

depth of 211.6 mbsl. The bit was positioned at 211.5 mbsl to spud the first core at 1825L, 16 September. Core 133-821B-1H recovered 9.83 m of sediment, which indicates that the mud line is at 211.6 mbsl. Continuous APC cores (Cores 133-821B-1H through -14H) were taken from 0 to 140.0 mbsf, with 140 m cored and 144.8 m recovered (103.4%). APC coring ended at the top of a coarse bioclastic interval, where the vibrapercussive corer (VPC) was picked up for our attempt to recover this interval better.

Cores 133-821B-16V to -18V were taken from 140.0 to 146.6 mbsf, with 6.6 m cored and 6.6 m recovered (100.0% recovery, using the advance-by-recovery method). As predicted, material in the VPC cores from this interval were less disturbed than XCB cores might have been. However, only in Core 133-821B-17V did we actually recover material. Therefore, we picked up the XCB in the hope of obtaining better recovery.

Cores 133-821B-19X through -20X were taken from 146.6 to 165.9 mbsf, with 19.3 m cored and 15.9 m recovered (88.0% recovery). Hole 821B was filled with heavy mud, and the bit was pulled out of the hole, arriving on deck at 0619L, 17 September.

Table 1 contains the coring summary for Site 821.

SITE GEOPHYSICS

A general description of the design and operation of the joint site location survey for Sites 819, 820, and 821 is included in the "Site Geophysics" section, "Site 819" chapter (this volume).

Site 821

Following completion of drilling at Hole 820B and separation from the beacon at JD 257/1559 UTC on 14 September 1990, *JOIDES Resolution* returned to the confirmed global positioning system (GPS) position of Site 821 under dynamic positioning control. The taut-wire beacon was deployed at the site at JD 257/1656 UTC, and the final coordinates of Hole 821A are 16°38.793′S and 146°17.376′E, with a water depth of 212.7 m (drill-pipe measurement from sea level).

Site 821 is the most landward or westerly of the three sites (Sites 819, 820, and 821) on the upper slope terrace adjacent to the Great Barrier Reef, being about 5 km west of Site 819 and 2 km west of Site 821 (Figs. 2 and 3). It lies about 6 km east of the nearest reef (Euston Reef), and was positioned to examine the most proximal parts of both the topset facies of the progradational units, and the aggradational units, that underlie the upper slope (Fig. 4; Symonds and Davies, 1988).

There was reasonable correspondence of the major features at the site on the *JOIDES Resolution* single channel seismic profiles and the *Rig Seismic* multichannel seismic profiles (Figs. 3 and 4), but the detailed seismic characteristics of the site were difficult to resolve on the *Resolution* profile owing to the very compressed nature of the record. Basement is not visible on any of the water-gun data across the site; however, normal resolution Gulf Aquapulse seismic data in the area (Symonds et al., 1983) indicates that it may lie up to 4 s TWT (two-way traveltime) below seafloor. The site is underlain by parallel to subparallel reflectors and no distinctive sequence boundaries are present (Fig. 4); however, when the sequence boundaries are traced landward from Site 820, the internal character of reflector packages is maintained through Site 821. The upper, aggradational unit is 0.2 s TWT (~170 m) thick, and as at Site 820 its upper part contains higher amplitude reflectors than its lower part. The irregular, disrupted reflector that occurs within this unit at Site 820 does not maintain its character to Site 821. The underlying units to beyond TD represent the topset facies of various prograda-

Table 1. Coring summary, Site 821.

Core no.	Date (Sept. 1990)	Time (UTC)	Depth (mbsf)	Length cored (m)	Length recovered (m)	Recovery (%)
Hole 821A						
1H	14	1830	0–4.4	4.4	4.39	99.8
2H	14	1840	4.4–13.9	9.5	9.51	100.0
3H	14	1850	13.9–23.4	9.5	9.44	99.3
4H	14	1920	23.4–32.9	9.5	9.91	104.0
5H	14	1940	32.9–42.4	9.5	10.09	106.2
6H	14	2005	42.4–51.9	9.5	9.56	100.0
7H	14	2025	51.9–61.4	9.5	9.91	104.0
8H	14	2040	61.4–70.9	9.5	9.97	105.0
9H	14	2105	70.9–80.4	9.5	9.99	105.0
10H	14	2120	80.4–89.9	9.5	9.92	104.0
11H	14	2140	89.9–99.4	9.5	9.97	105.0
12H	14	2155	99.4–108.9	9.5	9.94	104.0
13H	14	2210	108.9–118.4	9.5	9.63	101.0
14H	14	2235	118.4–127.9	9.5	9.95	105.0
15H	14	2255	127.9–137.4	9.5	9.55	100.0
16H	14	2315	137.4–145.9	8.5	7.62	89.6
17X	15	0005	145.9–155.6	9.7	9.72	100.0
18X	15	0020	155.6–165.2	9.6	8.82	91.9
19X	15	0040	165.2–174.9	9.7	8.87	91.4
20X	15	0105	174.9–184.6	9.7	8.59	88.5
21X	15	0120	184.6–193.9	9.3	9.55	102.0
22X	15	0140	193.9–203.5	9.6	9.40	97.9
23X	15	0220	203.5–212.8	9.3	7.94	85.4
24X	15	0245	212.8–222.5	9.7	9.77	101.0
25X	15	0315	222.5–232.2	9.7	9.84	101.0
26X	15	0350	232.2–241.8	9.6	9.89	103.0
27X	15	0420	241.8–251.4	9.6	9.78	102.0
28X	15	0445	251.4–261.1	9.7	9.85	101.0
29X	15	0520	261.1–270.8	9.7	8.99	92.7
30X	15	0545	270.8–280.4	9.6	10.02	104.4
31X	15	0650	280.4–290.1	9.7	7.54	77.7
32X	15	0755	290.1–299.7	9.6	0.32	3.3
33X	15	0900	299.7–309.4	9.7	9.81	101.0
34X	15	1010	309.4–319.0	9.6	8.99	93.6
35X	15	1155	319.0–328.7	9.7	6.87	70.8
36X	15	1325	328.7–338.3	9.6	9.81	102.0
37X	15	1425	338.3–347.9	9.6	9.29	96.8
38X	15	1520	347.9–357.5	9.6	8.69	90.5
39X	15	1710	357.5–367.2	9.7	9.85	101.0
40X	15	1825	367.2–376.8	9.6	8.24	85.8
41X	15	2000	376.8–386.4	9.6	8.78	91.4
42X	15	2125	386.4–396.1	9.7	10.10	104.1
43X	15	2210	396.1–400.0	3.9	4.24	109.0
			Coring totals	400.0	382.91	95.7
Hole 821B						
1H	16	0830	0–9.5	9.5	9.83	103.0
2H	16	0845	9.5–19.0	9.5	9.99	105.0
3H	16	0900	19.0–28.5	9.5	9.62	101.0
4H	16	0920	28.5–38.0	9.5	9.65	101.0
5H	16	0945	38.0–47.5	9.5	9.77	103.0
6H	16	1010	47.5–57.0	9.5	9.86	104.0
7H	16	1035	57.0–66.5	9.5	9.63	101.0
8H	16	1100	66.5–76.0	9.5	9.74	102.0
9H	16	1125	76.0–85.5	9.5	9.79	103.0
10H	16	1150	85.5–95.0	9.5	7.71	81.1
11H	16	1210	95.0–104.5	9.5	9.84	103.0
12H	16	1240	104.5–114.0	9.5	9.94	104.0
13H	16	1300	114.0–123.5	9.5	9.77	103.0
14H	16	1320	123.5–133.0	9.5	9.95	105.0
15H	16	1340	133.0–140.0	7.0	9.76	139.0
16V	16	1505	140.0–140.0	0.0	0.01	100.0
17V	16	1605	140.0–146.6	6.6	6.60	100.0
18V	16	1710	146.6–146.6	0.0	0.00	0.0
19X	16	1735	146.6–156.2	9.6	6.81	70.9
20X	16	1755	156.2–165.9	9.7	9.14	94.2
			Coring totals	165.9	167.41	100.9

Note: Times are Universal Time Coordinated or UTC, which is 10 hr different from local time or L.

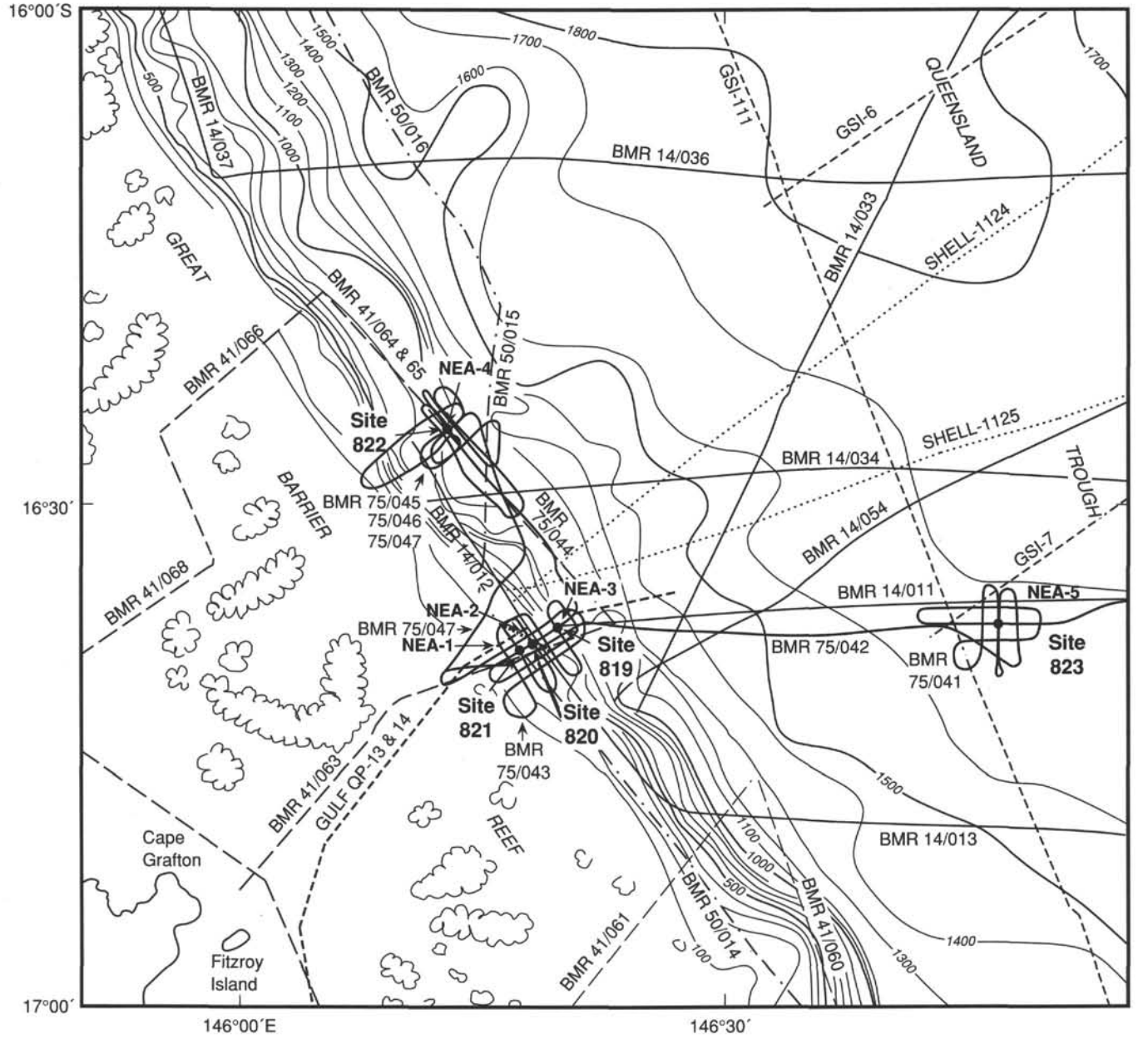

Figure 2. Track chart showing the distribution of regional seismic data in the area around Sites 819, 820, and 821; also shown are locations of Sites 822 and 823; simplified bathymetry in meters.

tional units. The foreset facies of these units generally lie to the east of Site 820. The topsets related to the upper, gently sigmoidal unit are about 0.06 s TWT (~60 m) thick, and consist of both high and low amplitude reflectors. The topsets related to the lower, complex sigmoid-oblique progradational units are at least 0.14 s TWT (~160 m) thick and appear to be composed of very low amplitude reflectors. These units extend to just beyond TD at Site 821 and lie largely within the first water-bottom multiple at the site (Fig. 4).

To provide some predictive capability during the drilling at Site 821, an estimate of the two-way traveltime (TWT)/depth relationship below the seafloor was made using stacking derived interval velocities from the BMR seismic lines across the site. In Figure 5, this relationship is compared with similarly derived TWT/depth curves for the adjacent Sites 819 and 820.

LITHOSTRATIGRAPHY

Site 821 is located in 212 m of water depth in Grafton Passage; the most landward site in a transect of three sites (Sites 819, 820, and 821) on the upper slope east of the present day Great Barrier Reef. APC drilling of Hole 821A recovered a complete section to 145.9 mbsf; a change to XCB and further drilling to 400 m recovered an almost complete section, with the exception of the interval between 290.1 and 299.7 mbsf, where only 3.3% was recovered. Hole 821B was drilled by APC to 140.0 mbsf, VPC from 140.0 to 146.6 mbsf, and finished with XCB down to the total depth of 165.9 mbsf. Recovery in this hole was almost complete.

The lithostratigraphy of Site 821 is divided into five units (Fig. 6) based on sharp lithologic changes, usually associated with distinct rather thin, fining-upward, coarse siliciclastic

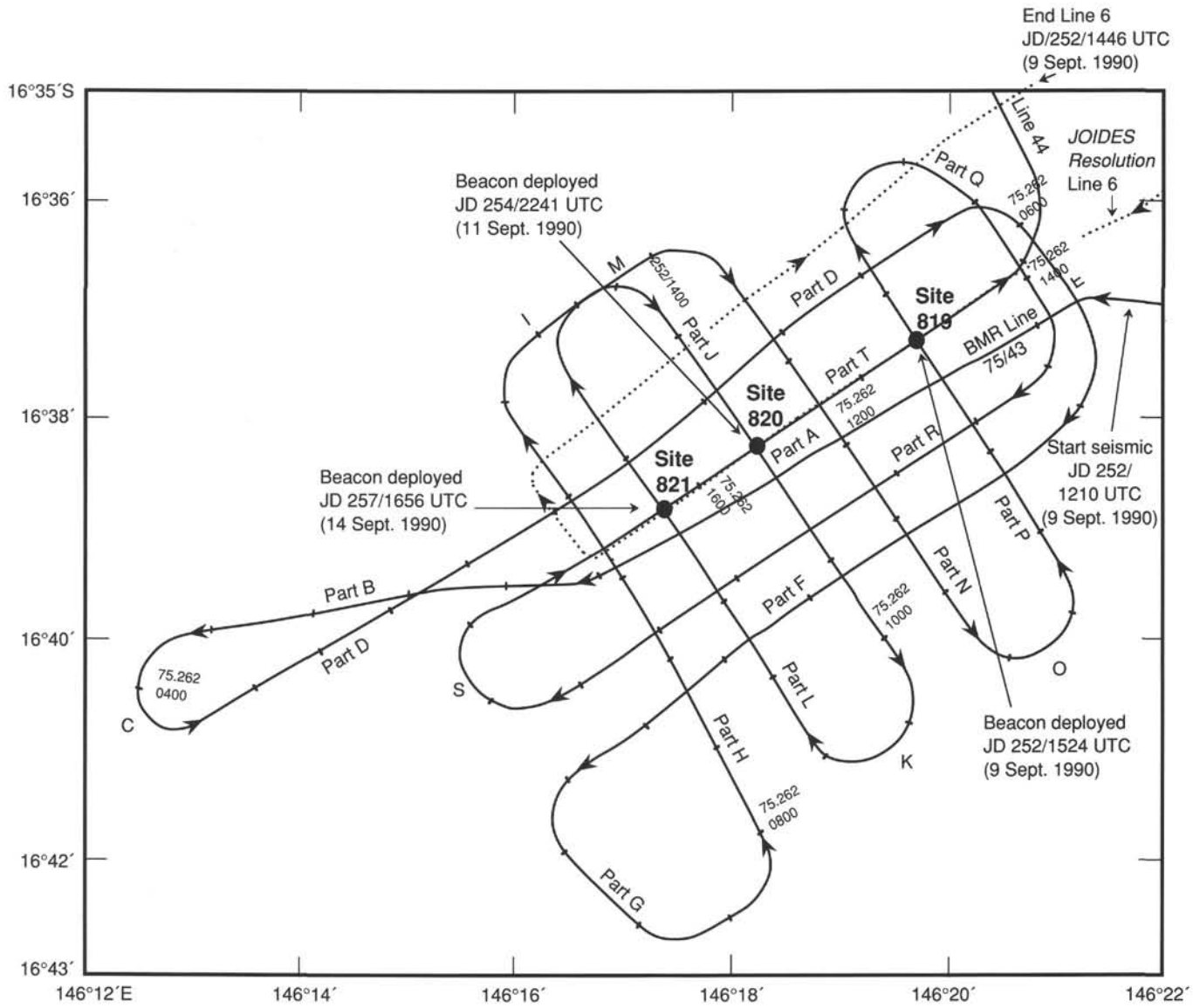

Figure 3. *JOIDES Resolution* Leg 133 site location tracks (dotted line) and *Rig Seismic* 1987 site survey tracks (solid line) around Sites 819, 820, and 821.

beds above the unit boundary. The upper half of Unit I consists of fining-upward cycles, each of which is composed of (1) greenish gray calcareous sand; (2) greenish gray calcareous silt; and (3) light greenish gray calcareous clay. The lower half of Unit I is composed of alternations of calcareous silt and clay, which tend to become chalky with a greenish gray color downward. This lower part also contains intercalated beds of calcareous silty sand or wackestone. Unit II is composed of two sets of dark gray, bioclastic calcareous mudstone or chalk overlying a partially to well lithified, gray to light gray, bioclastic packstone. Unit III is represented by greenish gray, dolomitized, bioclastic wackestone, chalky wackestone and chalk, with interbeds of lightly greenish gray bioclastic packstone. Unit IV consists of considerably dolomitized greenish gray chalk intercalated with varying thicknesses of light greenish gray bioclastic packstone-wackestones. Unit V is characterized by coarsening-upward cycles composed predominantly of greenish-gray clay and clayey to sandy calcareous mixed-sediment, with subordinate amounts of calcareous sandstone and calcareous mudstone. Scattered foraminifer tests and molluscan shell fragments occur throughout the unit.

Lithologic Units

Unit I (Sections 133-821A-1H-1 through -16H-4; depth, 0–145.5 mbsf; age, Holocene to late Pleistocene [<0.93 Ma])

This unit consists of three fining-upward cycles in the upper half, and rhythmic alternations of calcareous clay, silt beds, and calcareous silty sand or wackestone in the lower half. A shallow water-derived *Halimeda* rudstone defines the basal part of the unit.

Subunit IA (Sections 133-821A-1H-1 through -2H-5; depth, 0–16.5 mbsf. age, Holocene to late Pleistocene [<0.275 Ma])

Subunit IA forms an upward-fining set composed of (1) sand-sized bioclastic-siliciclastic sediment with large benthic foraminifers, coralline algae, bryozoans, etc.; (2) homogeneous clayey-silt to clay mixed sediment with bioclasts and nannofossils; and (3) clay with bioclasts and nannofossils.

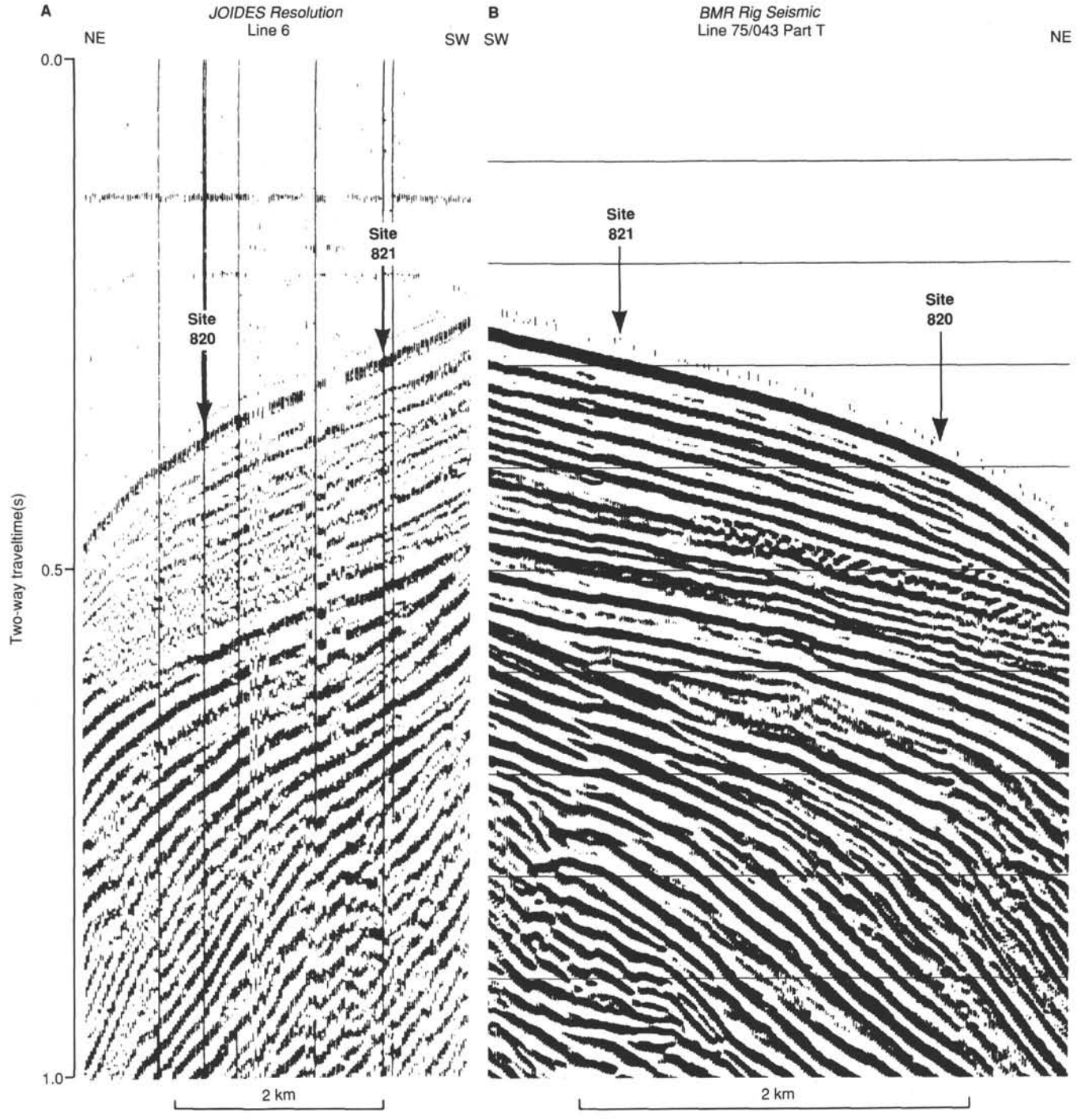

Figure 4. Comparison of *JOIDES Resolution* and *Rig Seismic* 80-in.^{3} water gun seismic profiles across Site 821. **A.** *JOIDES Resolution*. **B.** *Rig Seismic*.

Subunit IB (Sections 133-821A-2H-5 through -5H-5; depth, 16.5–40.3 mbsf; age, late Pleistocene [<0.465 Ma])

Subunit IB forms two upward-fining sets composed of (1) homogeneous silt- to sand-sized mixed sediment with bioclasts and mollusks and/or bryozoan fragments; (2) sandy bioclastic and siliciclastic mixed sediment with large benthic foraminifers, *Halimeda* internodes, coralline algae, pectinids and other mollusks; and (3) calcareous clay and silt, and mixed sediment.

Subunit IC (Sections 133-821A-5H-5 through -8H-3; depth, 40.3–66.5 mbsf; age, late Pleistocene [between 0.275 and 0.465 Ma])

Subunit IC also consists of two upward-fining cycles composed of (1) sandy silt to fine- to medium-sand with bioclasts and minor siliciclastic material; (2) clayey silt with bioclasts; and (3) homogeneous silty-clay to clay or clayey-silt with bioclasts and nannofossils.

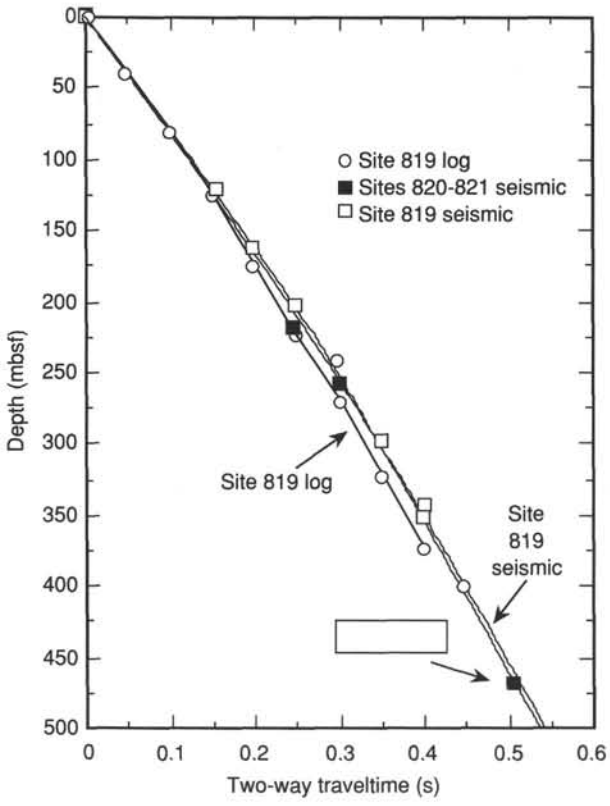

Figure 5. Comparison of TWT/depth curve estimated for Site 821 with those for Sites 819 and 820.

Subunit ID (Sections 133-821A-8H-3 through -10H-7; depth, 66.5–88.7 mbsf; age, late Pleistocene [between 0.275 and 0.465 Ma])

This subunit exhibits a rhythmic alternation of calcareous silty clay and clayey silt and, in part, lithified and dolomitized sandy layers of mixed sediment.

Subunit IE (Sections 133-821A-10H-7 through -11H-6; depth, 88.7–99.2 mbsf; age, late Pleistocene [between 0.275 and 0.465 Ma])

An upward-coarsening dolomitized calcareous bioclastic sand that contains a silty mud bed in the middle of the subunit.

Subunit IF (Sections 133-821A-11H-6 through -15H-3; depth, 99.2–132.1 mbsf; age, late Pleistocene [between 0.275 and 0.93 Ma])

Subunit IF is composed of three repeated cycles of interbedded, poorly sorted, firm, bioclastic sand or wackestone, and bioclastic-nannofossil ooze or chalk.

Subunit IG (ections 133-821A-15H-3 through -16H-4; depth, 132.1–145.5 mbsf; age, late Pleistocene [between 0.465 and 0.93 Ma])

The lowermost subunit within Unit I is characterized by upward-fining sediments consisting of (1) partially lithified, *Halimeda* rudstone, with minor molluscan and bryozoan fragments, large benthic foraminifer tests, and lithoclasts of packstone or other sediment types in a mud matrix; (2) calcareous mudstone with sand-sized siliciclastic detritus; and (3) medium to fine sand-sized bioclastic packstones.

Unit II (Sections 133-821A-16H-4 through -19X-5; depth, 145.5–172.0 mbsf; age, late Pleistocene [between 0.465 and 0.93 Ma])

Two suites of partially to completely lithified bioclastic packstone are overlain by a bioclastic to calcareous mudstone or chalk.

Subunit IIA (Sections 133-821A-16H-4 through -17X-CC; depth, 145.5–156.3 mbsf; age, late Pleistocene [between 0.465 and 0.93 Ma])

Partially to well-lithified bioclastic packstone is overlain by a 1.5-m-thick bed of firm to partially lithified chalk to calcareous mudstone. The uppermost part contains glauconite as detrital grains as well as infilling foraminifer chambers and may represent a submarine erosional or nondepositional hardground.

Subunit IIB (Sections 133-821A-18X-1 through -19X-5; depth, 156.3–172.0 mbsf; age, late Pleistocene [between 0.465 and 0.93 Ma])

A 7-m-thick bioclastic mudstone bed is underlain by partially to entirely lithified bioclastic packstone. The basal 2-m of bioclastic packstone contains abundant siliciclastic detritus and exhibits upward-fining structure.

Unit III (Sections 133-821A-19X-5 through -24X-2; depth, 172.0–215.0 mbsf; age, early Pleistocene [between 0.465 and 1.27 Ma])

This unit consists of partially dolomitized bioclastic wackestone, chalky wackestone, and chalk, with interbedded dolomitized bioclastic packstone layers.

Subunit IIIA (Sections 133-821A-19X-5 through -20X-6; depth, 172.0–184.3 mbsf; age, early Pleistocene [between 0.465 and 0.93 Ma])

Subunit IIIA is a lithified, dolomitized, bioclastic wackestone to chalk in the middle of which is a 3-m-thick, dolomitized, bioclastic packstone bed.

Subunit IIIB (Sections 133-821A-21X-1 through -24X-2; depth, 184.3–215.8 mbsf; age, early Pleistocene [between 0.93 and 1.27 Ma])

Subunit IIIB, a lithified, dolomitized, bioclastic wackestone to nannofossil-rich, chalky wackestone, has scattered intercalations of dolomitized bioclastic packstone or mixed sediment layers. The lowermost 50-cm-thick bed is a coarse-grained mixed sediment.

Unit IV (Sections 133-821A-24X-2 through -32X-CC; depth, 215.8–298.8 mbsf; age, early Pleistocene [between 0.93 and 1.48 Ma])

This unit comprises extensively dolomitized chalk interbedded with bioclastic packstone-wackestone beds of various thickness.

Subunit IVA (Sections 133-821A-24X-2 through -27X-4; depth, 215.8-246.3 mbsf; age, early Pleistocene [between 0.93 and 1.27 Ma])

In Subunit IVA, dolomitized micritic to nannofossil-rich chalk with bioclastic and siliciclastic detritus is overlain by a 6-m-thick bed composed of dolomitized bioclastic packstone to wackestone. An upward-fining structure was observed in a 1.5-m-thick wackestone layer at the base.

Subunit IVB (Sections 133-821A-27X-4 through -30X-6; depth, 246.3–279.0 mbsf; age, early Pleistocene [between 0.93 and 1.27 Ma])

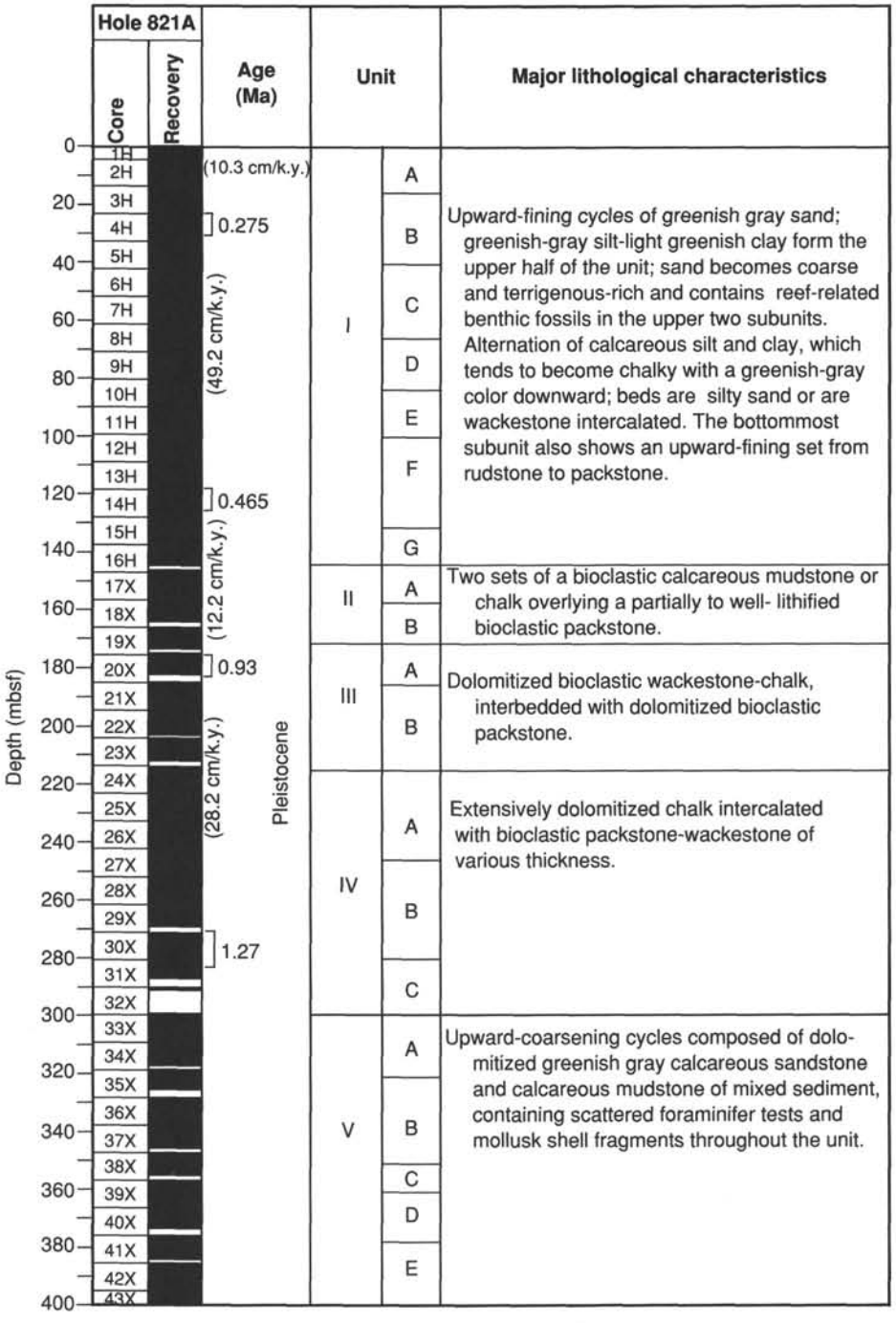

Figure 6. Summary chart showing the lithostratigraphy and lithologic characteristics for each unit at Site 821. Age assignment is provided by nannofossil biostratigraphy (See "Biostratigraphy" section, this chapter).

In addition to dolomitized micritic to nannofossil-rich chalk, this subunit also contains an upward-coarsening, less lithified clayey layer with coarse- to very coarse-grained bioclasts.

Subunit IVC (Sections 133-821A-30X-6 through -32X-CC; depth, 279.0–298.8 mbsf; age, early Pleistocene [between 1.27 and 1.48 Ma])

Subunit IVC is a dolomitized micritic to bioclastic chalk with a 5-cm-interval of planar lamination close to the top. A 30-cm-thick, dark greenish-gray, glauconitic(?) packstone occurs at the top.

Unit V (Sections 133-821A-33X-1 through -43X-CC; depth, 298.8–400.0 mbsf; age, early Pleistocene [between 1.27 and 1.48 Ma])

Unit V is distinctly different in lithologic characteristics from the four units above. It is characterized by upward-coarsening, dolomitized, greenish-gray, calcareous mixed sediment, interbedded with less calcareous mudstone and silts and sands.

Wispy lamination occurs in the middle two silty subunits. Foraminifer tests and mollusk shell fragments are scattered throughout the unit.

Subunit VA (Sections 133-821A-33X-1 through -35X-5; depth, 298.0–322.0 mbsf; age, early Pleistocene [between 1.27 and 1.48 Ma])

Subunit IA consists of upward-coarsening, dark greenish-gray chalk with bioclasts and abundant siliciclastic material.

Subunit VB (Sections 133-821A-35X-CC through -37X-CC; depth, 322.0–350.0 mbsf; age, early Pleistocene [between 1.27 and 1.48 Ma])

Upward-coarsening, greenish-gray dolomitized, bioclastic packstone to chalk with siliciclastic mud comprises Subunit VB.

Subunit VC (Sections 133-821A-38X-1 through -39X-2; depth, 350.0–360.0 mbsf; age, early Pleistocene [between 1.27 and 1.48 Ma])

This subunit is composed of greenish-gray, dolomitic, calcareous silt to medium-grained mixed sediment: wispy laminations occur at 348.8 mbsf.

Subunit VD (Sections 133-821A-39X-2 through -41X-6; depth, 360.0–377.0 mbsf; age, early Pleistocene [between 1.27 and 1.48 Ma])

Upward-coarsening, dolomitized, bioclastic packstone to chalk with abundant siliciclastic mud dominates this subunit. Wispy lamination occurs at 368.0 mbsf.

Subunit VE (Sections 133-821A-41X-6 through -43X-CC; depth, 377.0–400.0 mbsf; age, early Pleistocene [between 1.27 and 1.48 Ma])

Dolomitic calcareous silt to medium-grained mixed sediment is intercalated with clay and silty mud in the middle of the subunit.

Interpretation

Examination of the site-survey seismic data indicates that Unit V, dominated by upward-coarsening cycles, corresponds to a sequence with progradative geometry (see "Site Geophysics" section; this chapter). Units I and II correspond to a sequence with aggradative geometry. The boundary between Units II and III appears to correspond to the seismic reflector defining the transition from progradational to aggradational seismic geometries.

There is a remarkable degree of correlation between the lithologic units shown in Figure 6 and the variations in calcium carbonate content shown in Figure 7. The mixed lithologic character of Unit V, the generally consistent carbonate facies within Units III and IV, and the cyclical variations within Units I and II are also seen in the carbonate variations. If the variations in %carbonate reflect alternations between siliciclastic-rich, terrestrial-derived and carbonate-rich, marine-derived skeletal sediments, then the facies variations may accurately reflect sea-level fluctuations due to glacio-eustatic control.

The *Halimeda*-dominated sediments in Subunit IG (Fig. 8) suggest a tropical environment, while the shape of the carbonate curve would indicate deposition during a transgression, which may have occurred before 0.465 Ma. Further systematic analysis of both the reef-related and inter-reef benthic organisms among the allochthonous bioclasts or autochthonous build-up in these units will provide more relevant paleoclimatic and paleobathymetric information.

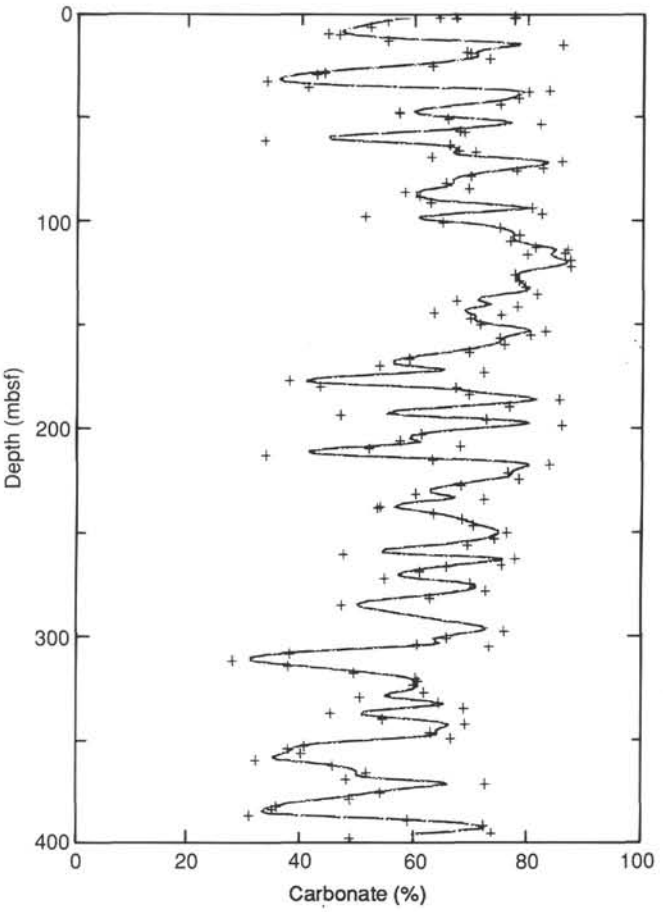

Figure 7. Graph showing trends in the vertical variation of percentage of $CaCO_3$ in Hole 821A. Original data are "smoothed" by a five-point weighted moving average (see "Inorganic Geochemistry" this chapter).

The lithological evidence suggests a hiatus or disconformity between Units I and II. It might explain the apparent decrease of the sedimentation rate in this part of the sequence (see "Sedimentation Rates" section, this chapter).

BIOSTRATIGRAPHY

The abundance and preservation of calcareous microfossils varies with the lithological facies at Hole 821A. Fine-grained muds contain abundant, well-preserved specimens, whereas the sandy intervals are characterized by sparse, poorly preserved specimens. The upper part of the section (Cores 133-821A-1H through -10H) contains abundant, well-preserved planktonic and benthic foraminifers, whereas the lower part of the hole (Cores 133-821A-11H through -43H) generally yield sparse, poorly preserved specimens, but with several exceptions (Samples 133-821A-17H-CC, -28H-CC, -34H-CC, -38H-CC, and -43H-CC). Although some of the poorly preserved faunas contain few depth-indicative benthic foraminifers, preliminary analysis suggests that the faunas at Hole 821A vary from neritic (<200 m) to upper bathyal (200–600 m).

The biostratigraphy of Site 821 is summarized in Figure 9. Planktonic foraminifers and nannofossils indicate a Pleistocene section for all of Hole 821A. Nannofossils indicate that the bottom of Hole 821A has an age between 1.27 and 1.48 Ma.

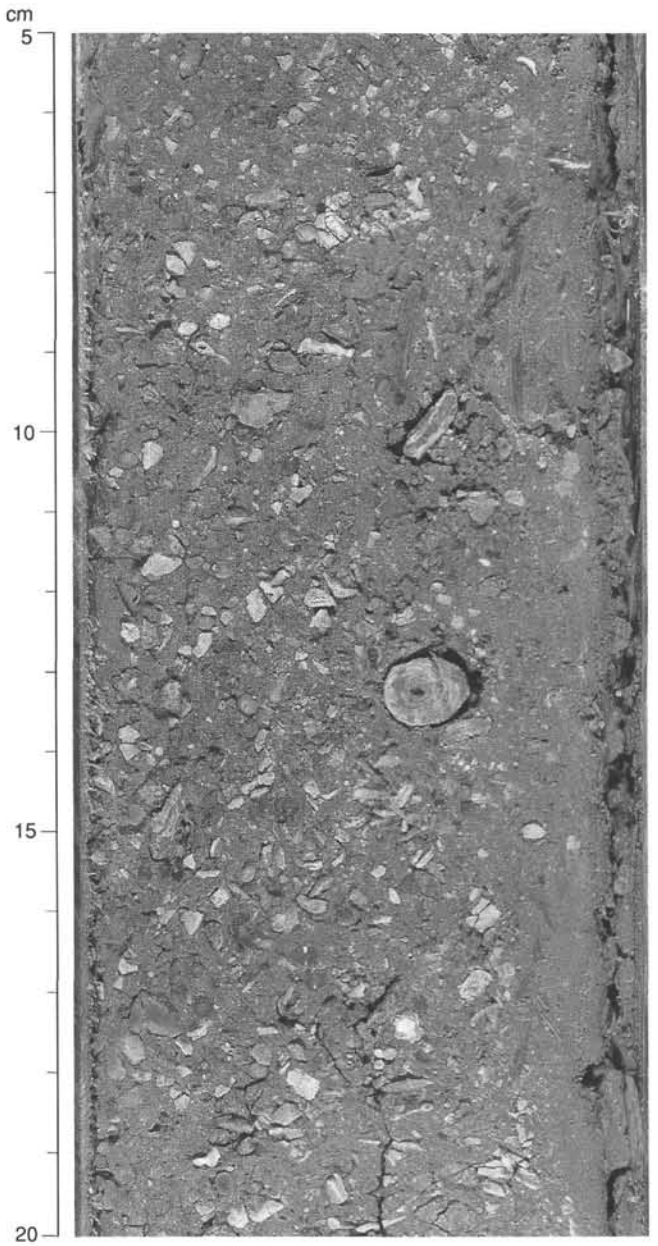

Figure 8. Photograph of the interval between 5 and 20 cm in Section 133-821A-16H-4, showing partially lithified *Halimeda* rudstone composed of an abundance of *Halimeda* internodes in association with skeletal fragments of mollusk shells, large benthic foraminifers, and a variety of encrusting organisms (bryozoans, serpulids, etc.), in addition to lithoclasts of bioclastic packstone and other sediment types. A small "rhodolith" in the middle of the photograph may be composed of bryozoa and nonarticulated coralline algae.

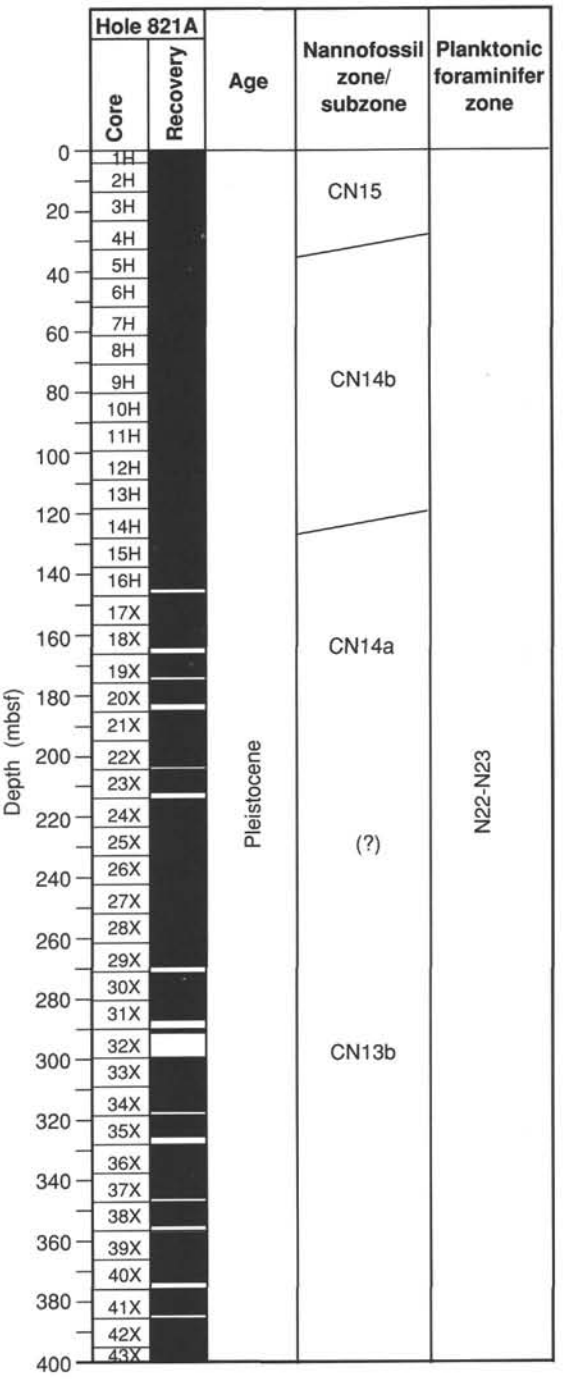

Figure 9. Summary of planktonic microfossil data from Hole 821A.

Calcareous Nannofossils

Site 821 is the shallowest of the three sites on a slope transect to the east of the Great Barrier Reef. Site 821, like the other two sites of the transect (819 and 820), yielded an expanded section of Pleistocene sediments. The bottom of the hole has an age between 1.27 and 1.48 Ma. The sediments consist of highly calcareous mud with varying amounts of calcareous sand. Nannofossils are generally abundant and preservation varies from near pristine in clayey intervals to severely overgrown in sandy intervals. Only core-catcher samples were examined, and from them the following biostratigraphy is constructed.

Emiliania huxleyi occurs in the core-catcher samples of Cores 133-821A-1H through -4H and these four cores are assigned to nannofossil Zone CN15, with an age ≤0.275 Ma. The highest occurrence of *Pseudoemiliania lacunosa* is in Sample 133-821A-14H-CC, and the interval between this and the previous biohorizon is assigned to Subzone CN14b, with an age range of 0.275–0.465 Ma. The next lower subzone, CN14a, extends to Sample 133-821A-20X-CC, which marks the upper limit of dominant small *Gephyrocapsa* with a concomitant virtual absence of large species of this genus. The interval has an age of 0.465–0.93 Ma and is assigned to

Subzone CN14a. The next lower, and oldest biohorizon penetrated, is the highest occurrence of *Helicosphaera sellii* in Sample 133-821A-30X-CC, which has an age of 1.27 Ma and the interval between the last two biohorizons also is assigned to Zone CN13b. The next lower biohorizon, the highest occurrence of *Calcidiscus tropicus* (1.48 Ma) was not penetrated, thus the cored section below Sample 133-821A-30X-CC has an age from 1.27 to 1.48 Ma.

Planktonic Foraminifers

Most core-catcher samples of Hole 821A were examined for planktonic foraminifers. The upper part of the section (Cores 133-821A-1H through -10H) contains abundant, well preserved foraminifers, whereas the lower part of the hole (133-821A-11H through -43H) generally yielded sparse, poorly-preserved specimens, except for some samples (133-821A-17H-CC, -28H-CC, -34H-CC, -38H-CC, and 43H-CC).

The presence of *Bolliella adamsi* in Sample 133-821A-4H-CC, *Globigerina rubescens* pink in Samples 133-821A-1H-CC through -4H-CC, *Globigerinoides ruber* pink in Sample 133-821A-4H-CC, and *Globigerinella calida calida* in Samples 133-821A-4H-CC and -8H-CC, indicates that the upper part of the hole can be referred to the upper Pleistocene. The lower part of the hole contains sparse *Globorotalia truncatulinoides* specimens, which indicates that Zone N22–N23 occurs throughout the hole. As at the other sites on this margin, Sites 819 and 820, the abundance of foraminifers seems to vary with the lithological facies. The fine grained muds contain abundant, well preserved specimens whereas sandy intervals are characterized by sparse, poorly preserved specimens.

Benthic Foraminifers

Samples 133-821A-1H-CC through -10H-CC contain abundant, well-preserved benthic foraminifers. Below this, core-catcher samples generally yield benthic foraminifers with moderate to poor preservation. However, Samples 133-821A-34X-CC, -38X-CC, and -43X-CC contain abundant, well-preserved benthic foraminifers. Although some of the poorly preserved faunas contain few depth-indicative benthic foraminifers, preliminary analysis suggests that the faunas at Hole 821A fluctuate between neritic (<200 m) and upper bathyal (200–600 m).

Samples 133-821A-2H-CC, -5H-CC, -8H-CC, 20H-CC, -23H-CC, -34X-CC, -38X-CC, and -43X-CC contain the upper bathyal depth indicators *Bulimina marginata, Bulimina mexicana, Cibicidoides cicatricosus, C. dutemplei, C. mundulus, C. pachyderma, C. subhaidingerii, Hanzawaia mantaensis, Hoeglundina elegans, Hyalinea balthica, Sigmoilopsis schlumbergeri, Sphaeroidina bulloides,* and *U. proboscidea* (van Morkhoven et al., 1986). Most of these samples include at least a small component of transported specimens, such as *Amphistegina* spp., *Discorbis* spp., and *Planorbulina* spp.

Core-catcher samples examined from Cores 133-821A-10H through -17H lack species found exclusively deeper than 200 m, yet they contain faunas that can be found deeper than 100 m, including the species *B. marginata, C. dutemplei, C. pachyderma, C. subhaidingerii, Hoeglundina elegans, Hyalinea balthica,* and *Sphaeroidina bulloides* (van Morkhoven et al., 1986), indicating an outer neritic paleodepth (100–200 m) for this interval. Samples 133-821A-26X-CC and -30X-CC lack both upper bathyal and outer neritic markers, and preservation is poor; these samples were tentatively assigned to the neritic zone.

PALEOMAGNETISM

Of the two holes (821A and 821B) drilled at this site, continuous paleomagnetic measurements were conducted only at Hole 821A. Cores 133-821A-1H through -16H were collected using the APC system, whereas Cores 133-821A-17X through -43X were obtained with the XCB system. All archive halves of cores from Hole 821A were measured at 10-cm intervals with the shipboard pass-through cryogenic magnetometer both before and after AF demagnetization at 15 mT. Whole-core magnetic susceptibilities also were measured at 10-cm intervals in all core sections using the shipboard Bartington pass-through susceptibility meter.

Paleomagnetic data obtained from the sediments in the upper 120 m of the cored section are of acceptable quality although perhaps not completely free of magnetic overprinting, and may be used for a preliminary polarity assignment (Fig. 10). However, below 120 m, inclinations are scattered, rendering the data unreliable and uninterpretable. We attribute this behavior to drilling disturbances. As a typical example of this, in Figure 11 one can see the variations of magnetic declination, inclination, and intensity after 15-mT AF demagnetization.

As noted above, inclination data in the upper 120 m of Hole 821A are fairly consistent and undisturbed. Inclination excursions, such as those observed around the 45-, 55-, 75-, and 95-mbsf level probably result from drilling deformation and gas expansion near the tops of these cores. When we ignored these variations, inclinations indicated normal polarity was usually about 30°. These values are in good agreement with the geocentric axial dipole inclination for Site 821 of 30.9°, implying that demagnetization at 15 mT was fairly effective for isolating a stable remanent magnetization component. As in nearby Sites 819 and 820, the origin of this remanence is still uncertain, owing to the strong geochemical regimes thought to have affected these sediments.

Available nannofossil data suggest that the upper 130 m or so of the sediments in Hole 821A have an age ≤0.465 Ma.

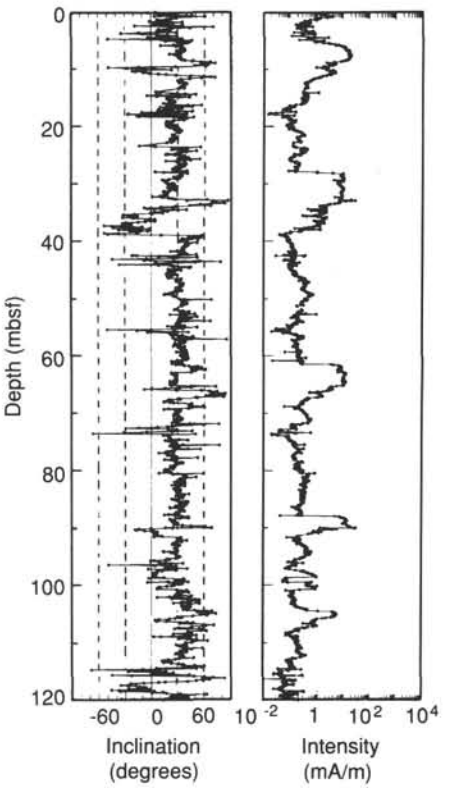

Figure 10. Downhole variation of magnetic inclination (after AF demagnetization at 15 mT) for the upper 120 m of Hole 821A.

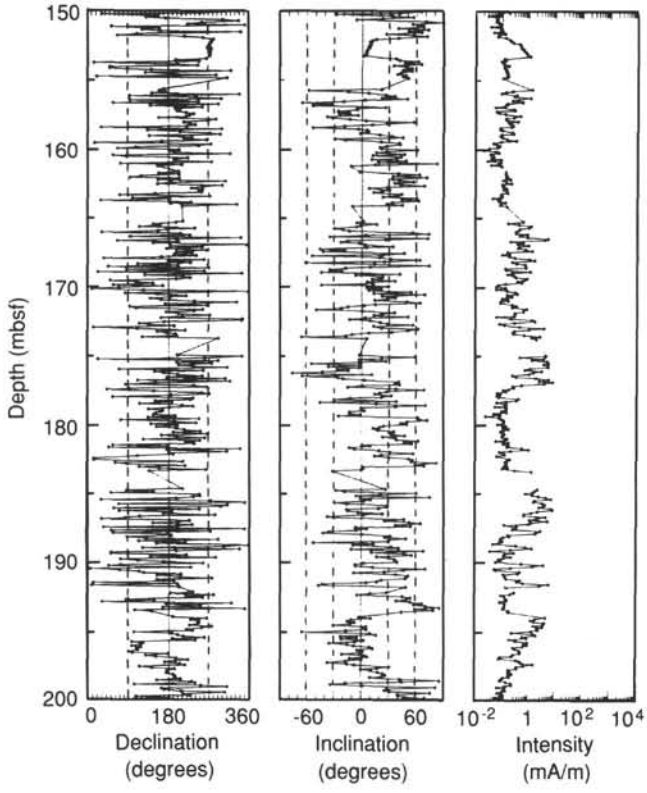

Figure 11. Example of scattered directional results from XCB cores in Hole 821A, 150–200 mbsf interval.

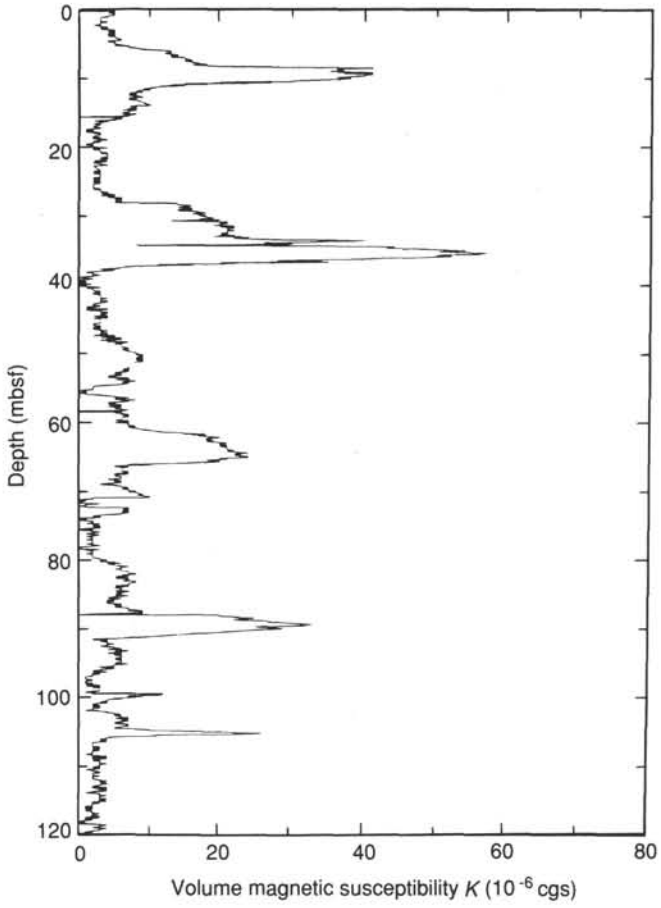

Figure 12. Downhole variation of magnetic susceptibility for the upper 120 mbsf of Hole 821A.

Normal polarity measured to ~120 mbsf is consistent with accumulation during the Brunhes normal chron. We are uncertain if this is a primary or secondary remanence. This normal polarity zone contains at least one short reversed interval at 35–39 mbsf, which may represent a field excursion. Shore-based analysis of 484 undisturbed, oriented discrete samples should help to locate the Brunhes/Matuyama boundary and possibly the Jaramillo subchron, if preserved.

Downhole variation of magnetic susceptibility for the upper 120 mbsf of Hole 821A is shown in Figure 12. As previously observed for Site 820, various large and small peaks seen in the susceptibility data exhibit a strong correlation with the NRM and AF 15 mT intensity. The large susceptibility peaks seen at ~10, 35, 65, and ~90 mbsf correlate well with peaks in the intensity data (Fig. 10). The susceptibility peaks, as at Sites 819 and 820, likely represent periods of lower relative sea level and greater input of terrigenous magnetic minerals.

INORGANIC GEOCHEMISTRY

Interstitial Waters

Interstitial fluids were taken from the first 10 cores of Hole 821A and from Cores 133-821A-13H, -17X, -20X, -23X, -26X, -29X, -33X, -35X, -38X, and -41X. Samples from Hole 821A were analyzed according to the procedures outlined in the "Explanatory Notes" (this volume). These data are listed in Table 2 and Figures 13 and 14.

Calcium, Magnesium, Potassium, and Strontium

The concentration of Ca^{2+} decreases below surface seawater values (10.36 mM) to a minimum of 2.32 mM at 144.8 mbsf (Fig. 13). Magnesium also decreases in concentration from 54.65 mM at 2.95 mbsf to 5.08 mM at 144.8 mbsf. When normalized to Cl^-, a net loss of 7 mM of Ca^{2+} and 50 mM of Mg^{2+} occurs (Fig. 14). This loss of Mg^{2+} and Ca^{2+} is mainly the result of precipitation of authigenic calcite and dolomite. During the alteration of clay minerals, Mg^{2+} and K^+ are also incorporated to form illite, according to Equation 1.

$$1.1Al_2Si_2O_5(OH)_4 + 0.8K^+ + 0.5Mg^{2+} + 1.2SiO_2 = K_{0.8}Mg_{0.5}Al_{2.2}Si_{3.4}O_{10}(OH)_2 + 1.8H^+ + 0.3H_2O. \quad (1)$$

It may be significant that as protons are produced during this reaction, these may cause enhanced dissolution of high-Mg calcite (HMC), thereby releasing Mg^{2+} to the pore fluids.

The concentration of Sr^{2+} increases rapidly to a maximum of 759 μM at 239.6 mbsf (Fig. 13). Below this depth, the Sr^{2+} slowly decreases in concentration to 730 μM at 382.7 mbsf. The increase in the concentration of Sr^{2+} is primarily a result of the dissolution of aragonite and HMC, combined with precipitation of low-Mg calcite (LMC) and dolomite. An increase in Sr^{2+} with increasing sub-bottom depth at Site 821 was greater than values at both Sites 819 and 820, suggesting that carbonate dissolution and precipitation processes were more prevalent at Site 821 than at the previous two sites. Decreases in the concentration of Sr^{2+} in the lower part of Hole 821A may be a result of the removal of Sr^{2+} during clay mineral diagenesis and of a lower rate of recrystallization in the carbonate part of the sediments.

Table 2. Interstitial water analyses data, 821.

Core, section, interval (cm)	Depth (mbsf)	pH	Alk. (mM)	Sal. (g/kg)	Cl^- (mM)	Mg^{2+} (mM)	Ca^{2+} (mM)	SO_4^{2-} (mM)	PO_4^{3-} (μM)	NH_4^+ (μM)	Si (μM)	K^+ (mM)	Sr^{2+} (μM)	Na^+ (mM)
Seawater		8.12	2.595	35.2	542.01	53.51	10.53	30.15	1.10	130	0	10.66	93	465.97
133-821A-														
1H-2, 145–150	2.95	7.52	6.996	35.8	562.86	54.65	8.61	26.19	14.80	560	312	9.04	82	486.52
2H-5, 145–150	11.85	7.40	7.160	35.2	560.96	54.11	6.25	23.54	4.20	825	170	9.37	86	484.93
3H-5, 145–150	21.35	7.32	4.817	35.2	558.12	49.38	7.80	24.47	2.40	955	153	9.79	147	487.44
4H-5, 145–150	30.85	7.59	5.086	35.2	560.02	44.40	8.05	21.73	2.80	1100	132	9.04	222	494.17
5H-5, 145–150	40.35	7.33	5.099	34.9	554.33	35.44	7.69	18.44	2.00	1599	168	8.59	329	500.81
6H-5, 145–150	49.85	7.45	5.267	33.8	551.49	29.74	6.14	15.65	1.80	2044	226	6.08	353	509.50
7H-5, 145–150	59.30	7.29	6.047	33.5	551.49	24.85	5.96	13.29	2.00	2058	172	6.38	379	515.36
8H-5, 145–150	68.85	7.48	6.144	33.5	544.86	21.25	5.51	11.69	1.80	2027	176	5.76	412	514.26
9H-5, 145–150	78.35	7.40	5.382	33.0	547.70	18.46	4.91	11.17	1.50	2229	170	5.15	437	522.65
10H-5, 145–150	87.85	7.68	5.887	32.0	543.91	15.58	4.43	9.22	1.60	2569	157	5.21	436	522.14
13H-5, 145–150	116.35	7.87	9.036	32.0	544.86	7.82	2.91	4.04	1.60	2113	141	3.59	489	535.93
17X-5, 140–150	144.80	7.89	6.330	30.2	538.22	5.08	2.32	0.00	1.10	3046	160	2.68	462	526.16
20X-5, 140–150	182.30	7.82	6.322	30.2	539.17	6.96	2.84	0.31	1.20	2239	166	3.18	548	522.25
23X-5, 140–150	210.90	8.11	5.745	30.5	542.01	5.65	2.84	0.00	1.40	2233	160	2.16	651	527.32
26X-5, 140–150	239.60			30.5	538.22	5.26	2.88	0.44	1.10	2423	151	1.79	759	519.51
29X-5, 140–150	268.50	8.20	4.360	30.2	540.12	4.74	2.66	0.11	1.10	2406	128	1.67	702	526.83
33X-5, 140–150	307.10	8.23	5.266	32.2	536.33	7.56	3.29	1.60	1.20	2598	134	1.82	612	520.04
35X-3, 140–150	323.40	8.35	3.549	30.5	538.22	5.22	3.14	0.00	1.20		105	1.44	695	522.21
38X-5, 140–150	355.30	8.10	5.012	31.5	535.38	8.71	3.79	0.83	1.90	2598	185	1.61	642	514.14
41X-4, 140–150	382.70	8.33	3.650	30.2	538.22	6.87	4.03	1.33	1.40		136	1.41	730	517.21

Note: Alk. = alkalinity; Sal. = salinity.

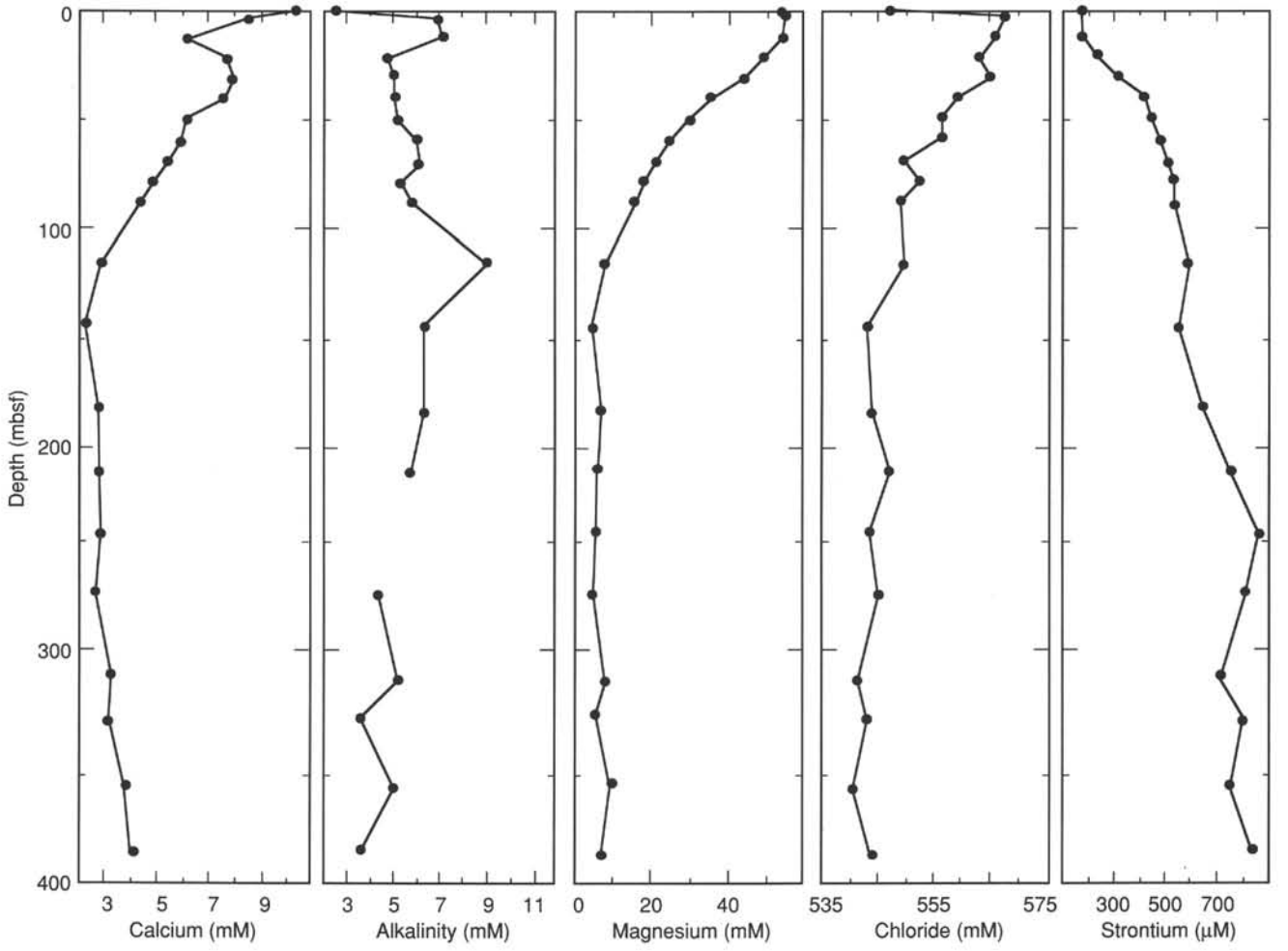

Figure 13. Concentrations of Ca^{2+}, alkalinity, Mg^{2+}, Cl^-, and Sr^{2+}, Site 821.

Table 3. Percentages of calcite, aragonite, quartz, and dolomite, Site 821.

Core, section, interval (cm)	Depth (mbsf)	Carbonate (%)
133-821A-		
1H-1, 95–98	0.95	74.20
1H-2, 145–150	2.95	67.70
1H-3, 95–98	3.95	64.70
2H-1, 95–98	5.35	55.50
2H-3, 95–98	8.35	52.50
2H-5, 95–98	11.35	45.00
2H-5, 145–150	11.85	47.10
3H-1, 95–98	14.85	55.60
3H-3, 95–98	17.85	86.50
3H-5, 95–98	20.85	69.50
3H-5, 145–150	21.35	70.20
4H-1, 95–98	24.35	73.60
4H-3, 95–98	27.35	63.50
4H-5, 95–98	30.35	44.30
4H-5, 145–150	30.85	42.90
5H-1, 95–98	33.85	34.20
5H-3, 96–98	36.86	41.50
5H-5, 96–98	39.86	84.10
5H-5, 145–150	40.35	80.40
6H-1, 95–98	43.35	78.60
6H-3, 95–98	46.35	75.40
6H-5, 95–98	49.35	57.40
6H-5, 145–150	49.85	57.60
7H-1, 95–98	52.85	66.10
7H-3, 95–98	55.85	82.40
7H-5, 95–98	58.85	68.10
7H-5, 145–150	59.35	69.00
8H-1, 100–103	62.40	33.70
8H-3, 96–99	65.36	66.40
8H-5, 96–99	68.36	68.00
8H-5, 145–150	68.85	70.90
9H-1, 15–17	71.05	63.10
9H-3, 15–17	74.05	86.10
9H-5, 15–17	77.05	82.70
9H-5, 145–150	78.35	78.10
10H-1, 22–24	80.62	70.00
10H-3, 22–24	83.62	65.60
10H-5, 22–24	86.62	69.70
10H-5, 145–150	87.85	58.30
11H-1, 20–23	90.10	61.00
11H-3, 20–23	93.10	63.00
11H-5, 20–23	96.10	80.80
11H-7, 20–23	99.10	82.50
12H-1, 17–19	99.57	51.30
12H-3, 17–19	102.57	65.10
12H-5, 17–19	105.57	75.20
13H-1, 15–17	109.05	78.60
13H-3, 15–17	112.05	76.90
13H-5, 15–17	115.05	81.40
13H-5, 145–150	116.35	87.10
13H-7, 15–17	118.05	86.50
14H-1, 10–11	118.50	79.90
14H-3, 3–4	121.43	87.60
14H-5, 3–4	124.43	87.60
15H-1, 10–13	128.00	77.70
15H-3, 10–13	131.00	78.50
15H-5, 10–13	134.00	79.60
16H-1, 8–10	137.48	81.60
16H-3, 8–10	140.48	67.30
16H-5, 8–11	143.48	78.10
17X-1, 10–12	146.00	63.30
17X-1, 145–150	147.35	75.20
17X-3, 10–12	149.00	69.70
17X-5, 10–12	152.00	71.50
18X-1, 1–2	155.61	83.00
18X-2, 9–10	157.19	80.30
18X-3, 9–10	158.69	74.90
18X-5, 9–10	161.69	75.80
19X-1, 2–4	165.22	69.50
19X-3, 2–4	168.22	58.90
19X-5, 7–8	171.27	53.60
20X-1, 11–12	175.01	72.10

Table 3 (continued).

Core, section, interval (cm)	Depth (mbsf)	Carbonate (%)
20X-3, 11–12	178.01	37.70
20X-5, 11–12	181.01	43.20
20X-5, 140–150	182.30	67.20
21X-1, 90–92	185.50	69.50
21X-3, 90–92	188.50	85.40
21X-5, 90–92	191.50	76.50
22X-1, 90–92	194.80	46.70
22X-3, 90–92	197.80	72.50
22X-5, 90–92	200.80	85.80
23X-1, 90–92	204.40	61.00
23X-3, 90–92	207.40	57.20
23X-5, 90–92	210.40	67.90
23X-5, 140–150	210.90	51.70
24X-1, 90–92	213.70	33.50
24X-3, 90–92	216.70	63.00
24X-5, 90–92	219.70	83.50
25X-1, 90–92	223.40	76.10
25X-3, 90–92	226.40	78.10
25X-5, 90–92	229.40	67.80
26X-1, 90–92	233.10	59.80
26X-3, 90–92	236.10	71.90
26X-5, 90–92	239.10	53.50
26X-5, 140–150	239.60	53.10
27X-1, 90–92	242.70	63.10
27X-3, 90–92	245.70	68.10
27X-5, 90–92	248.70	70.00
28X-1, 90–91	252.30	75.90
28X-3, 90–91	255.30	73.60
28X-5, 90–91	258.30	68.90
29X-1, 90–92	262.00	46.90
29X-3, 90–92	265.00	77.30
29X-5, 90–92	268.00	74.90
29X-5, 140–150	268.50	65.10
30X-1, 1–3	270.81	60.40
30X-3, 4–6	273.84	54.10
30X-5, 5–7	276.85	69.40
31X-1, 2–4	280.42	72.10
31X-3, 11–13	283.51	62.20
31X-5, 9–11	286.49	46.50
33X-1, 3–5	299.73	75.30
33X-3, 3–5	302.58	65.00
33X-5, 4–6	305.59	59.70
33X-5, 140–150	306.95	72.50
34X-1, 4–6	309.44	37.30
34X-3, 4–6	312.44	27.20
34X-5, 4–6	315.44	37.10
35X-1, 5–7	319.05	48.60
35X-3, 5–7	322.05	59.50
35X-5, 140–150	323.40	59.90
35X-5, 5–7	325.05	59.10
36X-1, 6–8	328.76	61.00
36X-3, 6–8	330.82	49.60
36X-5, 6–8	333.82	63.60
36X-7, 6–8	336.82	68.00
37X-1, 5–7	338.35	44.40
37X-3, 5–7	341.35	53.60
37X-5, 5–7	344.35	68.20
38X-1, 5–6	347.95	62.00
38X-3, 2–3	350.92	65.70
38X-5, 5–6	353.95	39.70
39X-1, 5–7	357.55	39.20
39X-3, 5–7	360.55	31.20
39X-5, 5–7	363.55	44.80
40X-1, 10–11	367.30	50.70
40X-3, 10–11	370.30	47.10
40X-5, 10–11	373.30	71.70
41X-1, 10–11	376.90	53.10
41X-3, 10–11	379.90	47.70
41X-5, 10–11	382.90	34.70
41X-5, 140–150	384.20	34.00
42X-1, 90–92	387.30	29.90
42X-3, 90–92	390.30	57.90
42X-5, 90–92	393.30	71.30
43X-1, 89–91	396.99	72.70
43X-2, 90–92	398.50	47.60

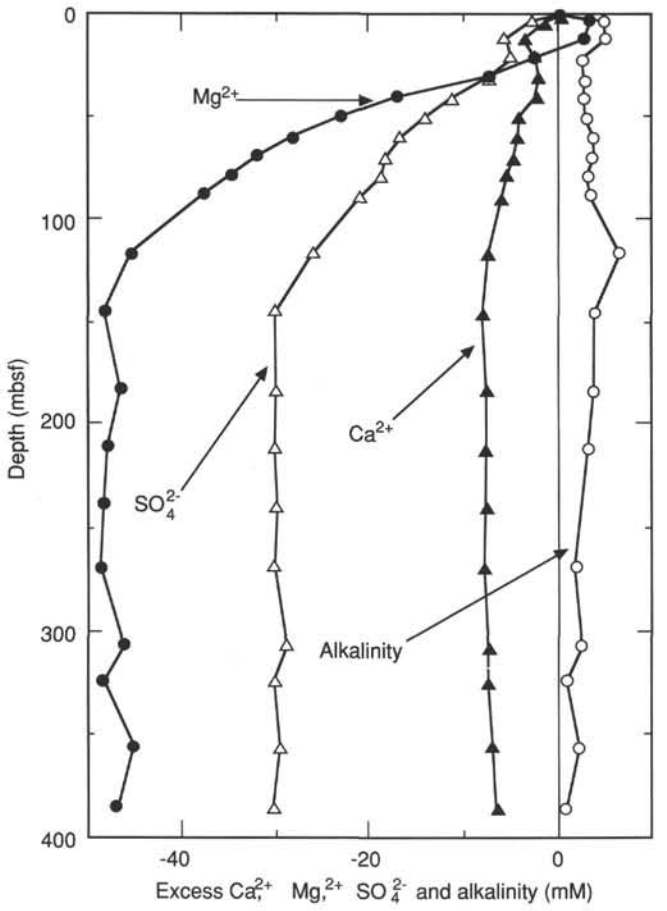

Figure 14. Changes in the concentration of SO_4^{2-}, alkalinity, Ca^{2+}, and Mg^{2+} relative to seawater Cl^- concentrations as a function of depth for Site 821.

Alkalinity, Sulfate, and Phosphate

The alkalinity increases in Hole 821A to 7.160 mM at 11.85 mbsf. It exhibits another peak of 9.036 mM coincident with the removal of sulfate at 116.35 mbsf. As at Sites 819 and 820, the alkalinity is lower than would be expected from sulfate reduction, which indicates the presence of precipitation reactions involving carbonate. Increases in phosphate and ammonia are considerably lower than expected (see "Inorganic Geochemistry," "Site 820" chapter, this volume).

Salinity and Chlorinity

The chlorinity exhibits a sharp increase in Core 133-821A-1H from seawater values to 542.01 mM. Below this depth there is a steady decrease (Fig. 13) reaching 535 mM at 355.3 mbsf. The decrease in chlorinity is insufficient to account for the change in salinity (see "Inorganic Geochemistry," "Site 819" chapter, this volume). Salinity decreases as a result of the precipitation of carbonates and the removal of sulfate through oxidation of organic material.

Carbonate Content and X-Ray Mineralogy

The carbonate content of the sediment at Site 821 varies between 10% and 90% (Table 3). Changes in the amount of carbonate occur principally as a result of dilution by terrigenous materials and are probably related to changes in the position of sea level.

Table 4. Carbonate content data, Site 821.

Core, section, interval (cm)	Depth (mbsf)	Calcite (%)	Aragonite (%)	Quartz (%)	Dolomite (%)
133-821A-					
1H-4, 145–150	5.95	36.4	51.8	11.7	0.0
2H-5, 145–150	11.85	33.5	48.6	17.9	0.0
3H-5, 145–150	21.35	39.0	55.3	5.7	0.0
4H-5, 145–150	30.85	33.2	44.5	22.3	0.0
5H-5, 145–150	40.35	30.7	59.3	5.3	4.8
6H-5, 145–150	49.85	32.1	55.3	11.7	1.0
7H-5, 145–150	59.35	25.1	43.2	14.3	17.4
8H-5, 140–150	68.80	31.7	50.5	10.6	7.2
9H-5, 140–150	78.30	32.0	52.6	7.9	7.5
10H-5, 140–150	87.80	32.9	49.7	14.5	2.9
13H-5, 140–150	116.30	35.9	48.9	2.8	12.3
17X-5, 140–150	153.50	53.5	32.9	7.6	6.0
18X-2, 9–13	157.19	41.8	35.8	9.3	13.1
20X-1, 148–150	176.38	41.4	42.3	6.2	10.1
21X-3, 90–96	188.50	62.5	14.3	5.6	17.6
23X-3, 140–150	207.90	31.5	42.8	21.7	4.1
24X-3, 90–94	216.70	36.7	44.1	11.9	7.3
26X-5, 140–150	239.60	35.9	41.2	17.7	5.2
29X-6, 140–150	270.00	50.3	28.6	8.0	13.1
30X-3, 4–6	273.84	38.3	42.5	16.1	3.1
33X-2, 140–150	302.60	20.9	27.9	11.6	39.5
35X-5, 140–150	326.40	43.3	34.8	19.1	2.8
38X-5, 140–150	355.30	46.8	38.7	14.5	0.0
39X-3, 5–8	360.25	33.1	30.8	35.6	0.5
39X-4, 4–6	361.74	31.8	30.3	36.9	1.0
40X-3, 10–13	370.30	31.2	43.6	24.5	0.6
41X-5, 140–150	384.20	30.2	37.4	30.6	1.8
42X-3, 90–96	390.30	52.0	31.2	11.8	5.0
43X-2, 90–96	398.50	35.3	32.5	17.7	14.5

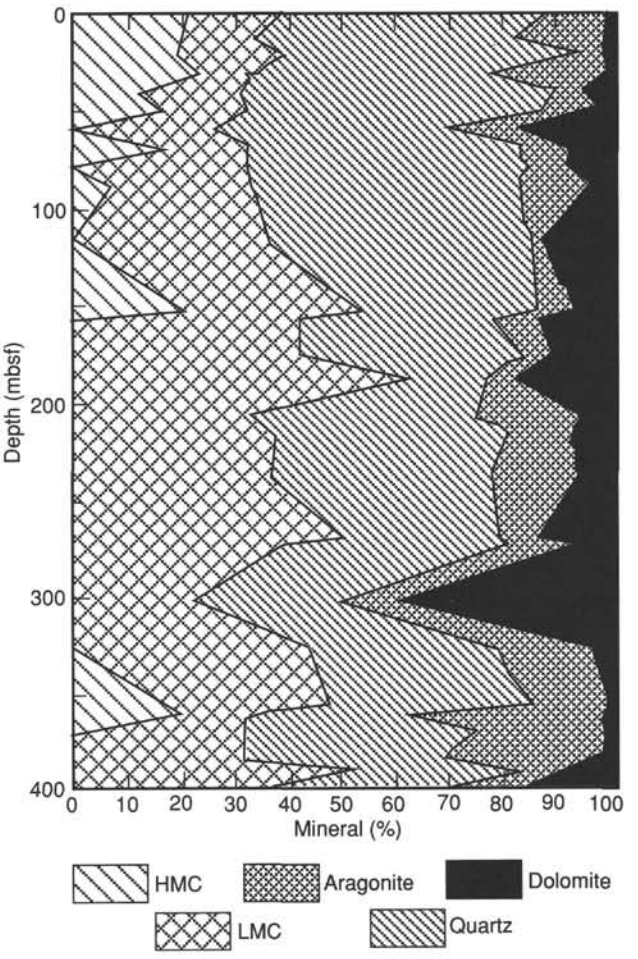

Figure 15. X-ray mineralogy data for Site 821.

Table 5. Volatile hydrocarbon data from headspace analyses, Site 821.

Core, section, interval (cm)	Depth (mbsf)	Sample	Volume (mL)	Gas chromato.	C_1 (ppm)	C_2 (ppm)	C_3 (ppm)	C_1/C_2	C_2/C_3	$C_1/(C_2+C_3)$
133-821A-										
1H-2, 145–146	2.95	HS	5	CAR132	189					
2H-5, 145–146	11.85	HS	5	CAR132	12					
3H-5, 145–146	21.35	HS	5	CAR132	7					
4H-5, 145–146	30.85	HS	5	CAR132	4					
5H-5, 145–146	40.35	HS	5	CAR132	4					
6H-5, 145–146	49.85	HS	5	CAR132	4					
7H-5, 145–146	59.35	HS	5	CAR132	4					
8H-5, 145–146	68.85	HS	5	CAR132	3					
9H-5, 149–150	78.39	HS	5	CAR132	4					
10H-5, 145–146	87.85	HS	5	CAR132	3					
11H-5, 149–150	97.39	HS	5	CAR132	3					
12H-5, 124–125	106.64	HS	5	CAR132	4					
13H-5, 145–146	116.35	HS	5	CAR132	8					
14H-5, 149–150	125.89	HS	5	CAR132	20	1		20		20
15H-5, 149–150	135.39	HS	5	CAR132	3334	3	2	1111	1.5	667
17X-5, 149–150	153.39	HS	5	CAR132	20521	8	4	2565	2.0	1710
18X-5, 149–150	163.09	HS	5	CAR132	50052	15	8	3337	1.9	2176
19X-5, 149–150	172.69	HS	5	CAR132	49293	14	9	3521	1.6	2143
20X-5, 140–141	182.3	HS	5	CAR132	54711	16	10	3419	1.6	2104
21X-5, 149–150	192.09	HS	5	CAR132	39839	11	7	3622	1.6	2213
23X-5, 140–141	210.9	HS	5	CAR132	62332	22	16	2833	1.4	1640
24X-5, 149–150	220.29	HS	5	CAR132	73788	21	15	3514	1.4	2050
25X-5, 149–150	229.99	HS	5	CAR132	61008	22	20	2773	1.1	1453
26X-5, 140–141	239.6	HS	5	CAR132	49257	14	12	3518	1.2	1895
27X-5, 149–150	249.29	HS	5	CAR132	21949	9	10	2439	0.9	1155
28X-5, 149–150	258.89	HS	5	CAR132	46761	16	17	2923	0.9	1375
29X-5, 140–141	268.5	HS	5	CAR132	68085	20	17	3404	1.2	1840
30X-5, 148–150	278.28	HS	5	CAR132	32997	11	13	3000	0.8	1375
31X-4, 149–150	286.39	HS	5	CAR132	5080	3	3	1693	1.0	847
32X-CC, 0–1	290.1	HS	5	CAR132	8573	5	7	1715	0.7	714
33X-5, 149–150	307.04	HS	5	CAR132	50271	16	18	3142	0.9	1479
34X-5, 149–150	316.89	HS	5	CAR132	9117	7	11	1302	0.6	507
35X-3, 140–141	323.4	HS	5	CAR132	15958	10	18	1596	0.6	550
36X-4, 149–150	333.75	HS	5	CAR132	9106	6	9	1518	0.7	607
37X-5, 149–150	345.79	HS	5	CAR132	18234	8	12	2279	0.7	912
38X-5, 140–141	355.3	HS	5	CAR132	20851	16	40	1303	0.4	372
39X-5, 149–150	364.99	HS	5	CAR132	16157	9	16	1795	0.6	621
40X-5, 149–150	374.69	HS	5	CAR132	9188	8	19	1149	0.4	328
41X-4, 140–141	382.7	HS	5	CAR132	9372	11	34	852	0.3	204
42X-5, 149–150	393.89	HS	5	CAR132	9927	9	18	1103	0.5	355
43X-2, 149–150	399.09	HS	5	CAR132	9461	10	28	946	0.4	243

HS = headspace sample.

Mineralogy

The sediments at Site 821 contain aragonite, LMC, HMC, dolomite, quartz, kaolinite, albite, and illite (Fig. 15 and Table 4). Dolomite is particularly abundant (10%) between 40.35 and 398.50 mbsf, coincident with the interval in which HMC is absent. This association lends credence to the speculation that HMC may provide the source for the Mg^{2+} needed for dolomitization. Similar associations between the occurrence of HMC and dolomite were noted at Sites 819 and 820. On the basis of the calculations of Swart and Guzikowski (1988), one can estimate that the dissolution of 40% HMC might provide enough Mg^{2+} to form 16 wt% dolomite. A further source of Mg^{2+} may be provided by diffusion along concentration gradients from the overlying seawater, provided that the dolomite forms at a shallow depth.

ORGANIC GEOCHEMISTRY

In addition to safety monitoring for hydrocarbons, the main purpose of the shipboard organic geochemistry studies at Site 821 was to assess the amount and origin of the organic matter preserved in the Pleistocene mixed sediments deposited in front of the present-day Great Barrier Reef. The second purpose was the characterization of the proportions of different light hydrocarbons generated in the sediments through biogenic or thermogenic decay of organic matter.

Samples

Forty-one samples were collected from Hole 821A at 10-m intervals over the depth range from 3 to 399 mbsf. All sediments were analyzed for their composition of light hydrocarbons (C_1–C_6) using headspace analyses, and for total nitrogen, sulfur, and carbon, using a NA 1500 Carlo Erba NCS analyzer.

Volatile Hydrocarbons

Hydrocarbon gases (C_1–C_6) in sediments were analyzed as part of ODP's safety and pollution-prevention monitoring program, using the headspace technique, the Carle gas chromatograph (for determination of C_1–C_3 concentrations), and the NGA gas chromatograph (mainly for determination of C_4–C_6 concentrations). The results of 41 headspace analyses from Hole 821A are presented in Table 5. In Figure 16, the WSTP-temperature data from Sites 817 and 820 are shown with the geothermal gradient used at Site 821 for the interpretation of the depth-related evolution of the C_1/C_2 ratio.

The sediments at Site 821 contained high concentrations of methane, which represented no safety and/or pollution haz-

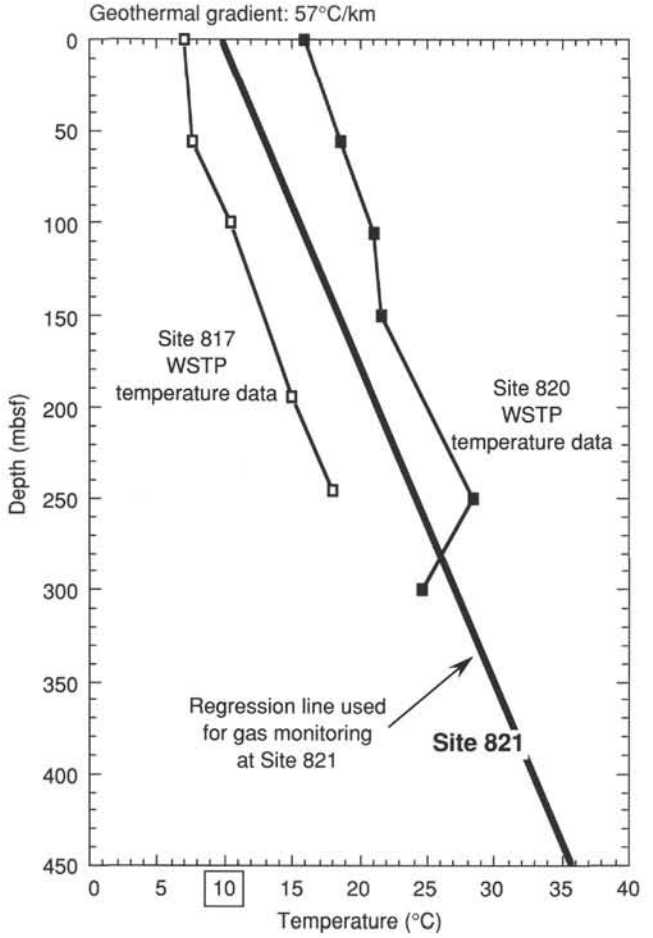

Figure 16. WSTP-temperature data from Sites 817 and 820, geothermal gradient, and approximate seafloor temperature at Site 821.

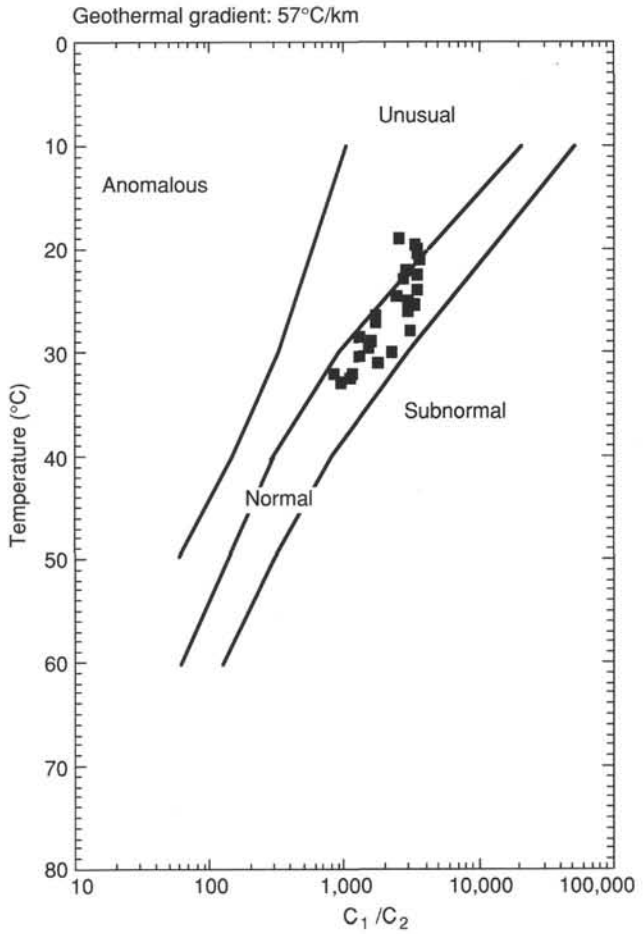

Figure 17. Distribution of the C_1/C_2 ratio from headspace analyses with temperature at Hole 821A. This diagram was compiled for the shipboard safety and pollution-prevention monitoring program.

ards. The evolution of the C_1/C_2 ratio with increasing depth and temperature did not show any anomalous trend (Fig. 17), and the values ranged between 3,600 and 800 (normal trend between 19°C and 33°C).

Headspace gas concentrations of methane were low to moderate (ranged between 3 and 190 ppm) in the sulfate reduction zone (Fig. 18, see also "Inorganic Geochemistry" section and Fig. 14), but increased rapidly below 130 mbsf. The concentrations reached a maximum value at 220 mbsf (74,000 ppm in Sample 133-821A-24X-5, 149–150 cm), and progressively decreased below this depth. Propane appeared together with ethane at 135 mbsf (Fig. 18). Their concentrations did not exceed 40 ppm and follow the trend of the methane concentrations. Between 135 and 225 mbsf ethane concentrations were higher than the propane concentrations (C_2/C_3 values progressively decreased between two and one). Between 230 and 310 mbsf $C_2/C_3 = 1$, and below this depth the propane concentrations exceeded ethane (C_2/C_3 ratio <1).

The observed coincidence between low sulfate concentrations and high amounts of methane (>10,000 ppm) and a trace amount of ethane/propane in the sediments suggests a bacterial origin of methane (and ethane/propane?) in the sulfate-free section (between 145 and 250 mbsf) of the sediments at Site 821 (Fig. 19). Below 250 mbsf, the progressive increase of propane content and the decrease of both the C_2/C_3 and $C_1/(C_2+C_3)$ ratio at shallow depth and low temperature (Figs. 18 and 19) are factors that seem to indicate the beginning of a mixing with thermogenic free-hydrocarbons.

Important variations of the gas concentrations were observed between 280 and 310 mbsf corresponding to sharp changes in the porosity of the sediments (see also "Physical Properties" section and Fig. 20): a decrease was observed in the dolomitized chalks (bottom of Unit IV), and below this cap an increase in the more porous chalks (top of Unit V, see also "Lithostratigraphy" section, Fig. 6, this chapter).

Organic Carbon Contents

The total organic carbon (TOC) and total inorganic carbon contents together with the total nitrogen and sulfur concentrations recorded in Site 821 are presented in Table 6.

The amount of organic carbon at Site 821 varied between very low (<0.25% TOC) and low values, not exceeding 0.45% TOC, and the average values remained relatively constant in the different lithologic units (Fig. 21).

In the first 140 m, corresponding to the sulfate reduction zone and to lithologic Unit I, the total sulfur concentrations in sediments were below the detection limits of the NCS analyzer (Table 6). Below this depth the sulfur content varied between 0.1% and 0.6% (average value = 0.2%)

The total nitrogen concentrations in sediments of lithologic Unit I were very low (<0.05%), but increased progressively to 0.08% between 120 and 398 mbsf (Fig. 21).

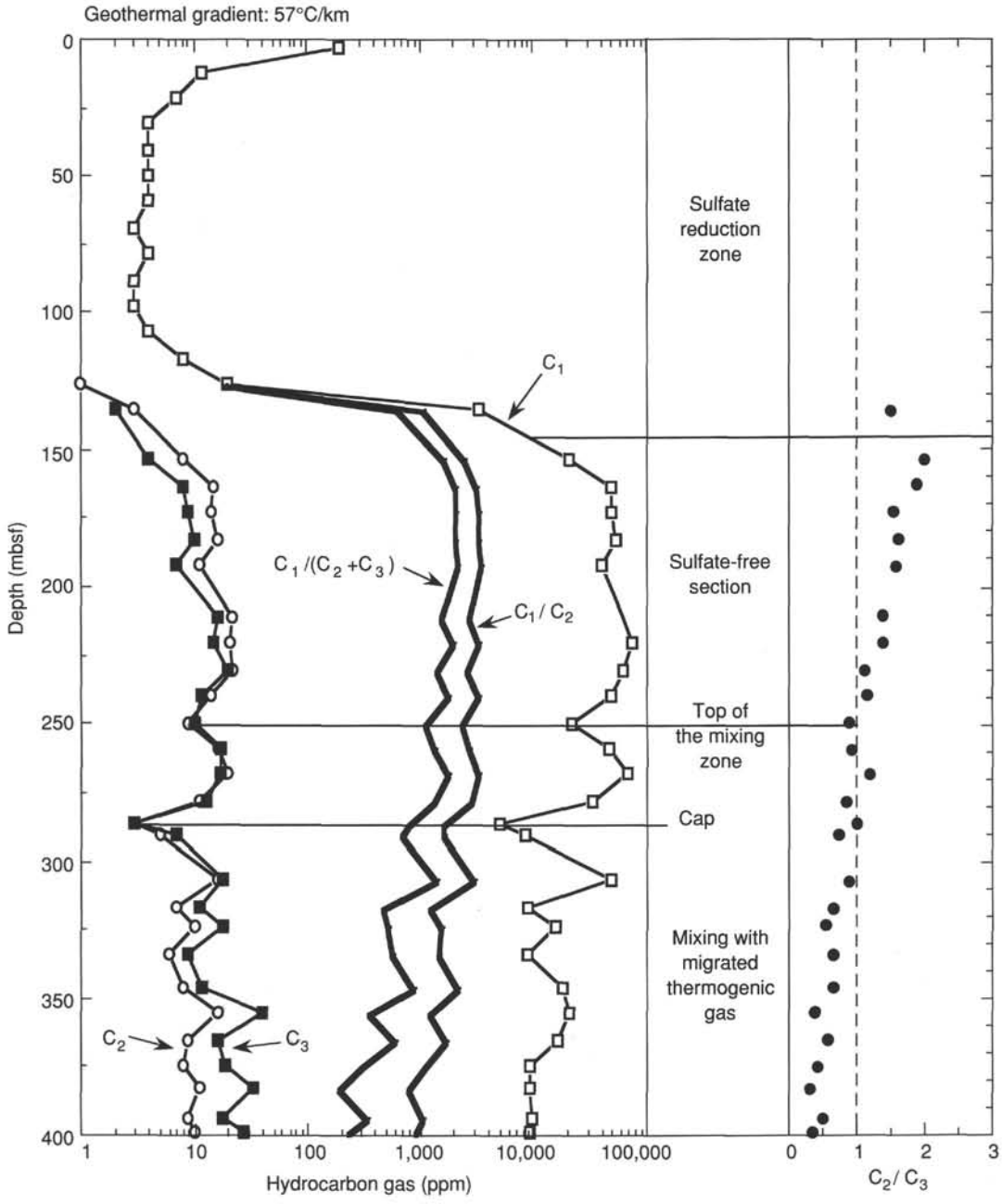

Figure 18. Distribution with depth of the amounts of hydrocarbon gas in headspace samples at Hole 821A. Evolution of C_1/C_2, C_2/C_3, and $C_1/(C_2+C_3)$ ratios.

On the basis of the TOC/nitrogen ratios (Fig. 21) marine organic matter is abundant below 120 mbsf in all the bioclastic and mixed sediments encountered at Site 821. There was mixing of terrestrial organic materials within the autochthonous organic matter above the *Halimeda* rudstone horizon, in the more siliciclastic Pleistocene sediments of Unit I. As a consequence of the low organic contents, we were unable to conduct detailed geochemical characterization of kerogen types using the Rock-Eval pyrolysis method, as originally planned. More detailed shore-based studies (elemental analysis and optical investigations on extracted kerogens) will permit characterization of the short-term fluctuations in the vertical distribution and preservation of the different components of the organic matter in the sediments encountered at Site 821.

PHYSICAL PROPERTIES

Physical properties analyzed in cores from this site include bulk density, *P*-wave velocity, and magnetic susceptibility on unsplit cores and *P*-wave velocity, electrical-resistivity formation factor, shear strength, and index properties (including bulk density, grain density, water content, porosity, and void ratio) on split cores. The methods used are described in detail in the "Explanatory Notes" chapter (this volume).

Bulk Density

Bulk densities for Site 821 were determined from volume and mass measurements on discrete core samples and from absorption of gamma rays by whole-round cores (Figs. 22 and

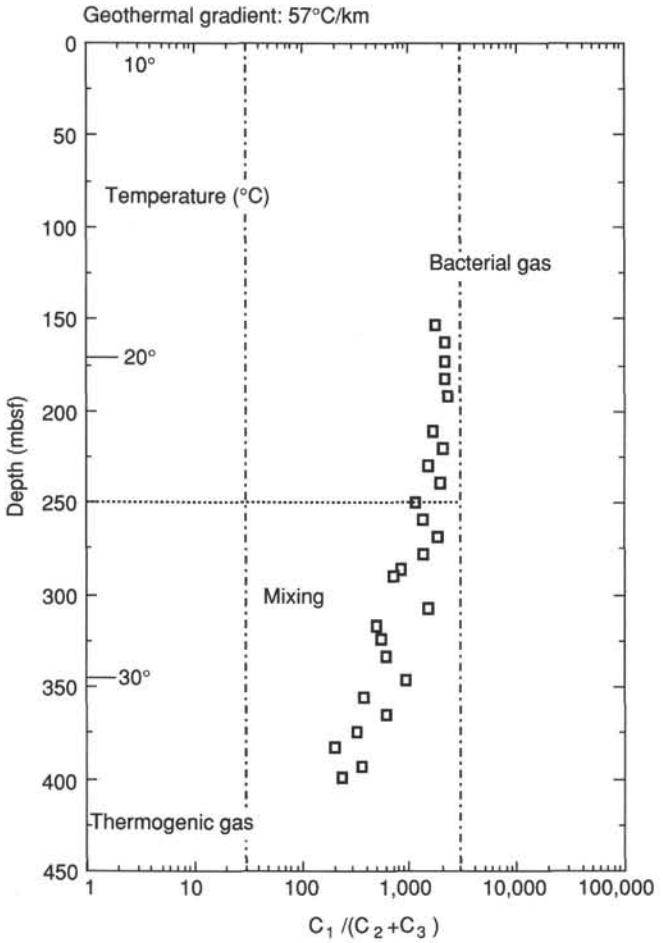

Figure 19. Evolution with depth and temperature of the $C_1/(C_2+C_3)$ ratio at Hole 821A.

23A and Table 7). After an initial increase in density with depth in the upper 100 mbsf, density increases much more slowly with depth. This increase in density is primarily a function of decreasing porosity resulting from increasing overburden with depth (see the discussion of porosity below).

P-Wave Velocity

P-wave velocities were measured on whole round cores using the multisensor track (MST) and on discrete core samples using the Hamilton Frame (Table 8 and Fig. 24A). As indicated in Figure 24, velocity is to some extent correlated with shear strength in that major low velocity peaks correlate with low shear strength peaks while the general increase in velocity with depth parallels the increase of shear strength with depth.

Porosity

Porosity was one of the index properties determined from discrete core samples using the mass balance and the pycnometer (Table 7). A graph of porosity vs. depth (Fig. 23B) depicts a comparison of the porosity measured for samples from split cores and from wireline logging. Much of the fine structure as well as the overall trend of the porosity-depth function is seen in both the wireline log and the core sample measurements, though some differences in detail and in amplitude of variations exist. High-porosity zones tend to be regions where calipers indicate that the hole has washed out to larger than normal size. This change in hole size accentuates the wireline log porosity estimates. In addition, Figure 23B exhibits an apparent correlation of peaks in porosity with lows in calcium carbonate content. However, Figure 25 indicates that overall the concentration of calcium carbonate does not correlate with porosity. In Figure 25, the expected strong correlation of porosity to bulk density is shown. The degree of correlation is a measure of the internal consistency of our measurements of density and porosity since both quantities are measured on the same sample, but the density involves both a mass and a volume measurement while the porosity involves only the latter.

Now that we have accumulated data from several sites, we have begun to recognize trends in the porosity data. Plots of porosity vs. depth for Site 815 in Figure 26 show that the general trend of porosity vs. depth at Site 815 is best represented by a linear regression of ln porosity on ln depth. Site 821 is similar to Site 820 in that a linear regression of ln porosity on ln depth is marginally better at describing the data than either the linear regression of porosity on depth or ln porosity on depth (Fig. 26B). These general trends are summarized in Figure 20, where we plotted normal compaction curves for all sites analyzed to date. Sites 820 and 821 have almost identical normal compaction curves, while Site 819 has a slightly divergent trend. Site 815 is more divergent, followed by Site 817, which is the most different from Sites 820 and 821. This trend parallels trends in sediment composition, where Site 817 is almost totally carbonate compared with a large admixture of terrigenous sediments at the other sites. We are not clear at present why Site 819 differs from Sites 820 and 821.

Electrical-Resistivity Formation Factor

We measured the formation factor (FF) in cores from Hole 821A (see Table 9 and Fig. 24D). Peaks in FF correlate with troughs in sonic velocity as well as with lows in shear strength in a number of cases. This probably is a consequence of the high water content that controls these three variables to some extent.

Shear Strength

We measured shear strength in the upper section of this hole (Table 10 and Fig. 24C). A suggestion that shear strength lows correlate with peaks in FF and lows in sonic velocity, might be expected if water content to controlled all three of these variables.

Physical Properties Conclusions

Sediment physical properties at Site 821 allow one to characterize the sediments into three basic physical property units. Unit A extends from the seafloor to 40 mbsf and consists predominantly of calcareous ooze. Physical properties showed a normal compaction trend of soft sediment. Unit B includes the interval from 40 to 300 mbsf and is composed of calcareous mudstone, chalk, and dolomitized wackestone. The compaction trend showed a more gentle slope than the Unit A (Figs. 23, 24, and 25). *P*-wave velocity exhibited a significant amount of the variation in this unit because of the occurrence of unsaturated foraminifer ooze. Vane shear strengths exhibited large variations that we found correlated with the occurrence of compacted gassy sediments. Unit C, which extends from 300 to 400 mbsf, consists of dolomitized calcareous sandstone and mudstone. Physical properties exhibited a significant amount of variation through this unit (Figs. 23 and 25) because of lithology and, for the most part, were invariant with depth. Two significant bulk density troughs were observed at 320 and 360 mbsf (Fig. 23) that may result from the occurrence of clay-rich mudstone. Values for the physical properties of this unit remained relatively constant throughout the section.

Water content and porosity showed a good inverse correlation with bulk density (Fig. 26). WE found that variations in these properties correlated with changes in sediment composition, especially the amount of clay.

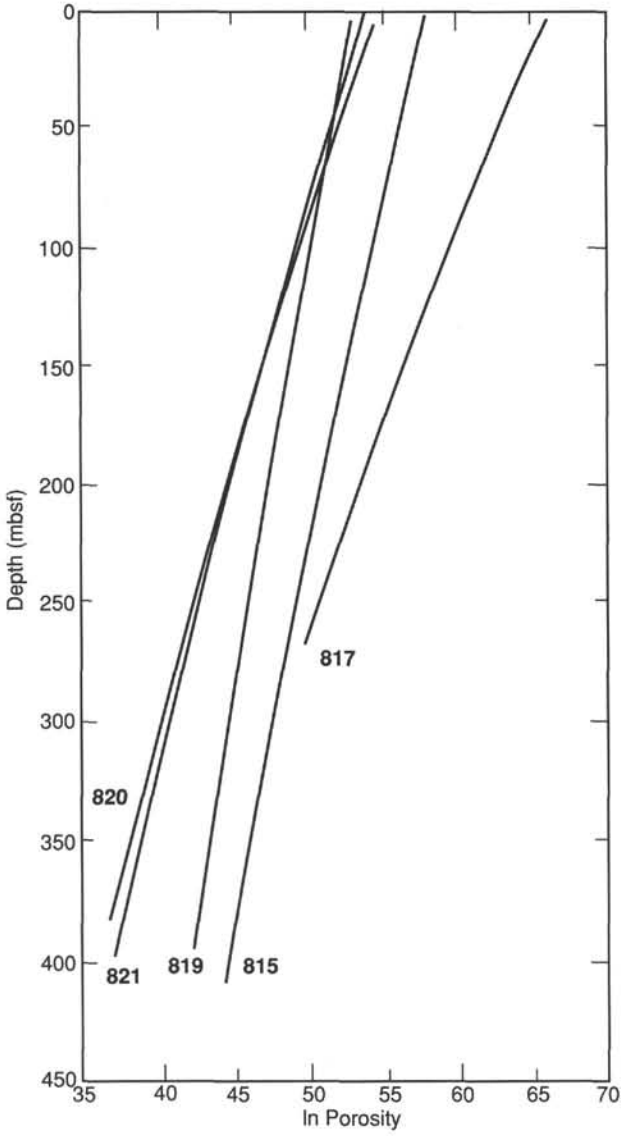

Figure 20. Generalized normal compaction curves for Sites 815, 817, 819, 820, and 821, obtained by linear regression of ln porosity on depth.

DOWNHOLE MEASUREMENTS

Log Reliability

Hole size is the most important control on accuracy of logs from Leg 133, and hole size at Hole 821A was the most uniform of any Leg 133 site to-date. Three types of caliper were obtained: an apparent caliper (Fig. 27) calculated from the sonic log (see "Explanatory Notes" chapter, this volume), a caliper (Fig. 27) from the Mechanical Caliper Device (MCD), and a two-axis caliper (Fig. 28) from the Formation MicroScanner (FMS). The lithodensity tool caliper was not operational at this site. The FMS caliper is much more reliable than the sonic and MCD calipers. Based on correlation of largest caliper values with anomalously low density values (Fig. 28), we suspect that occasional lowest-density portions of the lithodensity run are unreliable because of insufficient pad contact against the borehole wall. As discussed later, this pattern implies that porosity and Archie *m* calculations will be in error in these zones (Fig. 29). Most other logs do not require pad contact and therefore are relatively insensitive to the changes in borehole size. Two minor exceptions are the spectral gamma-ray and resistivity logs, which are likely to be changed slightly by post-cruise borehole correction.

As is often the case with ODP holes, the initial sonic logs from Hole 821A exhibited a few zones in which cycle skipping caused unreliable swings in apparent velocity. Reprocessing (see "Explanatory Notes" chapter, this volume) appears to have removed all unreliable data, and we consider the reprocessed velocity log of Figure 28 to be of good quality. For the short interval 376.2–392.8 mbsf at the bottom of the hole, resistivity logs but not sonic logs are available, because the resistivity tool is much lower on the tool string. A pseudosonic log was generated and used for this interval, based on regression of sonic transit time on logarithm of shallow resistivity for the overlying interval 333.7–376.1 mbsf ($R = -0.86$).

The spectral gamma-ray tool is the only tool on the seismic stratigraphic combination that can provide useful formation data even through pipe. At Hole 821A, through-pipe spectral gamma-ray logs were obtained for the interval 0–65.3 mbsf; however, we have not undertaken pipe correction of these logs yet.

Velocity, Resistivity, and Density Relations

Velocity, resistivity, and density are strongly correlated throughout almost all of the logged interval at Hole 821A (Fig. 28). This correlation arises from a porosity dominance of all three logs. The changes in velocity and density with depth (Fig. 28) generally follow a gradual compaction profile, suggesting that mechanical compaction is dominant over diagenesis in controlling porosity at this site. Similar patterns were observed at Sites 814, 817, 819, and 820 (see "Site 814", "Site 817", "Site 819", and "Site 820" chapters, this volume). Velocity and density within the open-hole logged interval are somewhat greater than are normally observed in terrigenous or calcareous sediments of comparable depths. Average velocity increases from 1.7 km/s at 70 mbsf to 2.3–2.4 km/s at 370–390 mbsf, compared to typical values for these depths of 1.55–1.60 and 1.9–1.95 km/s (Hamilton, 1979). Density increases very little, from 1.95 g/cm^3 at 80 mbsf to 2.1–2.2 g/cm^3 at 320–385 mbsf, compared to typical values for these depths of about 1.64 and 1.98 g/cm^3 (Hamilton, 1976). These values for density and porosity at Site 821 are similar to those at nearby Site 820 (see "Site 820" chapter, this volume).

The density log was used to calculate the Archie *m* (Fig. 29) to assess possible changes in style of pore structure (see "Site 817" chapter, this volume). Although the Archie (1942) relationship may not be applicable in this lithology, one can identify a trend for further study. For example, the density log has five intervals that may be affected by poor pad contact. These washouts where the density is in error have anomalously high values of *m*. If pore morphology changes with lithology, then *m* will vary and can be used as an additional indicator. Velocity and resistivity ratios (Fig. 30) are similarly useful in identifying changes in pore morphology and styles of cementation.

The velocity log has been converted to an integrated traveltime log (Fig. 31), to facilitate depth-to-time conversion for comparison of Site 821 data with seismic facies. For the unlogged interval between the seafloor and 66.2 mbsf, we used a simple linear interpolation between water velocity at the seafloor and the first log value at 66.2 mbsf. We subjectively estimate an error of less than 6 ms associated with uncertainties of velocities in the top 66.2 mbsf. A checkshot survey at nearby Site 820 (see "Site 820" chapter, this volume) showed <1 ms error in a 241 m interval of integrated sonic log. However, it also showed that the linear interpolation for unlogged shallow sediments led to traveltimes that were too slow by 5 ms.

Table 6. Concentrations of total organic carbon, inorganic carbon, total carbon, total nitrogen, and sulfur in headspace samples from Site 821.

Core, section, interval (cm)	Depth (mbsf)	Sample	Total organic carbon (%)	Total inorganic carbon (%)	Total carbon (%)	Total nitrogen (%)	Total sulfur (%)	TOC/ nitrogen	TOC/ sulfur
133-821A-									
1H-2, 145–150	2.95	XRD	0.4	8.13	8.53	0.20	0	20	
2H-5, 145–150	11.85	XRD	0.16	5.66	5.82	0.02	0	8	
3H-5, 145–150	21.35	XRD	0.32	8.43	8.75	0.02	0	16	
4H-5, 145–150	30.85	XRD	0.33	5.15	5.48	0.03	0	11	
5H-5, 145–150	40.35	XRD	0.2	9.65	9.85	0.01	0	20	
6H-5, 145–150	49.85	XRD	0.42	6.91	7.33	0.03	0	14	
7H-5, 145–150	59.35	XRD	0.28	8.28	8.56	0.03	0	9.3	
8H-5, 145–150	68.85	XRD	0.2	8.51	8.71	0.01	0	20	
9H-5, 145–150	78.35	XRD	0.23	9.38	9.61	0.02	0	11	
10H-5, 145–150	87.85	XRD	0.35	7	7.35	0.03	0	11	
11H-3, 20–23	93.1	PP	0.3	7.56	7.86	0.02	0	15	
12H-3, 17–19	102.57	PP	0.29	7.82	8.11	0.02	0	14	
13H-5, 145–150	116.35	XRD	0.4	10.46	10.86	0.02	0	20	
14H-3, 3–4	121.43	PP	0.11	10.52	10.63	0	0		
15H-3, 10–13	131	PP	0.06	9.42	9.48	0.02	0	3	
16H-3, 8–10	140.48	PP	0.07	8.08	8.15	0.04	0.23	2	0.03
17X-1, 145–150	147.35	XRD	0.35	9.03	9.38	0.04	0.03	8.7	11
18X-2, 9–10	157.19	PP	0.26	9.64	9.9	0.04	0.09	6.5	2.9
19X-3, 2–4	168.22	PP	0.26	7.07	7.33	0.06	0.36	4.3	0.72
20X-5, 140–150	182.3	XRD	0.25	8.07	8.32	0.05	0.17	5	1.5
21X-3, 90–92	188.5	PP	0.19	10.25	10.44	0.05	0.14	3.8	1.3
22X-3, 90–92	197.8	PP	0.13	8.7	8.83	0.07	0.11	1.8	1.2
23X-5, 140–150	210.9	XRD	0.21	6.21	6.42	0.06	0.07	3.5	3
24X-3, 90–92	216.7	PP	0.26	7.56	7.82	0.04	0.14	6.5	1.8
25X-3, 90–92	226.4	PP	0.16	9.37	9.53	0.05	0.06	3.2	2.6
26X-5, 140–150	239.6	XRD	0.15	6.38	6.53	0.06	0.24	2.5	0.62
27X-3, 90–92	245.7	PP	0.2	8.18	8.38	0.04	0.25	5	0.8
28X-3, 90–91	255.3	PP	0.18	8.83	9.01	0.06	0.14	3	1.3
29X-5, 140–150	268.5	XRD	0.23	7.81	8.04	0.06	0.43	3.8	0.53
30X-3, 4–6	273.84	PP	0.17	6.49	6.66	0.06	0.08	2.8	2.1
31X-3, 11–13	283.51	PP	0.42	7.47	7.89	0.05	0.18	8.4	2.3
33X-5, 140–150	306.95	XRD	0.01	8.7	8.71	0.06	0.07	0.1	0.1
34X-3, 4–6	312.44	PP	0.26	3.26	3.52	0.06	0.09	4.3	2.9
35X-3, 140–150	323.4	XRD	0.32	7.19	7.51	0.06	0.09	5.3	3.5
36X-3, 6–8	330.82	PP	0.19	5.96	6.15	0.06	0.23	3.1	0.82
37X-3, 5–7	341.35	PP	0.23	6.43	6.66	0.06	0.23	3.8	1
38X-5, 140–150	355.3	XRD	0.37	4.43	4.8	0.08	0.09	4.6	4.1
39X-3, 5–7	360.55	PP	0.3	4.04	4.34	0.08	0.37	3.7	0.81
40X-3, 10–11	370.3	PP	0.23	5.65	5.88	0.07	0.08	3.3	2.9
41X-5, 140–150	384.2	XRD	0.37	4.08	4.45	0.08	0.12	4.6	3.1
42X-3, 90–92	390.3	PP	0.3	6.95	7.25	0.07	0.14	4.3	2.1
43X-2, 90–92	398.5	PP	0.35	5.71	6.06	0.08	0.58	4.4	0.6

PP = physical properties sample; XRD = X-ray diffraction sample.

Log-Based Units

Lithostratigraphy at Site 821 is dominated by variations in concentration of two principal components: carbonate (either nannofossils or micrite) and clay minerals. This conclusion is based on smear-slide descriptions (see "Lithostratigraphy" section, this chapter); it was independently demonstrated at nearby Site 820 by geochemical logs (see "Site 820" chapter, this volume).

In general, the three porosity-sensitive logs are moderately well correlated with the spectral gamma-ray log (SGR in Fig. 27), with gamma-ray maxima corresponding to velocity, resistivity, and density minima. This pattern implies a substantial effect of mineralogy on porosity. This pattern is typical in ODP of clay-mineral variation. Higher clay-mineral concentration is evidenced by higher gamma-ray counts, particularly if illite (3%–8% potassium; Serra, 1986) is a significant constituent of the clays, and clay minerals substantially increase the porosity of uncompacted (<2 km overburden) sediments. Diagenesis can augment or diminish this correlation between high clay content and high porosity. Augmentation occurs if diagenesis is more extensive in carbonate-rich beds than in clay-rich beds due to higher permeability or local dissolution/precipitation. Diminishment occurs if there is preferential precipitation in clay-rich beds.

The spectral gamma-ray values at Site 821 are similar to those at Site 819 and 820, which are in turn substantially higher than at previous sites on Leg 133. The potassium in particular has increased by more than a factor of 10, to values ranging from 0.5% to 1.0%. Thorium values increased by a factor of three, while the total SGR count was nearly double that at Site 817 (see "Site 817" chapter, this volume), with values in the range of 30 to 50 API units. These patterns can be attributed to the much higher clay content and proportionately lower carbonate content at Sites 819, 820, and 821, in comparison to earlier Leg 133 sites.

On the basis of log responses, the open-hole logged interval of Site 821 was divided into three units and several subunits: log Unit 1 from the base of the pipe (65 mbsf) to 210 mbsf, log Unit 2 from 210 to 293 mbsf, and log Unit 3 from 293 mbsf to the bottom of the logged interval at 392 mbsf.

Log Unit 1 (<65–210 mbsf) includes calcareous mudstones and chalks corresponding to lithologic Units I, II, and III (0–215 mbsf; see "Lithostratigraphy" section, this chapter). Log Unit 1 is characterized by a smooth compaction

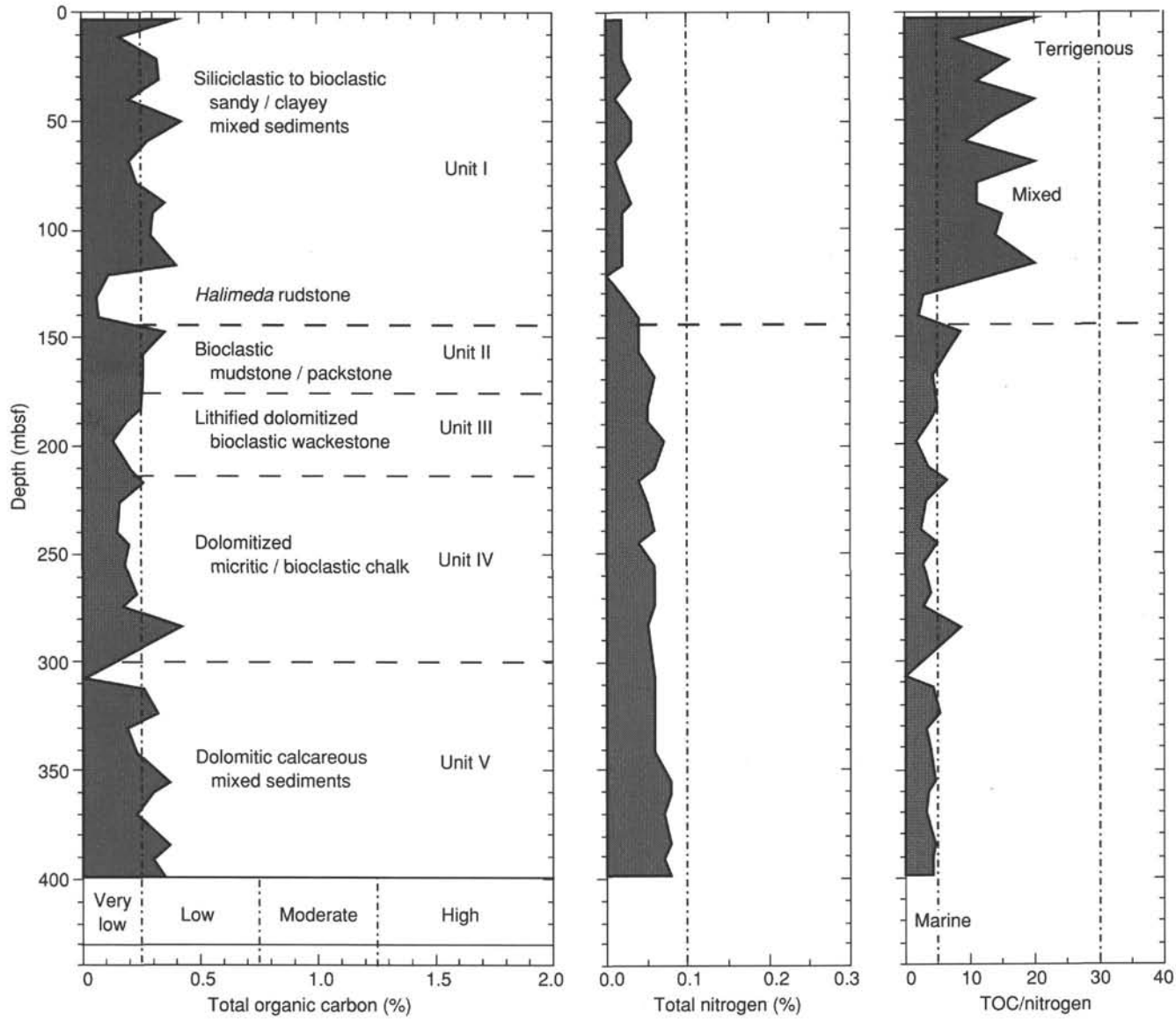

Figure 21. Distribution with depth of concentrations of total organic carbon and nitrogen and of TOC/nitrogen ratio in headspace samples from Hole 821A.

profile for the velocity and resistivity logs as shown in Figure 28. Punctuating this broad pattern is a regular sawtoothed pattern of apparently upward-fining beds, 4– to 14-m thick. A sawtoothed pattern is most evident in resistivity logs and subtle-to-absent in spectral gamma-ray and potassium logs (Fig. 27). We attribute this difference to the much higher signal-to-noise ratio of resistivity than spectral gamma rays or potassium, particularly at the high logging speed used for the seismic stratigraphic combination tool. On the basis of patterns seen at Site 820 (see "Site 820" chapter, this volume), where spectral gamma-ray logs had a higher signal-to-noise ratio than at Site 821, we speculate that these cycles of upward-increasing porosity were caused by an increase in the proportion of clay minerals and a decrease in carbonate contents.

Log Unit 2 (210–293 mbsf) corresponds with lithologic Unit IV (215–299 mbsf); interbedded dolomitized chalks and bioclastic packstone-wackestone (see "Lithostratigraphy" section, this chapter). Resistivity (Fig. 29) in log Unit 2 exhibits a sawtoothed pattern of beds increasing in porosity up the section, much like log Unit 1, except that the beds are usually thicker (10–20 m). Gamma rays are generally positively correlated with resistivity and velocity in this unit (Fig. 27); this pattern is opposite to that normally observed and indicates that intervals rich in clay minerals are lower in porosity, presumably due to diagenesis. Little or no evidence of a compaction pattern occurs in this unit (Fig. 28), again suggesting the importance of diagenesis.

Further evidence for diagenesis in log Unit 2 is shown in Figure 30, where the ratios of velocity and resistivity have been normalized with respect to seawater, and the resulting ratios divided to create the *A/B* ratio (see "Site 817" chapter, this volume). This ratio can be used to identify sections (such as the one from 261 to 270 mbsf) where values have increased as a result of a substantial relative reduction in resistivity. Previously, this form of response has been associated with dolomitization of porous facies (see "Site 817" chapter, this volume). Shipboard scientists suggested that this dissolution caused increased porosity to which the resistivity logs responded, while cementation may account for the relatively high compressional

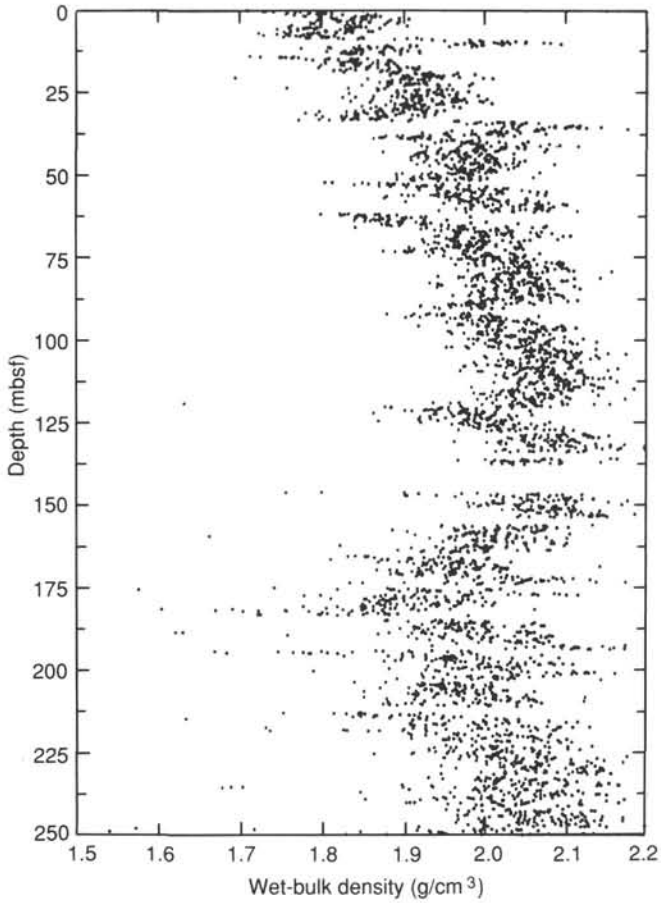

Figure 22. GRAPE bulk density measurements for Site 821. Data values have been averaged at 5-cm intervals.

wave velocity. Thus, we have interpreted this response between 261 and 270 mbsf as having been caused by cementation, which agrees with the increase in dolomitization observed in the cores (see "Lithostratigraphy" section, this chapter).

Log Unit 3 (293 to at least 392 mbsf) corresponds with lithologic Unit V (299–400 mbsf), which consists of coarsening-upward cycles of calcareous sandstone and calcareous mudstone (see "Lithostratigraphy" section, this chapter). At least four such cycles are visible in the logs: 362–340 mbsf, 340–330 mbsf, 330–318 mbsf, and 318–293 mbsf. The gamma-ray log typically is inversely correlated with resistivity and velocity in this unit, in contrast to the pattern in Log Unit 2 but consistent with the pattern at Site 820 of higher clay-mineral abundance causing higher porosity (see "Site 820" chapter, this volume).

The logs do not directly establish that the cycles in log Unit 3 are coarsening upward, but instead that they are decreasing in clay-mineral content and porosity upward. However, within each upward-coarsening be, some tendency exists for the Archie component m to decrease upward (Fig. 29). Such a trend might be caused by a decrease in the proportion of clay minerals, which should result in the shape of the particles being less platy; this is known to decrease the value of m. These are relatively subtle trends at this site, but they can be taken as an indication of upward-coarsening owing to the often observed decrease in grain size with increasing content of platy clay minerals. These log-based upward-coarsening sequences are discussed in more detail in the "Lithostratigraphy" section (this chapter). A good example of changing style of cementation can be seen at the top of Log Unit 3 from 295 to 300 mbsf, where the *A/B* ratio (Fig. 30, described above) is high at a point of high velocity and low resistivity, thus indicating that an increase in cementation is probable. Other zones having a high *A/B* ratio occur; however, these are associated with low velocities and thus do not immediately indicate an increase in cementation. Post-cruise research is planned for evaluating these trends in terms of diagenesis and sedimentological processes to produce more comprehensive lithological correlations.

Temperature

The Lamont-Doherty Geological Observatory (LDGO) temperature tool was run at the bottom of the seismic stratigraphic tool string. Because the hole temperatures have been reduced by circulation during coring and by hole conditioning immediately prior to logging, it is not possible to infer an equilibrium thermal profile from a single temperature logging run. Thus, our recorded maximum temperature of 28.6°C is a minimum estimate of equilibrium temperature.

The temperature tool was run not to estimate heat flow, but in case fluid flow was present. In Figure 32, temperature has been measured as a function of pressure recorded simultaneously by the tool. Depths shown are approximate and may be revised by up to 5 m by post-cruise merging of Schlumberger time/depth data with LDGO time/pressure data.

The temperature pattern in Figure 32 exhibits evidence of thermal lags from a mud-clogged end sub. Mud clogging can occur when the temperature tool, which is the bottom tool on the tool string, hits the bottom of a hole that contains sticky clay. The effect on the log is a higher temperature for the upgoing log than for the downgoing log, and a maximum temperature recording, not at the deepest point in the hole, but somewhat shallower than the deepest point on the upgoing log. When rigged down after logging, the temperature tool did have a mud-clogged end sub.

The downgoing log probably has been minimally affected, while the upgoing log is probably somewhat affected by mud clogging. This pattern indicates an approximately linearly increasing temperature between the base of pipe and the bottom of the hole. Both logs indicate that through-pipe temperatures are significantly cooler than those of the adjacent open hole. The extrapolated bottom-water temperature (based on observed sub-bottom thermal gradient) is substantially warmer than the observed bottom-water temperature (Fig. 32). This discrepancy might be caused by either upward flux of pore fluids out of the formation or by bottom waters that are presently cooler than average; the latter seems more likely in these shallow waters.

Hole Deviation

At Hole 821A, the hole deviation measured by the FMS ranges from 0.2° to 1.1° (Fig. 33). Azimuth of this very small deviation ranges from south to west.

SEISMIC STRATIGRAPHY

For a discussion, see "Seismic Stratigraphy" section, "Site 819" chapter (this volume).

SUMMARY AND CONCLUSIONS

For a discussion of this site, see "Summary and Conclusions" section, "Site 819" chapter (this volume).

REFERENCES

Archie, G. E., 1942. The electrical resistivity log as an aid in determining some reservoir characteristics. *J. Pet. Tech.*, 5:1–8.

Hamilton, E. L., 1976. Variation of density and porosity with depth in deep-sea sediments. *J. Sediment. Petrol.*, 46:280–300.

_____, 1979. Sound velocity gradients in marine sediments. *J. Acoust. Soc. Am.*, 65:909–922.
Serra, O., 1986. *Fundamentals of Well Log Interpretation 2: The Interpretation of Logging Data:* Amsterdam (Elsevier).
Swart, P. K., and Guzikowski, M., 1988. Interstitial-water chemistry and diagenesis of periplatform sediments from the Bahamas, ODP Leg 101. *In* Austin, J. A., Jr., Schlager, W., et al., *Proc. ODP, Sci. Results,* 101: College Station, TX (Ocean Drilling Program), 363–380.
Symonds, P. A., and Davies, P. J., 1988. Structure, stratigraphy, evolution and regional framework of the Townsville Trough and Marion Plateau region–research cruise proposal, project 9131.11. *Bur. Miner. Res. Aust. Record,* 1988/48.
Symonds, P. A., Davies, P. J., and Parisi, A., 1983. Structure and stratigraphy of the central Great Barrier Reef. *BMR J. Aust. Geol. Geophys.*, 8:277–291.
van Morkhoven, F.P.C.M., Berggren, W .A., Edwards. A. S., et al., 1986. Cenozoic cosmopolitan deep-water benthic foraminifera. *Bull. Cent. Rech. Explor.-Prod. Elf-Aquitaine,* Mem. 11.

Ms 133A-114

NOTE: All core description forms ("barrel sheets") and core photographs have been printed on coated paper and bound separately as Part 2 of this volume, beginning on page 813.

Formation microscanner images for this site are presented on microfiche in the back of Part 2.

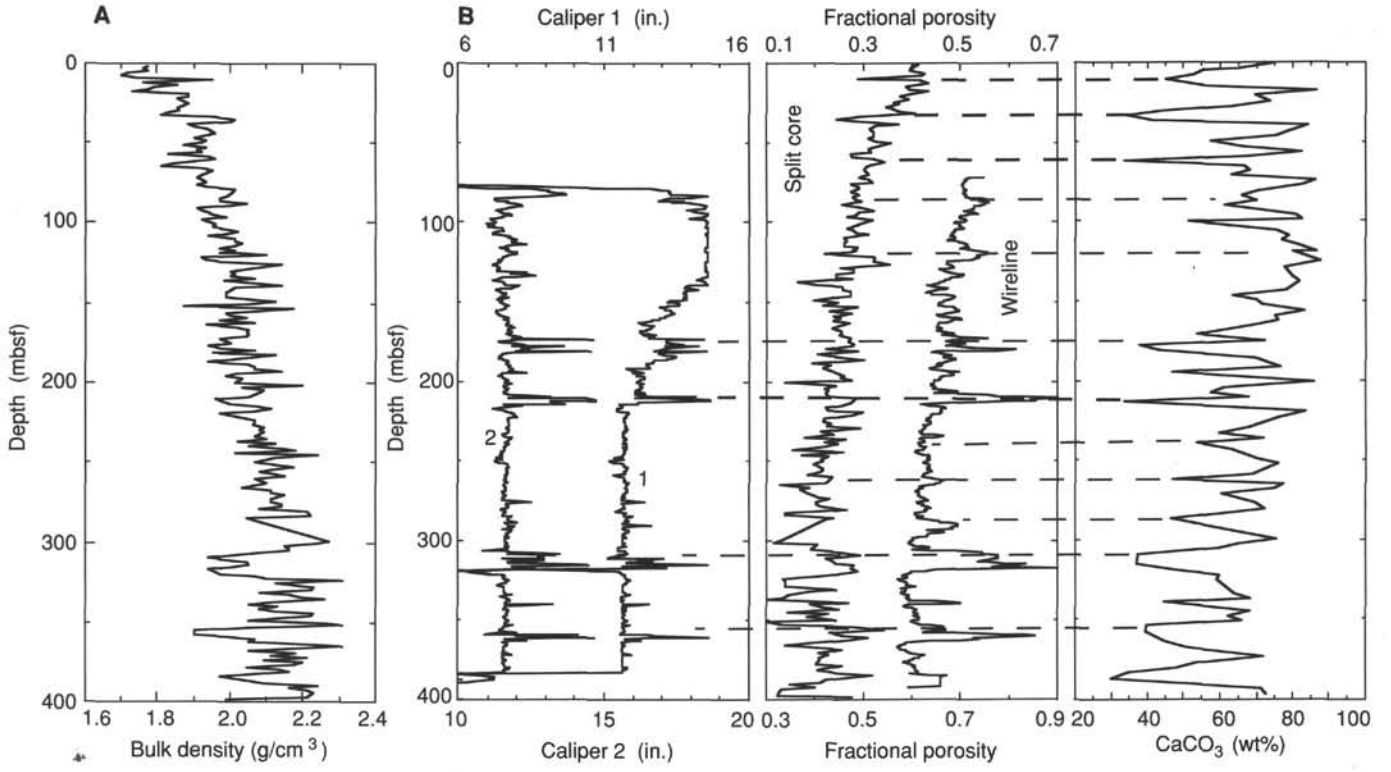

Figure 23. **A.** Bulk density vs. depth at Site 821. The data were obtained from mass and volume measurements of samples taken from split cores. **B.** Porosity, wireline caliper measurements, and weight percent of carbonate at Site 821. Carbonate contents are derived from measurements of samples from split cores as is one of the porosity curves. For the most part, the samples for carbonate analysis were a subsample of the samples used for determining porosity. The wireline porosity curve and the caliper curves were obtained by wireline logging. The dashed lines indicate correlations among the various curves. There is a pattern, by no means perfect, for lows in carbonate to correlate with highs in porosity.

Table 7. Index property data, Site 821.

Core, section, interval (cm)	Depth (mbsf)	Bulk density (g/cm^3)	Grain density (g/cm^3)	Porosity (%)	Water content (%)	Void ratio
133-821A-						
1H-1, 95–98	0.95	1.77	2.77	61.2	54.7	1.58
1H-2, 95–98	2.45	1.76	2.77	60.5	54.4	1.53
1H-3, 75–78	3.75	1.77	2.75	59.8	53.0	1.49
2H-1, 95–98	5.35	1.72	2.78	59.5	55.0	1.47
2H-2, 95–98	6.85	1.70	2.72	62.5	60.6	1.67
2H-3, 95–98	8.35	1.74	2.77	61.8	57.3	1.62
2H-4, 95–98	9.85	1.95	2.69	48.8	34.4	0.95
2H-5, 95–98	11.35	1.76	2.67	61.6	55.7	1.60
3H-1, 95–98	14.85	1.79	2.74	58.7	50.4	1.42
3H-2, 95–98	16.35	1.77	2.74	59.5	52.4	1.47
3H-3, 95–98	17.85	1.73	2.75	63.4	60.2	1.73
3H-4, 95–98	19.35	1.88	2.73	59.4	47.8	1.46
3H-5, 95–98	20.85	1.88	2.77	57.4	45.7	1.35
3H-6, 95–98	22.35	1.85	2.74	59.2	48.9	1.45
4H-1, 95–98	24.35	1.88	2.78	56.3	44.3	1.29
4H-2, 95–98	25.85	1.87	2.80	57.1	45.5	1.33
4H-3, 95–98	27.35	1.85	2.77	54.7	43.3	1.21
4H-4, 95–98	28.85	1.86	2.66	55.8	44.5	1.26
4H-5, 95–98	30.35	1.83	2.81	57.1	47.0	1.33
4H-6, 95–98	31.85	1.81	2.79	60.6	52.2	1.54
5H-1, 95–98	33.85	1.95	2.71	49.0	34.7	0.96
5H-2, 95–98	35.35	2.01	2.73	44.5	29.4	0.80
5H-3, 95–98	36.85	2.00	2.75	48.6	33.1	0.95
5H-4, 95–98	38.35	1.88	2.81	57.2	45.4	1.34
5H-5, 95–98	39.85	1.90	2.78	52.5	39.3	1.11
5H-6, 95–98	41.35	1.94	2.83	51.3	37.2	1.06
6H-1, 95–98	43.35	1.96	2.80	52.2	37.7	1.09
6H-2, 95–98	44.85	1.93	2.56	52.2	38.2	1.09
6H-3, 95–98	46.35	1.90	3.56	52.1	39.0	1.09
6H-4, 95–98	47.85	1.93	2.78	51.1	37.3	1.05
6H-5, 95–98	49.35	1.92	2.87	52.7	39.2	1.12
6H-6, 95–98	50.85	1.87	2.79	55.6	43.9	1.26
7H-1, 95–98	52.85	1.93	2.78	51.6	37.6	1.07
7H-2, 95–98	54.35	1.91	2.82	51.2	37.8	1.05
7H-3, 95–98	55.85	1.92	2.63	51.6	38.0	1.06
7H-4, 95–98	57.35	1.83	2.75	47.3	36.0	0.90
7H-5, 95–98	58.85	1.94	2.80	47.5	33.6	0.90
7H-6, 95–98	60.35	1.96	2.82	52.2	37.6	1.09
8H-1, 95–98	62.35	1.84	2.72	54.5	43.4	1.20
8H-2, 95–98	63.85	1.81	2.69	51.3	40.9	1.05
8H-3, 95–98	65.35	1.92	2.78	50.6	36.9	1.03
8H-4, 95–98	66.85	1.95	2.75	50.1	35.7	1.00
8H-5, 95–98	68.35	1.94	2.58	50.4	36.4	1.02
8H-6, 95–98	69.85	1.92	2.65	51.2	37.8	1.05
9H-1, 95–98	71.85	1.91	2.78	49.0	35.6	0.96
9H-2, 95–98	73.35	1.92	2.74	51.2	37.5	1.05
9H-3, 95–98	74.85	1.93	2.72	51.9	38.1	1.08
9H-4, 95–98	76.35	1.91	2.73	47.2	34.0	0.89
9H-5, 95–98	77.85	1.93	2.73	49.0	35.0	0.96
9H-6, 95–98	79.35	2.01	2.59	49.1	33.5	0.97
10H-1, 95–98	81.35	2.00	2.74	47.3	32.0	0.90
10H-2, 95–98	82.85	1.99	2.77	49.0	33.9	0.96
10H-3, 95–98	84.35	1.97	2.74	47.9	33.2	0.92
10H-4, 95–98	85.85	1.97	2.85	48.3	33.6	0.94
10H-5, 95–98	87.35	2.04	2.85	49.7	33.2	0.99
10H-6, 95–98	88.85	2.00	2.75	45.5	30.5	0.84
11H-1, 95–98	90.85	1.91	2.75	49.6	36.3	0.98
11H-2, 95–98	92.35	1.92	2.77	52.2	38.7	1.09
11H-3, 95–98	93.85	1.94	2.70	49.0	34.8	0.96
11H-4, 95–98	95.35	1.95	2.89	48.4	34.1	0.94
11H-5, 95–98	96.85	1.99	2.73	46.6	31.6	0.87
11H-6, 95–98	98.35	1.92	2.72	51.8	38.2	1.08
12H-1, 95–98	100.35	1.96	2.64	49.6	34.9	0.98
12H-2, 95–98	101.85	1.95	2.59	48.5	34.3	0.94
12H-3, 95–98	103.35	1.99	2.79	46.4	31.2	0.86
12H-4, 95–98	104.85	2.02	2.73	47.6	31.9	0.91
12H-5, 95–98	106.35	1.99	2.80	48.6	33.2	0.94
12H-6, 95–98	107.85	1.94	2.77	50.9	36.7	1.04
13H-1, 95–98	109.85	2.01	2.78	46.1	30.7	0.86
13H-2, 95–98	111.35	2.01	2.70	46.4	31.0	0.86
13H-3, 95–98	112.85	2.03	2.83	46.1	30.4	0.86
13H-4, 95–98	114.35	2.01	2.73	46.1	30.7	0.86
13H-5, 95–98	115.85	1.97	2.65	48.9	34.0	0.96
13H-6, 95–98	117.35	2.01	2.82	47.9	32.2	0.92
13H-7, 10–12	118.00	1.97	2.82	48.6	33.9	0.95

Table 7 (continued).

Core, section, interval (cm)	Depth (mbsf)	Bulk density (g/cm^3)	Grain density (g/cm^3)	Porosity (%)	Water content (%)	Void ratio
14H-1, 5–7	118.45	2.02	2.77	47.2	31.5	0.89
14H-2, 5–7	119.95	2.10	2.75	42.0	25.8	0.72
14H-3, 5–7	121.45	1.92	2.77	52.0	38.4	1.08
14H-4, 5–7	122.95	1.93	2.81	52.4	38.7	1.10
14H-5, 15–17	124.55	1.97	2.74	52.2	37.3	1.09
14H-6, 10–13	126.00	2.14	2.81	55.5	36.2	1.25
15H-1, 10–13	128.00	2.05	2.77	45.3	29.2	0.83
15H-2, 10–13	129.50	2.00	2.78	48.0	32.7	0.92
15H-3, 10–13	131.00	2.01	2.76	48.1	32.5	0.93
15H-4, 10–13	132.50	2.00	2.77	44.2	29.3	0.79
15H-5, 10–13	134.00	2.07	2.77	44.3	28.1	0.80
15H-6, 2–4	135.42	1.98	2.72	47.8	32.7	0.92
16H-1, 8–11	137.48	2.58	2.69	36.4	16.9	0.57
16H-2, 8–11	138.98	2.14	2.73	40.3	23.9	0.67
16H-3, 8–11	140.48	2.01	2.73	45.5	30.1	0.83
16H-4, 8–11	141.98	2.00	2.75	45.7	30.5	0.84
16H-5, 8–11	143.48	1.99	2.75	47.4	32.2	0.90
17X-1, 8–11	145.98	1.99	2.78	47.2	32.0	0.89
17X-2, 8–11	147.48	2.04	2.75	44.6	28.9	0.80
17X-3, 8–11	148.98	2.12	2.77	39.6	23.7	0.66
17X-4, 8–11	150.48	2.04	2.71	44.8	29.0	0.81
17X-5, 8–11	151.98	1.87	2.71	41.6	29.4	0.71
17X-6, 8–11	153.48	2.17	2.78	48.9	30.0	0.96
18X-1, 3–5	155.63	1.99	2.74	43.0	28.4	0.75
18X-2, 9–11	157.19	2.00	2.72	47.6	32.3	0.91
18X-3, 11–13	158.71	2.04	2.71	43.8	28.1	0.78
18X-4, 11–13	160.21	1.97	2.77	45.3	30.8	0.83
18X-5, 22–24	161.82	2.07	2.71	43.8	27.7	0.78
18X-6, 10–12	163.20	1.93	2.69	47.1	33.3	0.89
19X-1, 3–5	165.23	2.01	2.71	44.7	29.5	0.81
19X-2, 3–5	166.73	2.05	2.75	43.4	27.7	0.77
19X-3, 3–5	168.23	2.04	2.73	45.3	29.3	0.83
19X-4, 6–9	169.76	2.05	2.77	45.4	29.3	0.83
19X-5, 6–9	171.26	2.04	2.75	45.0	29.1	0.82
19X-6, 6–9	172.76	1.97	2.77	47.4	32.6	0.90
20X-1, 12–13	175.02	2.00	2.76	46.9	31.6	0.88
20X-2, 7–10	176.47	1.94	2.72	48.1	34.0	0.93
20X-3, 7–10	177.97	1.97	2.76	47.5	32.8	0.91
20X-4, 7–10	179.47	2.07	2.75	42.3	26.5	0.73
20X-5, 7–10	180.97	1.95	2.76	48.7	34.3	0.95
20X-6, 7–10	182.47	2.12	2.75	40.4	24.3	0.68
21X-1, 90–92	185.50	1.99	2.77	47.4	32.4	0.90
21X-2, 90–92	187.00	1.94	2.76	50.0	35.8	1.00
21X-3, 90–92	188.50	2.05	2.73	39.5	24.6	0.65
21X-4, 90–92	190.00	2.07	2.74	43.3	27.3	0.76
21X-5, 90–92	191.50	2.07	2.73	41.6	26.0	0.71
21X-6, 90–92	193.00	2.14	2.81	42.5	25.5	0.74
22X-1, 90–92	194.80	2.02	2.77	44.5	29.1	0.80
22X-2, 90–92	196.30	1.99	2.72	45.9	30.9	0.85
22X-3, 90–92	197.80	2.03	2.75	45.3	29.7	0.83
22X-4, 90–92	199.30	2.01	2.80	47.5	31.9	0.91
22X-5, 90–92	200.80	2.20	2.76	33.9	18.7	0.51
22X-6, 90–92	202.30	2.03	2.72	44.2	28.8	0.79
23X-1, 90–92	204.40	2.09	2.76	42.0	26.0	0.72
23X-2, 90–92	205.90	2.08	2.74	42.7	26.7	0.75
23X-3, 90–92	207.40	2.07	2.73	42.1	26.3	0.73
23X-4, 90–92	208.90	2.05	2.73	42.6	27.1	0.74
23X-5, 90–92	210.40	1.96	2.79	48.5	33.9	0.94
24X-1, 90–92	213.70	2.00	2.75	47.3	31.9	0.90
24X-2, 90–92	215.20	2.07	2.74	45.1	28.8	0.82
24X-3, 90–92	216.70	2.11	2.83	42.3	25.8	0.73
24X-4, 90–92	218.20	2.07	2.76	42.6	26.7	0.74
24X-5, 90–92	219.70	1.97	2.73	49.8	34.9	0.99
24X-6, 90–92	221.20	2.03	2.73	47.6	31.7	0.91
25X-1, 90–92	223.40	2.07	2.69	42.0	26.2	0.72
25X-2, 90–92	224.90	2.07	2.74	41.8	26.1	0.72
25X-3, 90–92	226.40	2.06	2.73	43.2	27.4	0.76
25X-4, 90–92	227.90	2.09	2.73	42.4	26.2	0.74
25X-5, 90–92	229.40	2.08	2.64	49.4	32.2	0.98
25X-6, 90–92	230.90	2.09	2.73	41.2	25.3	0.70
26X-1, 90–92	233.10	2.07	2.74	43.8	27.7	0.78
26X-2, 90–92	234.60	2.10	2.72	38.0	22.7	0.61
26X-3, 90–92	236.10	2.02	2.77	46.3	30.7	0.86
26X-4, 90–92	237.60	2.12	2.76	42.0	25.5	0.72
26X-5, 90–92	239.10	2.05	2.75	44.7	28.8	0.81
26X-6, 90–92	240.6	2.14	2.73	41.9	25.0	0.72
27X-1, 90–92	242.70	2.18	2.74	35.4	20.0	0.55

Table 7 (continued).

Core, section, interval (cm)	Depth (mbsf)	Bulk density (g/cm^3)	Grain density (g/cm^3)	Porosity (%)	Water content (%)	Void ratio
27X-2, 90–92	244.20	2.01	2.78	45.8	30.5	0.85
27X-3, 90–92	245.70	2.24	2.71	37.0	20.3	0.59
27X-4, 90–92	247.20	2.12	2.74	42.7	25.9	0.74
27X-5, 90–92	248.70	2.09	2.76	41.1	25.2	0.70
27X-6, 90–92	250.20	2.07	2.74	41.7	26.0	0.72
28X-1, 90–92	252.30	2.17	2.73	39.7	23.0	0.66
28X-2, 90–92	253.80	2.12	2.70	40.9	24.7	0.69
28X-3, 90–92	255.30	2.08	2.66	41.8	25.9	0.72
28X-4, 90–92	256.80	2.12	2.75	41.3	25.0	0.70
28X-5, 90–92	258.30	2.15	2.74	38.4	22.4	0.62
28X-6, 90–92	259.80	2.07	2.71	43.6	27.5	0.77
29X-2, 90–92	263.50	2.10	2.67	42.1	25.9	0.73
29X-3, 90–92	265.00	2.03	2.90	32.8	19.8	0.49
29X-4, 90–92	266.50	2.11	2.81	38.9	23.3	0.64
29X-5, 90–92	268.00	2.11	2.79	36.8	21.8	0.58
29X-6, 90–92	269.50	2.15	2.80	38.1	22.2	0.62
30X-2, 11–13	272.41	2.11	2.72	40.7	24.6	0.69
30X-3, 4–5	273.84	2.11	2.74	43.0	26.5	0.75
30X-4, 5–7	275.35	2.14	2.72	40.1	23.7	0.67
30X-5, 5–7	276.85	2.14	2.75	40.2	23.8	0.67
30X-6, 5–7	278.35	2.08	2.66	41.3	25.5	0.70
31X-1, 2–4	280.42	2.21	2.74	46.6	27.6	0.87
31X-2, 9–11	281.99	1.69	2.71	33.8	25.8	0.51
31X-3, 11–13	283.51	2.22	2.71	33.7	18.4	0.51
31X-4, 11–13	285.01	2.04	2.66	43.7	28.1	0.78
31X-5, 9–11	286.49	2.07	2.73	42.3	26.5	0.73
33X-1, 3–5	299.73	2.27	2.69	3.33	17.7	0.50
33X-2, 3–5	301.08	2.24	2.71	31.6	16.9	0.46
33X-3, 3–5	302.58	2.15	2.74	40.3	23.8	0.68
33X-4, 5–7	304.10	2.16	2.74	39.6	23.2	0.66
33X-5, 4–6	305.59	2.16	2.72	39.2	22.9	0.64
33X-6, 4–6	307.09	2.07	2.75	44.6	28.3	0.81
34X-1, 4–6	309.44	1.94	2.71	49.4	35.2	0.98
34X-2, 4–6	310.94	1.99	2.75	42.2	27.7	0.73
34X-3, 4–6	312.44	2.04	2.74	43.3	27.7	0.76
34X-4, 4–6	313.94	2.05	2.73	44.3	28.4	0.80
34X-5, 4–6	315.44	2.00	2.73	48.1	32.6	0.93
34X-6, 4–6	316.94	1.94	2.79	47.2	33.1	0.89
35X-1, 5–7	319.05	1.97	2.70	48.9	34.2	0.96
35X-2, 5–7	320.55	2.07	2.73	44.1	27.8	0.79
35X-3, 5–7	322.05	2.10	2.71	42.3	25.9	0.73
35X-4, 5–7	323.55	2.31	2.56	33.3	17.3	0.50
35X-5, 5–7	325.05	2.12	2.71	33.8	19.5	0.51
36X-1, 6–8	328.76	2.23	2.70	33.7	18.3	0.51

Table 7 (continued).

Core, section, interval (cm)	Depth (mbsf)	Bulk density (g/cm^3)	Grain density (g/cm^3)	Porosity (%)	Water content (%)	Void ratio
36X-2, 6–8	329.32	2.22	2.71	34.1	18.7	0.52
36X-3, 6–8	330.82	2.08	2.74	44.2	27.9	0.79
36X-4, 6–8	332.32	2.16	2.70	38.7	22.5	0.63
36X-5, 6–8	333.82	2.19	2.73	34.6	19.3	0.53
36X-6, 6–8	335.32	2.26	2.72	33.4	17.9	0.50
36X-7, 6–8	336.82	2.12	2.76	29.6	16.7	0.42
37X-1, 5–7	338.35	2.05	2.91	46.8	30.6	0.88
37X-2, 5–7	339.85	2.13	2.74	38.8	22.9	0.63
37X-3, 5–7	341.35	2.08	2.77	41.7	25.9	0.72
37X-4, 5–7	342.85	2.12	2.77	45.0	27.8	0.82
37X-5, 5–7	344.35	2.23	2.72	34.3	18.7	0.52
37X-6, 5–7	345.85	2.22	2.71	42.8	24.6	0.75
38X-1, 5–6	347.95	2.14	2.56	38.5	22.6	0.63
38X-2, 5–6	349.45	2.05	2.75	44.3	28.5	0.79
38X-3, 2–3	350.92	2.25	2.57	29.7	15.6	0.42
38X-4, 2–3	352.42	2.31	2.70	33.2	17.3	0.50
38X-5, 5–6	353.95	2.05	2.69	47.4	31.1	0.90
38X-6, 5–6	355.45	1.90	2.75	54.2	41.2	1.18
39X-1, 5–7	357.55	1.90	2.89	43.0	30.2	0.75
39X-2, 5–7	359.05	1.99	2.75	45.8	30.9	0.85
39X-3, 5–7	360.55	2.07	2.70	50.9	33.6	1.04
39X-4, 5–7	362.05	2.05	2.74	45.5	29.5	0.84
39X-5, 5–7	363.55	2.17	2.79	41.0	23.9	0.69
39X-6, 5–7	365.05	2.31	2.74	33.8	17.6	0.51
40X-1, 10–11	367.30	2.05	2.73	42.8	27.1	0.75
40X-2, 10–11	368.80	2.18	2.79	45.4	27.1	0.83
40X-3, 10–11	370.30	2.11	2.56	40.8	24.7	0.69
40X-4, 10–11	371.80	2.21	2.69	42.6	24.6	0.74
40X-5, 10–11	373.30	2.09	2.71	40.6	24.7	0.68
40X-6, 10–11	374.80	2.20	3.01	41.0	23.6	0.69
41X-1, 10–11	376.90	2.17	2.69	40.1	23.4	0.67
41X-2, 10–11	378.40	2.04	2.71	45.4	29.6	0.83
41X-3, 10–11	379.90	2.13	2.73	41.5	24.9	0.71
41X-4, 10–11	381.40	2.16	2.87	40.4	23.7	0.68
41X-5, 10–11	382.90	2.04	2.92	45.1	29.3	0.82
41X-6, 10–11	384.40	1.97	2.68	51.9	37.0	1.08
42X-1, 90–92	387.30	2.05	2.77	42.1	26.6	0.73
42X-2, 90–92	388.80	2.09	2.78	40.9	25.1	0.69
42X-3, 90–92	390.30	2.24	2.76	34.9	19.0	0.54
42X-4, 90–92	391.80	2.16	2.75	39.8	23.2	0.66
42X-5, 90–92	393.30	2.21	2.75	33.0	18.0	0.49
42X-6, 90–92	394.80	2.23	2.79	32.5	17.6	0.48
43X-1, 89–91	396.99	2.21	2.62	32.4	17.7	0.48
43X-2, 90–92	398.50	1.99	2.65	47.6	32.6	0.91

Table 8. Compressional-wave velocity data, Site 821.

Core, section, interval (cm)	Depth (mbsf)	Distance (mm)	Traveltime (μs)	Velocity (m/s)
133-821A-				
1H-1, 95–98	0.95	28.96	20.98	1562
1H-2, 95–98	2.45	29.57	21.52	1549
1H-3, 75–78	3.75	27.93	20.39	1555
2H-1, 95–98	5.35	29.80	21.73	1544
2H-2, 95–98	6.85	29.82	21.81	1538
2H-3, 95–98	8.35	29.55	21.48	1552
2H-4, 95–98	9.85	28.93	19.38	1716
2H-5, 95–98	11.35	29.28	21.37	1546
2H-6, 95–98	12.85	29.51	21.38	1558
3H-1, 95–98	14.85	27.62	20.10	1564
3H-2, 95–98	16.35	29.11	20.54	1611
3H-3, 95–98	17.85	28.83	20.15	1632
3H-4, 95–98	19.35	26.33	19.07	1583
3H-5, 95–98	20.85	29.29	20.96	1583
3H-6, 95–98	22.35	29.55	21.21	1575
4H-1, 95–98	24.35	29.68	21.27	1577
4H-2, 95–98	25.85	29.50	20.96	1595
4H-3, 95–98	27.35	29.91	21.41	1578
4H-4, 95–98	28.85	29.42	21.11	1577
4H-5, 95–98	30.35	29.20	21.28	1549
4H-6, 95–98	31.85	27.58	20.18	1554
5H-1, 95–98	33.85	27.93	21.39	1469
5H-3, 95–98	36.85	28.96	22.46	1440
5H-4, 95–98	38.35	29.51	22.72	1449
5H-5, 95–98	39.85	28.96	20.23	1632
5H-6, 95–98	41.35	28.50	19.97	1629
6H-1, 95–98	43.35	29.29	20.59	1617
6H-2, 95–98	44.85	29.51	20.77	1613
6H-3, 95–98	46.35	27.99	19.70	1625
6H-4, 95–98	47.85	29.34	20.50	1628
6H-5, 95–98	49.35	29.55	20.68	1624
6H-6, 95–98	50.85	29.01	20.75	1586
7H-1, 95–98	52.85	29.33	20.52	1626
7H-2, 95–98	54.35	29.89	20.87	1626
7H-3, 95–98	55.85	27.61	20.80	1500
7H-4, 95–98	57.35	28.23	19.71	1638
7H-5, 95–98	58.85	29.81	20.52	1654
7H-6, 95–98	60.35	29.02	20.16	1642
8H-1, 100–103	62.40	29.65	21.07	1593
8H-2, 95–98	63.85	29.93	21.40	1580
8H-3, 95–98	65.35	29.78	20.34	1670
8H-4, 95–98	66.85	30.38	21.06	1636
8H-5, 95–98	68.35	31.25	21.70	1627
8H-6, 95–98	69.85	29.99	20.83	1635
9H-1, 15–19	71.05	30.55	20.98	1653
9H-2, 15–19	72.55	30.42	21.17	1628
9H-3, 15–19	74.05	31.55	21.72	1641
9H-4, 15–19	75.55	30.55	21.45	1610
9H-5, 15–19	77.05	28.15	19.50	1655
9H-6, 15–19	78.55	28.64	19.98	1637
10H-1, 22–25	80.62	30.31	20.86	1651
10H-2, 22–25	82.12	30.36	20.83	1656
10H-3, 22–25	83.62	29.50	20.42	1645
10H-4, 22–25	85.12	30.07	20.54	1667
10H-5, 22–25	86.62	30.41	21.08	1636
11H-1, 20–23	90.10	28.58	21.83	1469
11H-2, 20–23	91.60	28.86	22.08	1464
11H-3, 20–23	93.10	29.85	20.51	1657
11H-4, 20–23	94.60	29.42	20.21	1661
11H-5, 20–23	96.10	29.51	21.82	1521
11H-6, 20–23	97.60	29.72	21.70	1542
11H-7, 20–23	99.10	30.03	20.55	1664
12H-1, 15–18	99.55	29.42	20.99	1587
12H-2, 15–18	101.05	30.68	21.18	1642
12H-3, 15–18	102.55	29.72	20.39	1661
12H-4, 15–18	104.05	29.68	20.55	1643
12H-5, 15–18	105.55	29.79	20.07	1697
12H-6, 15–18	107.05	29.37	20.49	1631
13H-1, 15–18	109.05	29.99	19.85	1732
13H-2, 15–18	110.55	29.81	22.76	1462
13H-3, 15–18	112.05	29.51	20.19	1668
13H-4, 15–18	113.55	29.55	20.35	1655
13H-5, 15–18	115.05	30.16	20.83	1645
15H-1, 10–13	128.00	32.06	22.43	1607
15H-2, 10–13	129.50	30.94	21.29	1647
15H-3, 10–13	131.00	29.99	20.37	1679
15H-4, 10–13	132.50	30.23	20.53	1678
15H-5, 10–13	134.00	30.07	19.84	1738

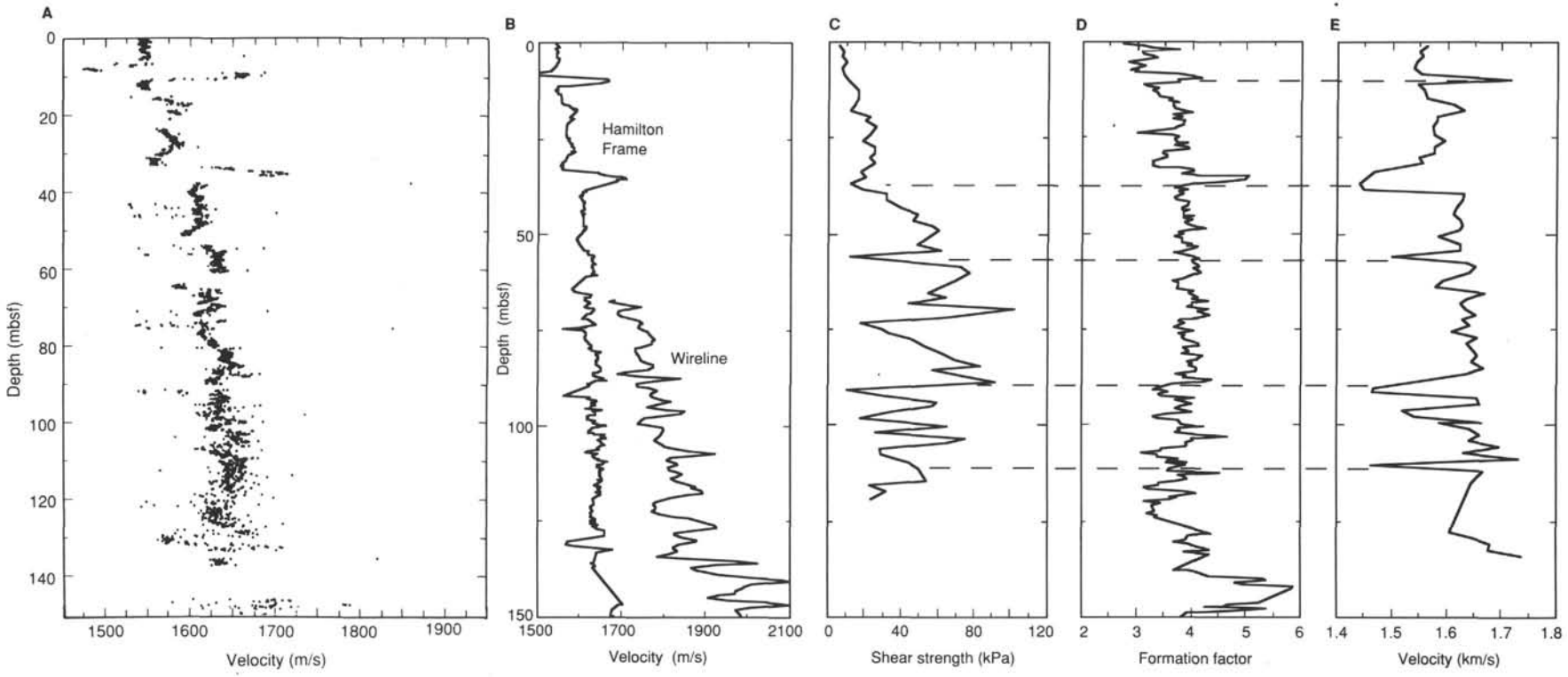

Figure 24. **A.** MST sonic velocity data Hole 821A. Raw data values with amplitudes greater than 30 have been averaged in 5-cm intervals. **B.** Velocity vs. depth for the upper 150 mbsf of section at Site 821 determined from Hamilton Frame measurements of samples from split cores and from wireline logging. **C.** Shear strength vs. depth. **D.** FF vs. depth. **E.** Velocity vs. depth. All these data were obtained from split cores. There is a general, though not perfect, correlation of velocity lows with shear strength lows and FF highs that should be consistent with expected relationships between water content and the measured physical properties.

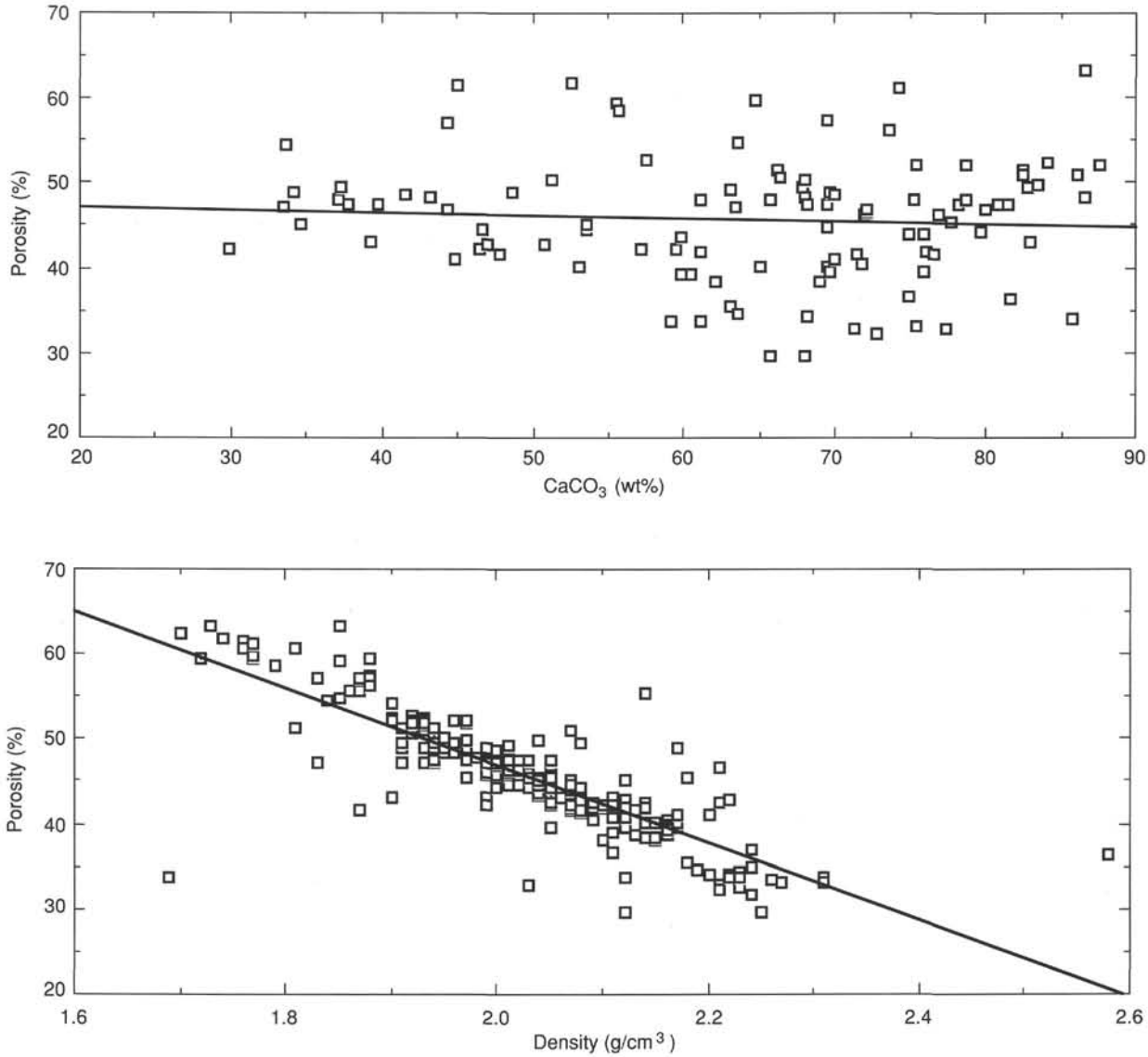

Figure 25. Porosity vs. wt% carbonate and porosity vs. bulk density at Site 821. This plot suggests essentially no correlation between wt% carbonate and porosity. The linear regression curve is of the form, $P = 47.7 - 0.0310\ CaCO_3$, where P = porosity, $CaCO_3$ = wt% carbonate, and the regression coefficient $R = 0.06$. There is the expected strong linear inverse correlation between porosity and bulk density. The regression curve is of the form $P = 137–45D$, where P = porosity, D = bulk density, and the regression coefficient $R = 0.83$. This is a useful check on the internal consistency of our measurements of density and porosity.

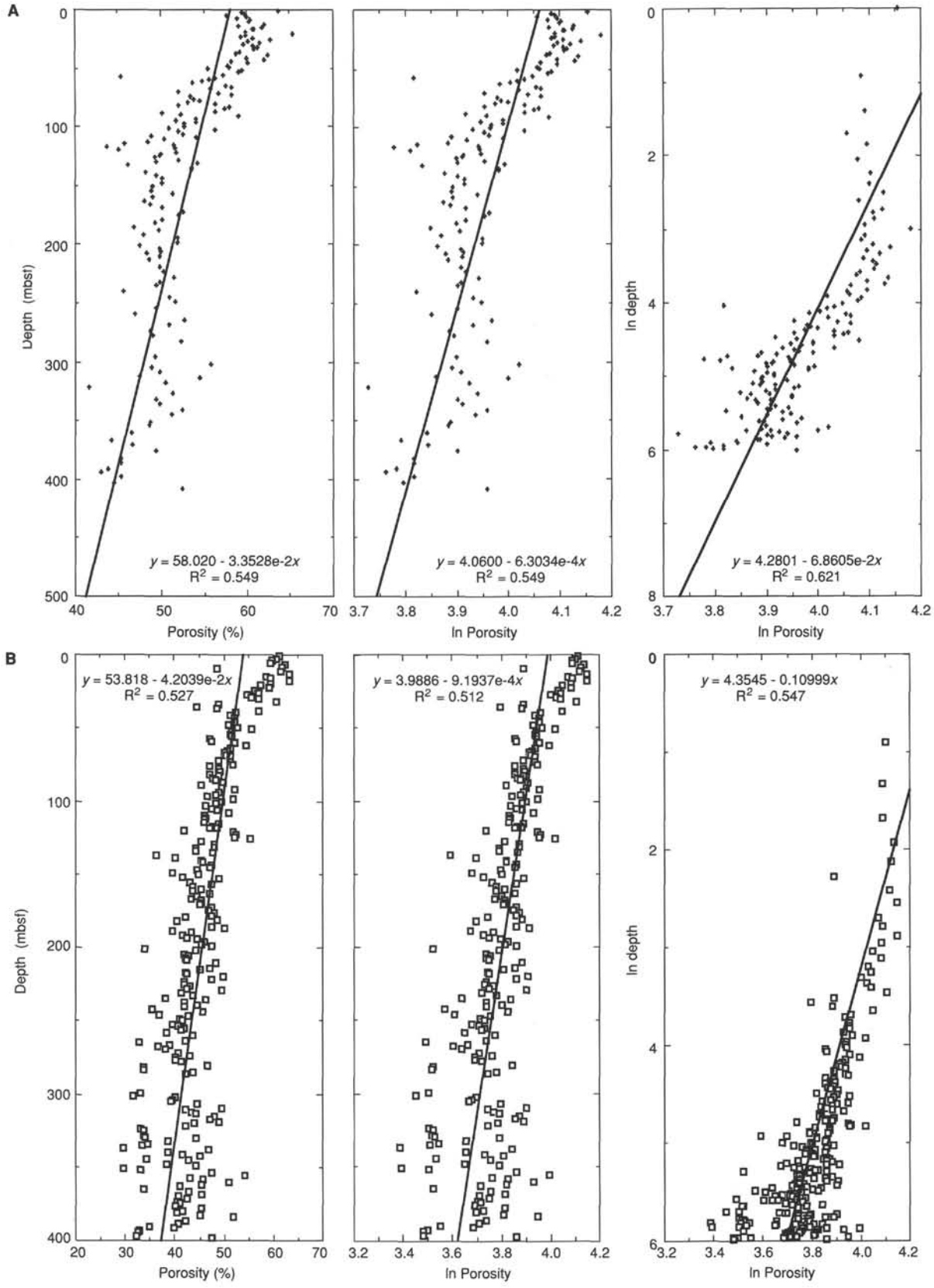

Figure 26. **A.** Porosity-depth, ln porosity-depth, and ln porosity-ln depth plots of data from Site 815. Linear regressions are shown for each plot along with R^2 where R is the regression coefficient. For Site 815 a linear regression of ln porosity on ln depth describes the actual data marginally better than the other regressions. **B.** Porosity-depth, ln porosity-depth, and ln porosity-ln depth plots of data from Site 821. Linear regressions are shown for each plot along with R^2 where R is the regression coefficient. For Site 821, a linear regression of ln porosity on ln depth describes the actual data marginally better than the other regressions.

Table 9. Formation factor data, Hole 821A.

Core, section, interval (cm)	Depth (mbsf)	Seawater (ohms)	Sample (ohms)	Formation factor
133-821A-				
1H-1, 40–40	0.40	2.6	7.1	2.73
1H-1, 80–80	0.80	2.6	7.9	3.04
1H-1, 130–130	1.30	2.6	8.0	3.08
1H-2, 20–20	1.70	2.6	8.5	3.27
1H-2, 70–70	2.20	2.6	9.8	3.77
1H-2, 120–120	2.70	2.6	8.0	3.08
1H-3, 20–20	3.20	2.6	8.1	3.12
1H-3, 70–70	3.70	2.6	8.5	3.27
1H-3, 110–110	4.10	2.6	8.7	3.35
2H-1, 20–20	4.60	2.6	8.2	3.15
2H-1, 70–70	5.10	2.6	7.4	2.85
2H-1, 130–130	5.70	2.6	7.8	3.00
2H-2, 20–20	6.10	2.6	8.2	3.15
2H-2, 70–70	6.60	2.6	8.2	3.15
2H-2, 130–130	7.20	2.6	7.5	2.88
2H-3, 20–20	7.60	2.6	7.8	3.00
2H-3, 70–70	8.10	2.6	7.7	2.96
2H-3, 130–130	8.70	2.6	9.7	3.73
2H-4, 20–20	9.10	2.6	10.4	4.00
2H-4, 70–70	9.60	2.6	10.9	4.19
2H-4, 130–130	10.20	2.6	9.7	3.73
2H-5, 20–20	10.60	2.6	9.8	3.77
2H-5, 70–70	11.10	2.6	8.1	3.12
2H-5, 130–130	11.70	2.6	8.3	3.19
2H-6, 20–20	12.10	2.6	8.8	3.38
2H-6, 70–70	12.60	2.6	8.5	3.27
2H-6, 130–130	13.20	2.6	8.7	3.35
3H-1, 20–20	14.10	2.6	8.9	3.42
3H-1, 70–70	14.60	2.6	9.4	3.62
3H-1, 130–130	15.20	2.6	9.3	3.58
3H-2, 20–20	15.60	2.6	9.8	3.77
3H-2, 70–70	16.10	2.6	9.5	3.65
3H-2, 130–130	16.70	2.6	9.5	3.65
3H-3, 20–20	17.10	2.6	9.6	3.69
3H-3, 70–70	17.60	2.6	9.6	3.69
3H-3, 130–130	18.20	2.6	10.0	3.85
3H-4, 20–20	18.60	2.6	10.4	4.00
3H-4, 70–70	19.10	2.6	9.5	3.65
3H-4, 130–130	19.70	2.6	9.9	3.81
3H-5, 20–20	20.10	2.6	9.5	3.65
3H-5, 70–70	20.60	2.6	10.1	3.88
3H-5, 110–110	21.00	2.6	10.0	3.85
3H-6, 20–20	21.60	2.6	10.0	3.85
3H-6, 70–70	22.10	2.6	9.7	3.73
3H-6, 130–130	22.70	2.6	9.6	3.69
4H-1, 20–20	23.60	2.6	7.8	3.00
4H-1, 70–70	24.10	2.6	9.4	3.62
4H-1, 130–130	24.70	2.6	9.8	3.77
4H-2, 20–20	25.10	2.6	9.6	3.69
4H-2, 70–70	25.60	2.6	9.6	3.69
4H-2, 130–130	26.20	2.6	9.7	3.73
4H-3, 20–20	26.60	2.6	10.2	3.92
4H-3, 70–70	27.10	2.6	9.6	3.69
4H-3, 130–130	27.70	2.6	10.2	3.92
4H-4, 20–20	28.10	2.6	10.3	3.96
4H-4, 70–70	28.60	2.6	9.1	3.50
4H-4, 130–130	29.20	2.6	9.0	3.46
4H-5, 20–20	29.60	2.6	9.2	3.54
4H-5, 70–70	30.10	2.6	9.2	3.54
4H-5, 130–130	30.70	2.6	8.9	3.42
4H-6, 20–20	31.10	2.6	8.5	3.27
4H-6, 70–70	31.60	2.6	8.6	3.31
4H-6, 130–130	32.20	2.6	8.5	3.27
4H-7, 20–20	32.60	2.6	8.9	3.42
4H-7, 60–60	33.00	2.6	9.8	3.77
5H-1, 20–20	33.10	2.6	10.4	4.00
5H-1, 70–70	33.60	2.6	10.5	4.04
5H-1, 130–130	34.20	2.6	9.9	3.81
5H-2, 20–20	34.60	2.6	10.8	4.15
5H-2, 70–70	35.10	2.6	13.1	5.04
5H-2, 130–130	35.70	2.6	12.9	4.96
5H-3, 20–20	36.10	2.6	12.8	4.92
5H-3, 70–70	36.60	2.6	12.0	4.62
5H-3, 130–130	37.20	2.6	10.6	4.08
5H-4, 20–20	37.60	2.6	10.1	3.88

Table 9 (continued).

Core, section, interval (cm)	Depth (mbsf)	Seawater (ohms)	Sample (ohms)	Formation factor
5H-4, 70–70	38.10	2.6	9.6	3.69
5H-4, 130–130	38.70	2.6	10.2	3.92
5H-5, 20–20	39.10	2.6	9.8	3.77
5H-5, 70–70	39.60	2.6	10.0	3.85
5H-5, 130–130	40.20	2.6	9.8	3.77
5H-6, 20–20	40.60	2.6	9.6	3.69
5H-6, 70–70	41.10	2.6	9.7	3.73
5H-6, 130–130	41.70	2.6	10.3	3.96
6H-1, 20–20	42.60	2.6	10.2	3.92
6H-1, 70–70	43.10	2.6	9.9	3.81
6H-1, 130–130	43.70	2.6	9.90	3.81
6H-2, 20–20	44.10	2.6	10.3	3.96
6H-2, 70–70	44.60	2.6	10.0	3.85
6H-2, 130–130	45.20	2.6	10.0	3.85
6H-3, 20–20	45.60	2.6	10.5	4.04
6H-3, 70–70	46.10	2.6	10.0	3.85
6H-3, 130–130	46.70	2.6	10.4	4.00
6H-4, 20–20	47.10	2.6	10.1	3.88
6H-4, 70–70	47.60	2.6	10.2	3.92
6H-4, 130–130	48.20	2.6	10.4	4.00
6H-5, 20–20	48.60	2.6	11.1	4.27
6H-5, 70–70	49.10	2.6	10.3	3.96
6H-5, 110–110	49.50	2.6	9.8	3.77
6H-6, 20–20	50.10	2.6	10.0	3.85
6H-6, 70–70	50.60	2.6	9.6	3.69
6H-6, 130–130	51.20	2.6	9.9	3.81
7H-1, 20–20	52.10	2.6	9.9	3.81
7H-1, 70–70	52.60	2.6	10.4	4.00
7H-1, 130–130	53.20	2.6	10.2	3.92
7H-2, 20–20	53.60	2.6	10.7	4.12
7H-2, 70–70	54.10	2.6	10.5	4.04
7H-2, 130–130	54.70	2.6	9.8	3.77
7H-3, 20–20	55.10	2.6	9.6	3.69
7H-3, 70–70	55.60	2.6	10.0	3.85
7H-3, 130–130	56.20	2.6	10.5	4.04
7H-4, 20–20	56.60	2.6	10.8	4.15
7H-4, 70–70	57.10	2.6	10.4	4.00
7H-4, 130–130	57.70	2.6	10.5	4.04
7H-5, 20–20	58.10	2.6	10.7	4.12
7H-5, 70–70	58.60	2.6	10.8	4.15
7H-5, 130–130	59.20	2.6	10.5	4.04
7H-6, 20–20	59.60	2.6	10.8	4.15
7H-6, 70–70	60.10	2.6	10.9	4.19
7H-6, 130–130	60.70	2.6	10.5	4.04
8H-1, 20–20	61.60	2.6	10.0	3.85
8H-1, 70–70	62.10	2.6	9.5	3.65
8H-1, 130–130	62.70	2.6	9.8	3.77
8H-2, 20–20	63.10	2.6	9.8	3.77
8H-2, 70–70	63.60	2.6	9.8	3.77
8H-2, 130–130	64.20	2.6	9.7	3.73
8H-3, 20–20	64.60	2.6	9.7	3.73
8H-3, 70–70	65.10	2.6	10.5	4.04
8H-3, 130–130	65.70	2.6	10.3	3.96
8H-4, 20–20	66.10	2.6	10.4	4.00
8H-4, 70–70	66.60	2.6	10.7	4.12
8H-4, 120–120	67.10	2.6	10.4	4.00
8H-5, 20–20	67.60	2.6	11.2	4.31
8H-5, 70–70	68.10	2.6	10.4	4.00
8H-5, 120–120	68.60	2.6	10.4	4.00
8H-6, 20–20	69.10	2.6	10.2	3.92
8H-6, 70–70	69.60	2.6	11.2	4.31
8H-6, 120–120	70.10	2.6	10.7	4.12
9H-1, 20–20	71.10	2.6	11.3	4.35
9H-1, 70–70	71.60	2.6	10.9	4.19
9H-1, 120–120	72.10	2.6	10.4	4.00
9H-2, 20–20	72.60	2.6	9.9	3.81
9H-2, 70–70	73.10	2.6	9.8	3.77
9H-2, 120–120	73.60	2.6	10.1	3.88
9H-3, 20–20	74.10	2.6	9.8	3.77
9H-3, 70–70	74.60	2.6	9.6	3.69
9H-3, 120–120	75.10	2.6	10.0	3.85
9H-4, 20–20	75.60	2.6	10.5	4.04
9H-4, 70–70	76.10	2.6	9.8	3.77
9H-4, 120–120	76.60	2.6	10.1	3.88
9H-5, 20–20	77.10	2.6	9.9	3.81
9H-5, 70–70	77.60	2.6	10.1	3.88
9H-6, 20–20	78.60	2.6	10.7	4.12

Table 9 (continued).

Core, section, interval (cm)	Depth (mbsf)	Seawater (ohms)	Sample (ohms)	Formation factor
9H-6, 70–70	79.10	2.6	10.8	4.15
9H-6, 120–120	79.60	2.6	10.0	3.85
10H-1, 20–20	80.60	2.9	11.5	3.97
10H-1, 70–70	81.10	2.9	11.2	3.86
10H-1, 120–120	81.60	2.9	11.1	3.83
10H-2, 20–20	82.10	2.9	12.2	4.21
10H-2, 70–70	82.60	2.9	12.0	4.14
10H-2, 120–120	83.10	2.9	11.9	4.10
10H-3, 20–20	83.60	2.9	11.4	3.93
10H-3, 70–70	84.10	2.9	11.6	4.00
10H-3, 120–120	84.60	2.9	11.5	3.97
10H-4, 20–20	85.10	2.9	11.9	4.10
10H-4, 70–70	85.60	2.9	11.9	4.10
10H-4, 120–120	86.10	2.9	11.8	4.07
10H-5, 20–20	86.60	2.9	10.8	3.72
10H-5, 70–70	87.10	2.9	11.3	3.90
10H-5, 120–120	87.60	2.9	11.2	3.86
10H-6, 20–20	88.10	2.9	12.7	4.38
10H-6, 70–70	88.60	2.9	12.2	4.21
10H-6, 120–120	89.10	2.9	10.6	3.66
11H-1, 20–20	90.10	2.9	9.8	3.38
11H-1, 70–70	90.60	2.9	9.6	3.31
11H-1, 120–120	91.10	2.9	10.0	3.45
11H-2, 20–20	91.60	2.9	10.4	3.59
11H-2, 70–70	92.10	2.9	9.9	3.41
11H-2, 120–120	92.60	2.9	10.1	3.48
11H-3, 20–20	93.10	2.9	11.8	4.07
11H-3, 70–70	93.60	2.9	10.8	3.72
11H-3, 120–120	94.10	2.9	11.3	3.90
11H-4, 20–20	94.60	2.9	11.6	4.00
11H-4, 70–70	95.10	2.9	11.1	3.83
11H-4, 120–120	95.60	2.9	10.8	3.72
11H-5, 20–20	96.10	2.9	11.2	3.86
11H-5, 70–70	96.60	2.9	11.6	4.00
11H-5, 120–120	97.10	2.9	10.3	3.55
11H-6, 20–20	97.60	2.9	9.6	3.31
11H-6, 70–70	98.10	2.9	9.8	3.38
11H-6, 120–120	98.60	2.9	10.9	3.76
12H-1, 20–20	99.60	2.9	11.1	3.83
12H-1, 70–70	100.10	2.9	11.8	4.07
12H-1, 120–120	100.60	2.9	12.3	4.24
12H-2, 20–20	101.10	2.9	10.9	3.76
12H-2, 70–70	101.60	2.9	11.0	3.79
12H-2, 120–120	102.10	2.9	10.8	3.72
12H-3, 20–20	102.60	2.9	11.7	4.03
12H-3, 70–70	103.10	2.9	13.5	4.66
12H-3, 120–120	103.60	2.9	11.6	4.00
12H-4, 20–20	104.10	2.9	11.7	4.03
12H-4, 70–70	104.60	2.9	11.3	3.90
12H-4, 120–120	105.10	2.9	11.4	3.93
12H-5, 20–20	105.60	2.9	11.3	3.90
12H-5, 70–70	106.10	2.9	10.1	3.48
12H-5, 120–120	106.60	3.1	10.7	3.45
12H-6, 20–20	107.10	3.1	9.6	3.10
12H-6, 70–70	107.60	3.1	10.5	3.39
12H-6, 120–120	108.10	3.1	10.5	3.39
12H-7, 20–20	108.60	2.6	9.8	3.77
13H-1, 20–20	109.10	3.1	11.1	3.58
13H-1, 70–70	109.60	3.1	12.2	3.94
13H-1, 120–120	110.10	3.1	11.0	3.55
13H-2, 20–20	110.60	3.1	12.1	3.90

Table 9 (continued).

Core, section, interval (cm)	Depth (mbsf)	Seawater (ohms)	Sample (ohms)	Formation factor
13H-2, 70–70	111.10	3.1	11.6	3.74
13H-2, 120–120	111.60	3.1	11.2	3.61
13H-3, 20–20	112.10	3.1	11.1	3.58
13H-3, 70–70	112.60	3.1	14.0	4.52
13H-3, 120–120	113.10	3.1	11.7	3.77
13H-4, 20–20	113.60	3.1	12.0	3.87
13H-4, 70–70	114.10	3.1	12.2	3.94
13H-4, 120–120	114.60	3.1	11.6	3.74
13H-5, 20–20	115.10	3.1	10.6	3.42
13H-5, 70–70	115.60	3.1	10.6	3.42
13H-5, 120–120	116.10	3.1	9.7	3.13
13H-6, 20–20	116.60	3.1	10.0	3.23
13H-6, 70–70	117.10	3.0	11.6	3.87
13H-6, 120–120	117.60	3.0	12.3	4.10
14H-1, 20–20	118.60	3.0	10.8	3.60
14H-1, 70–70	119.10	3.0	11.2	3.73
14H-1, 120–120	119.60	3.0	10.8	3.60
14H-2, 20–20	120.10	3.0	9.4	3.13
14H-2, 70–70	120.60	3.0	10.3	3.43
14H-2, 120–120	121.10	3.0	9.8	3.27
14H-3, 120–120	122.60	3.0	10.0	3.33
14H-4, 20–20	123.10	3.0	9.6	3.20
14H-4, 70–70	123.60	3.0	10.2	3.40
14H-4, 120–120	124.10	3.0	10.0	3.33
15H-1, 20–20	128.10	3.0	13.1	4.37
15H-1, 70–70	128.60	3.0	12.5	4.17
15H-1, 120–120	129.10	3.0	11.9	3.97
15H-2, 70–70	130.10	3.0	11.7	3.90
15H-2, 120–120	130.60	3.0	11.1	3.70
15H-3, 20–20	131.10	3.0	11.9	3.97
15H-3, 70–70	131.60	3.0	12.1	4.03
15H-3, 120–120	132.10	3.0	12.7	4.23
15H-4, 20–20	132.60	3.1	13.5	4.35
15H-4, 70–70	133.10	3.1	12.0	3.87
15H-4, 120–120	133.60	3.0	13.0	4.33
16H-1, 20–20	137.60	3.0	11.1	3.70
16H-1, 70–70	138.10	3.0	11.9	3.97
16H-1, 120–120	138.60	3.0	12.4	4.13
16H-2, 70–70	139.60	3.0	13.0	4.33
16H-2, 120–120	140.10	3.0	15.9	5.30
16H-3, 20–20	140.60	3.0	16.1	5.37
16H-3, 70–70	141.10	3.0	14.4	4.80
16H-3, 120–120	141.60	3.0	14.9	4.97
16H-4, 20–20	142.10	3.0	17.6	5.87
16H-4, 70–70	142.60	3.0	17.5	5.83
17X-1, 20–20	146.10	3.0	15.7	5.23
17X-1, 70–70	146.60	3.0	14.0	4.67
17X-1, 120–120	147.10	3.0	13.8	4.60
17X-2, 20–20	147.60	3.0	12.8	4.27
17X-2, 70–70	148.10	3.0	16.1	5.37
17X-2, 120–120	148.60	3.0	14.3	4.77
17X-3, 20–20	149.10	3.0	11.8	3.93
17X-3, 120–120	150.10	3.0	11.5	3.83
17X-4, 20–20	150.60	3.0	13.0	4.33
17X-4, 120–120	151.60	3.0	11.4	3.80
17X-5, 20–20	152.10	3.0	12.0	4.00
17X-5, 70–70	152.60	3.0	11.8	3.93
17X-5, 120–120	153.10	3.0	11.9	3.97
17X-6, 20–20	153.60	3.0	13.0	4.33
17X-6, 70–70	154.10	3.0	13.8	4.60
17X-6, 120–120	154.60	3.0	14.8	4.93

Table 10. Vane shear strength data, Hole 821A.

Core, section, interval (cm)	Depth (mbsf)	Spring Number	Torque (degrees)	Strain (degrees)	Shear strength (kPa)
133-821A-					
1H-1, 92–93	0.92	4	5	5	5.9
1H-2, 92–93	2.42	4	7	10	8.3
1H-3, 72–73	3.72	4	6	12	7.1
2H-1, 92–93	5.32	4	8	12	9.5
2H-2, 92–93	6.82	4	6	9	7.1
2H-3, 92–93	8.32	4	7	12	8.3
2H-4, 92–93	9.82	4	9	11	10.7
2H-6, 89–90	12.79	4	14	12	16.7
3H-1, 89–90	14.79	4	14	12	16.7
3H-2, 89–90	16.29	4	12	12	14.3
3H-3, 90–91	17.80	4	10	16	11.9
3H-4, 90–91	19.30	4	19	20	22.6
3H-5, 90–91	20.80	4	17	17	20.2
3H-6, 90–91	22.30	4	22	16	26.2
4H-1, 90–91	24.30	4	19	19	22.6
4H-2, 90–91	25.80	4	16	18	19.0
4H-3, 90–91	27.30	4	21	20	25.0
4H-4, 90–91	28.80	4	21	15	25.0
4H-5, 90–91	30.30	4	19	15	22.6
4H-6, 90–91	31.80	4	21	14	25.0
5H-1, 81–82	33.71	4	15	17	17.8
5H-2, 90–91	35.30	4	17	23	20.2
5H-3, 90–91	36.80	4	10	26	11.9
5H-4, 90–91	38.30	4	16	15	19.0
5H-5, 90–91	39.80	4	27	14	32.1
5H-6, 90–91	41.30	4	27	21	32.1
6H-1, 91–92	43.31	4	34	17	40.4
6H-2, 91–92	44.81	4	41	18	48.8
6H-3, 91–92	46.31	4	39	16	46.4
6H-4, 91–92	47.81	4	48	21	57.1
6H-5, 91–92	49.31	4	51	13	60.7
6H-6, 91–92	50.81	4	47	12	55.9
7H-1, 91–92	52.81	4	41	17	48.8
7H-2, 91–92	54.31	4	52	16	61.8
7H-3, 91–92	55.81	4	10	11	11.9
7H-4, 91–92	57.31	4	42	22	50.0
7H-5, 92–93	58.82	4	61	17	72.5
7H-6, 92–93	60.32	4	65	16	77.3
8H-1, 91–92	62.31	4	58	16	69.0
8H-2, 91–92	63.81	4	52	16	61.8
8H-3, 91–92	65.31	4	46	13	54.7
8H-4, 91–92	66.81	4	54	16	64.2
8H-5, 91–92	68.31	4	37	21	44.0
8H-6, 91–92	69.81	4	86	17	102.3
9H-1, 91–92	71.81	4	54	15	64.2
9H-2, 91–92	73.31	4	15	11	17.8
9H-3, 91–92	74.81	4	25	17	29.7
9H-4, 91–92	76.31	4	28	19	33.3
9H-5, 91–92	77.81	4	39	15	46.4
9H-6, 91–92	79.31	4	44	15	52.3
10H-1, 91–92	81.31	4	53	15	63.0
10H-2, 91–92	82.81	4	58	18	69.0
10H-3, 91–92	84.31	4	70	15	83.3
10H-4, 91–92	85.81	4	48	17	57.1
10H-5, 91–92	87.31	4	62	13	73.7
10H-6, 91–92	88.81	4	77	13	91.6
11H-1, 88–89	90.78	4	9	12	10.7
11H-2, 88–89	92.28	4	26	10	30.9
11H-3, 88–89	93.78	4	50	18	59.5
11H-4, 88–89	95.28	4	48	18	57.1
11H-5, 88–89	96.78	4	29	18	34.5
11H-6, 88–89	98.28	4	15	9	17.8
12H-1, 94–95	100.34	4	55	16	65.4
12H-2, 94–95	101.84	4	22	13	26.2
12H-3, 94–95	103.34	4	63	16	74.9
12H-4, 93–94	104.83	4	55	16	65.4
12H-5, 93–94	106.33	4	24	15	28.5
12H-6, 96–97	107.86	4	25	16	29.7
13H-1, 96–97	109.86	4	38	16	45.2
13H-2, 96–97	111.36	4	42	16	50.0
13H-4, 96–97	114.36	4	45	13	53.5
13H-5, 96–97	115.86	4	19	15	22.6
13H-6, 96–97	117.36	4	27	10	32.1
14H-1, 96–97	119.36	4	20	18	23.8

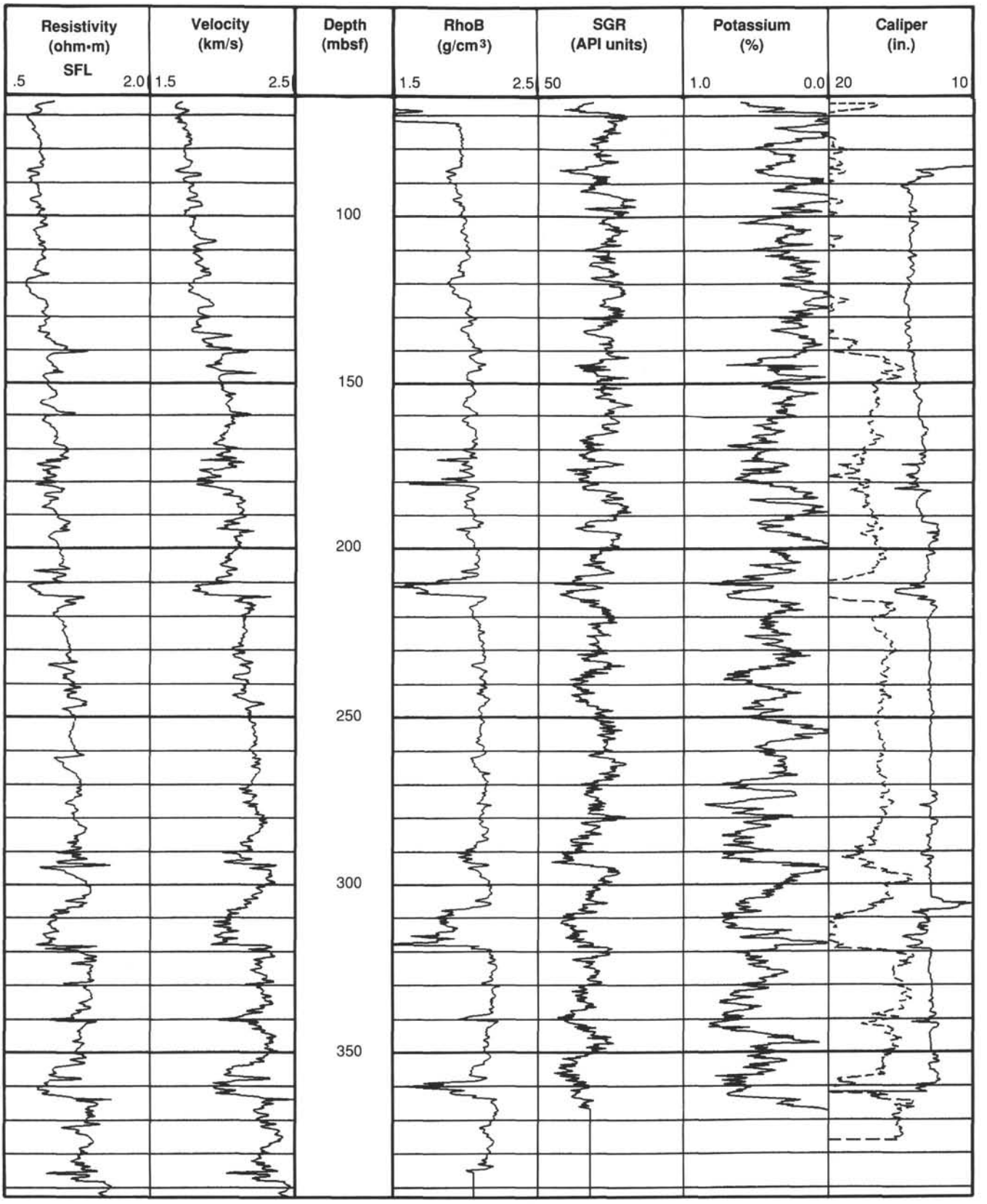

Figure 27. Comparison of porosity-sensitive logs (resistivity, velocity, and bulk density) to logs sensitive to clay-mineral content (SGR gamma ray and potassium). Calipers shown are from the mechanical caliper device (solid line) and sonic caliper (dashed line); both are less reliable than the calipers of Figure 28.

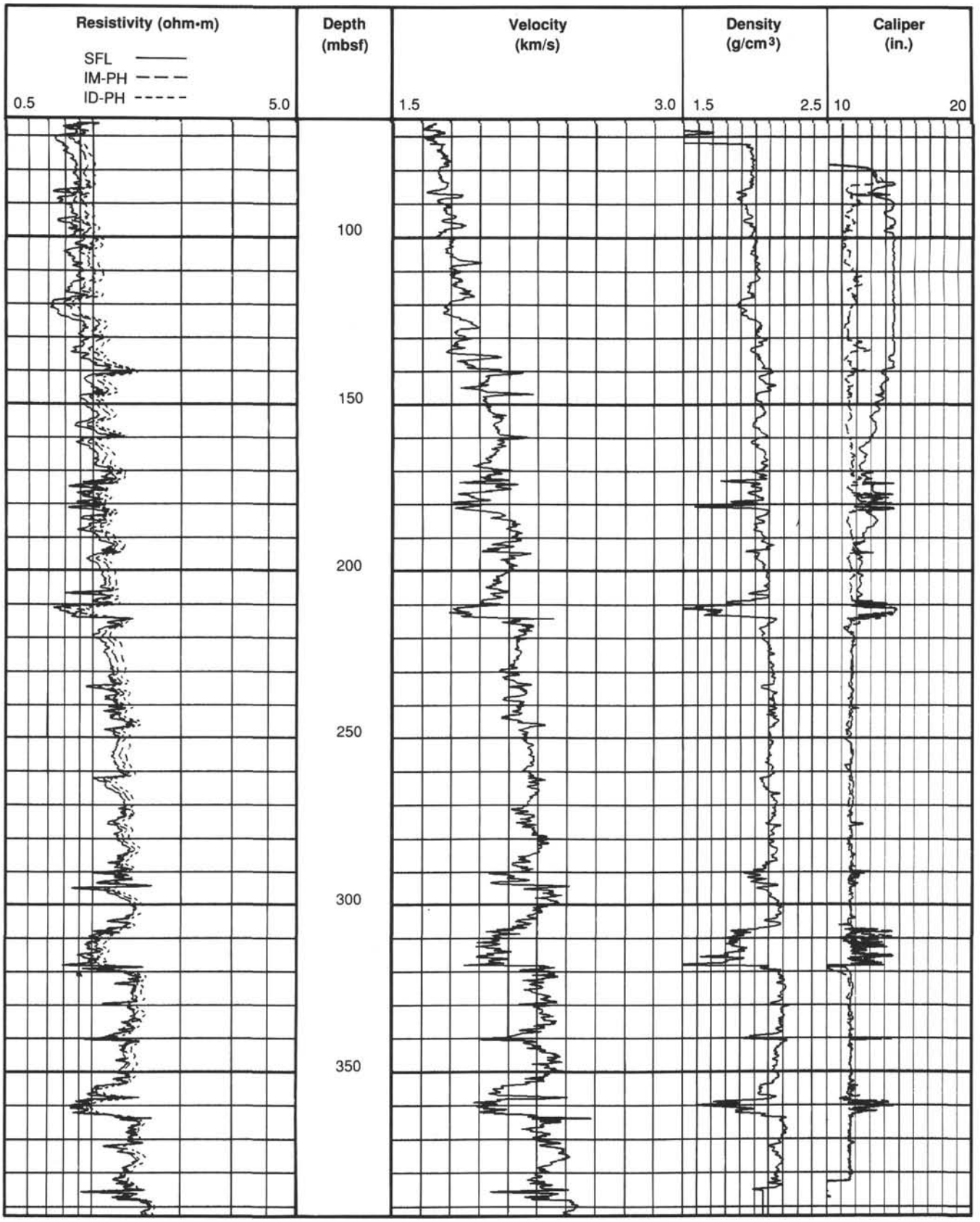

Figure 28. Porosity-sensitive logs obtained by the seismic stratigraphic tool string at Hole 821A. The calipers shown are from the FMS. Density lows are probably artifacts caused by poor pad contact in washed-out intervals.

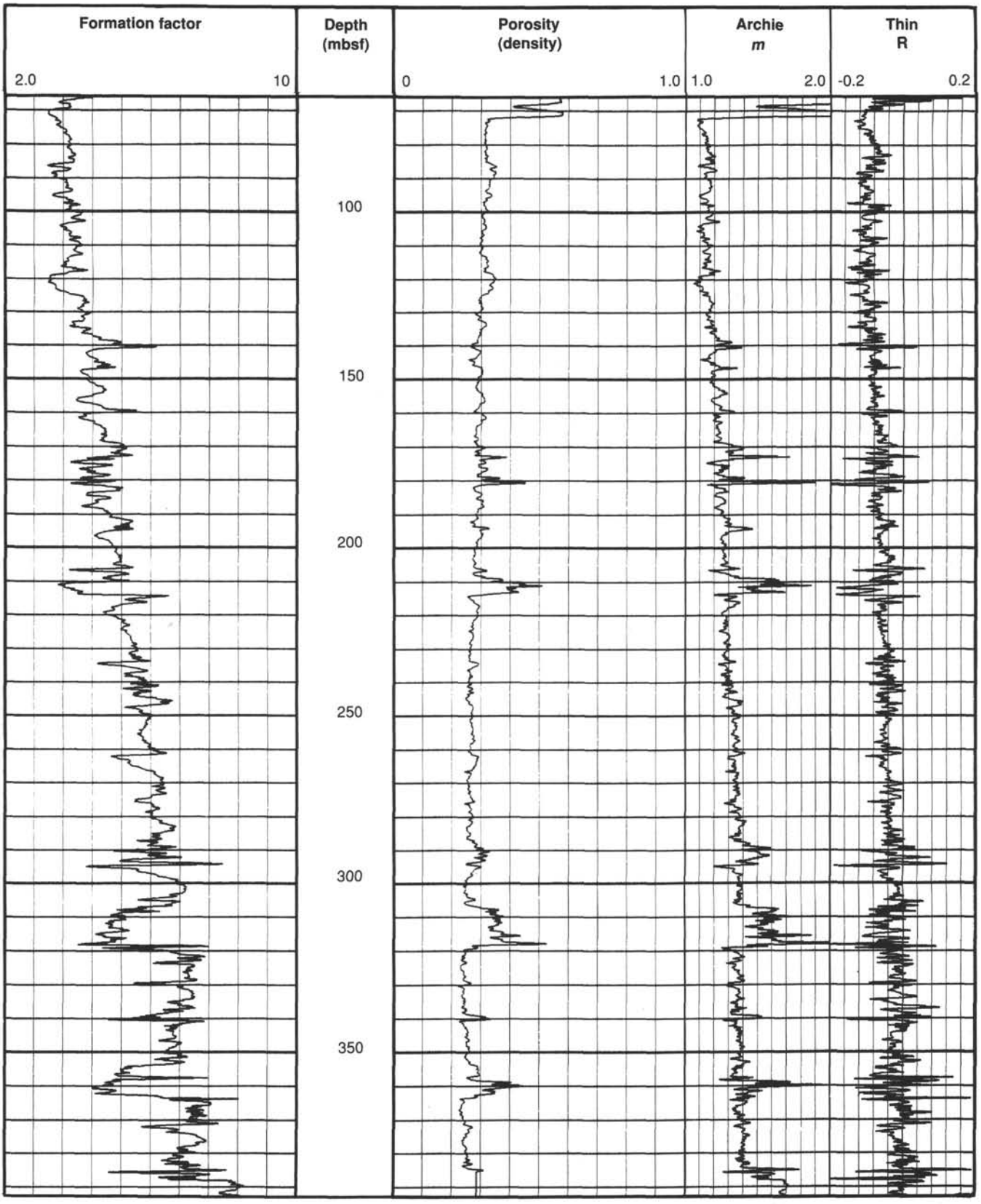

Figure 29. Site 821 logs of FF (from the ratio of formation resistivity to fluid resistivity), porosity (from the density log), the Archie component *m* relating FF to porosity, and the parameter "Thin R," which responds to thin-bed effects.

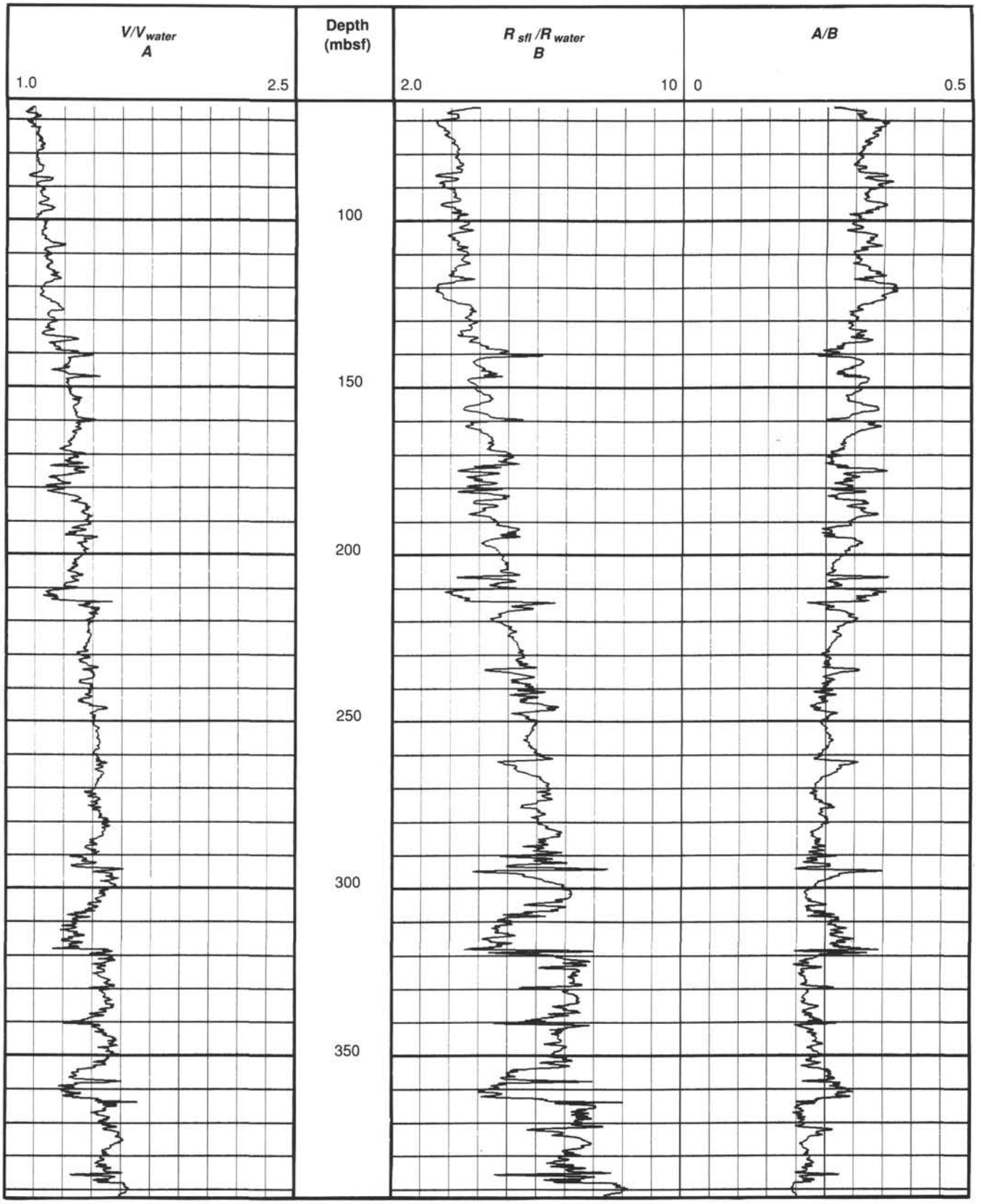

Figure 30. Velocity and resistivity logs for Hole 821A, plotted as ratios to each other and to water to highlight changes in pore geometry.

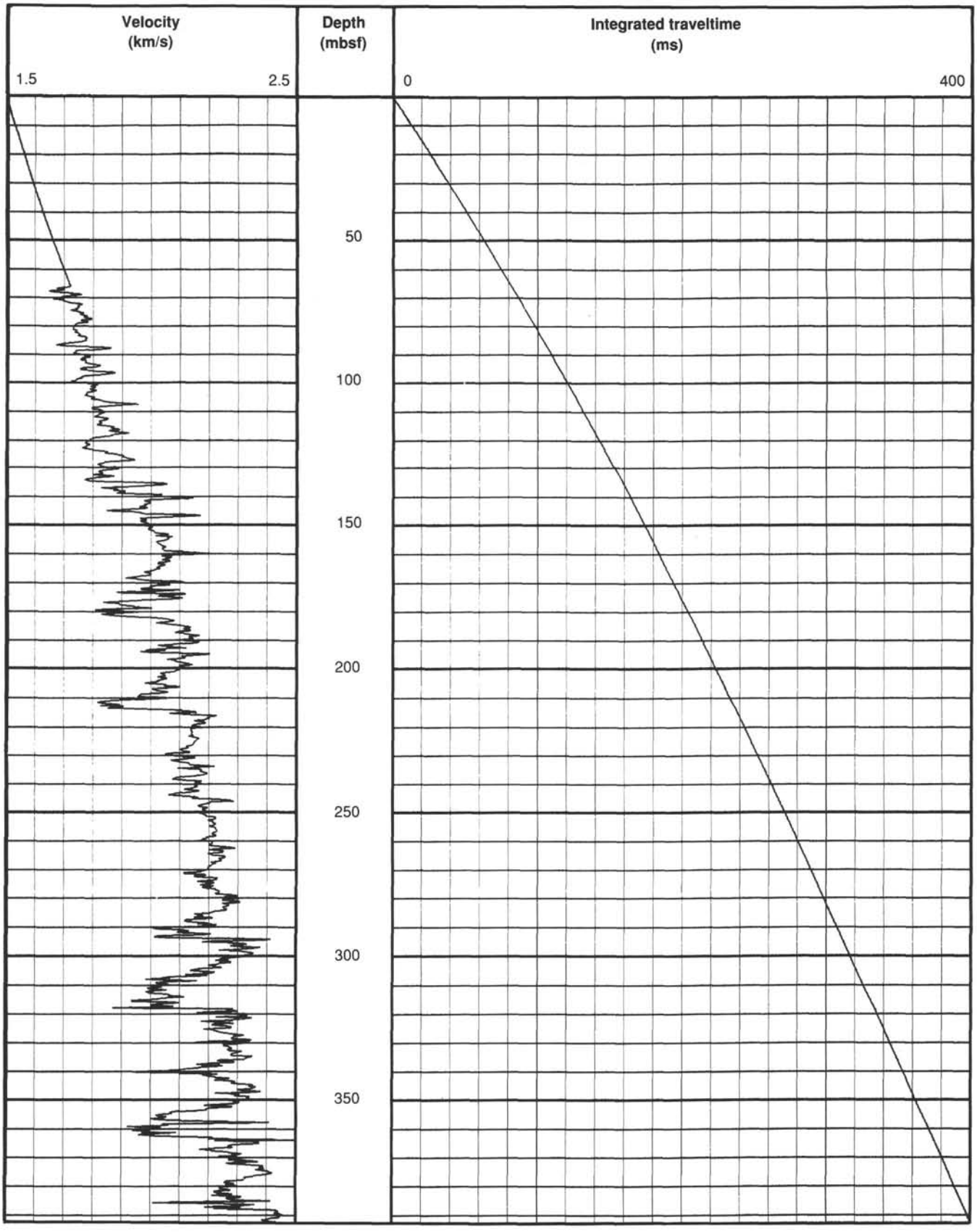

Figure 31. Velocity log, and the integrated two-way traveltime function that it implies, for matching of core-based information from Site 821 with the seismic sections across the site.

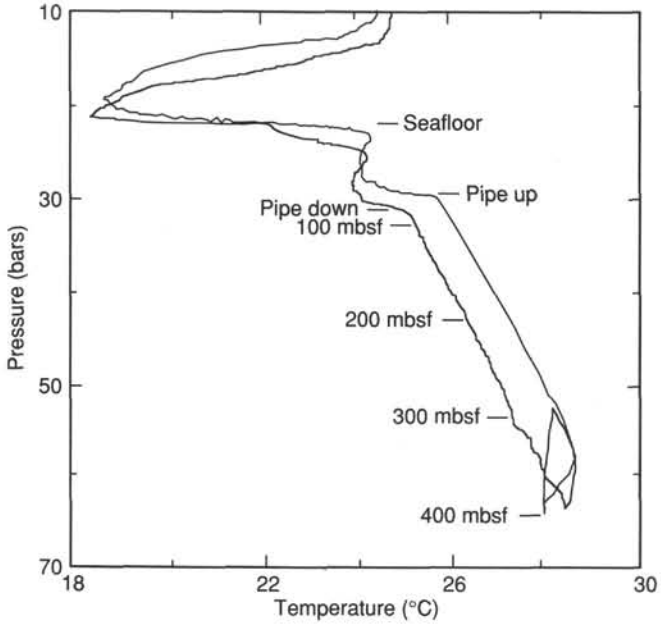

Figure 32. Temperature log as a function of pressure (or depth) for Site 821.

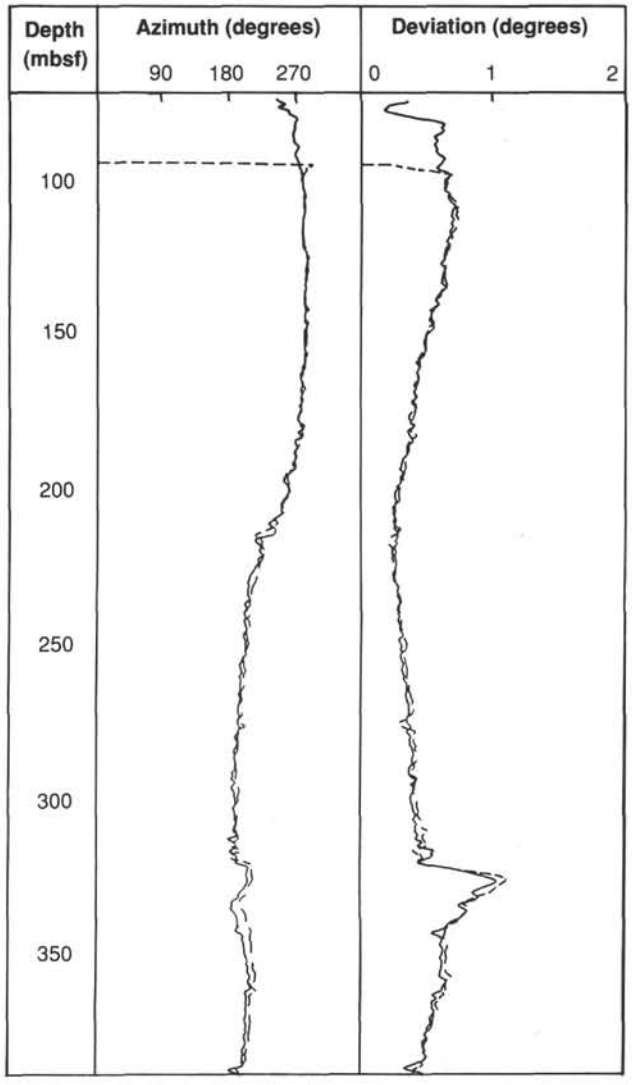

Figure 33. Hole deviation and its azimuth at Hole 821A.

Hole 821A: Resistivity-Sonic-Natural Gamma Ray Log Summary

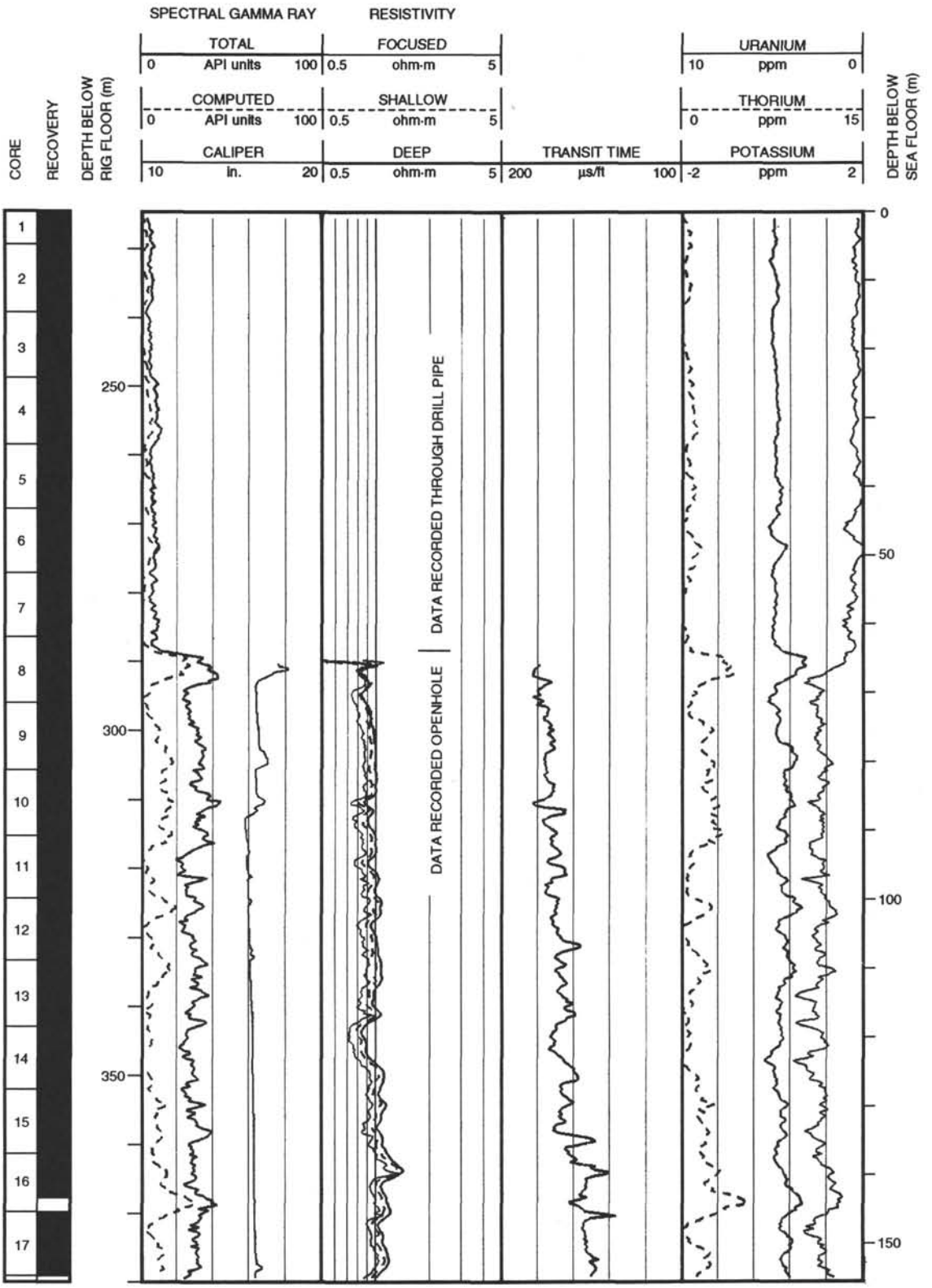

Hole 821A: Resistivity-Sonic-Natural Gamma Ray Log Summary (continued)

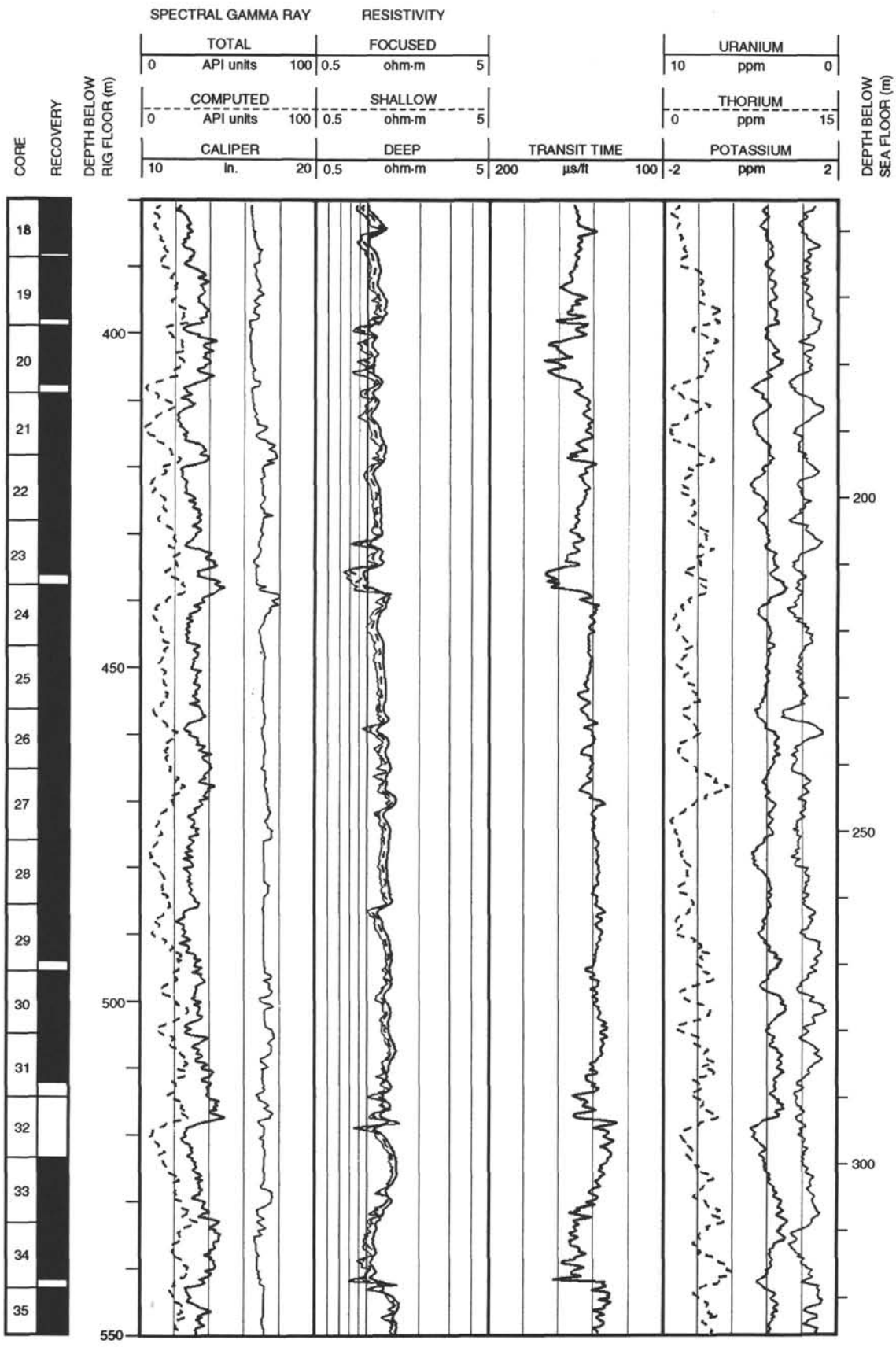

Hole 821A: Resistivity-Sonic-Natural Gamma Ray Log Summary (continued)

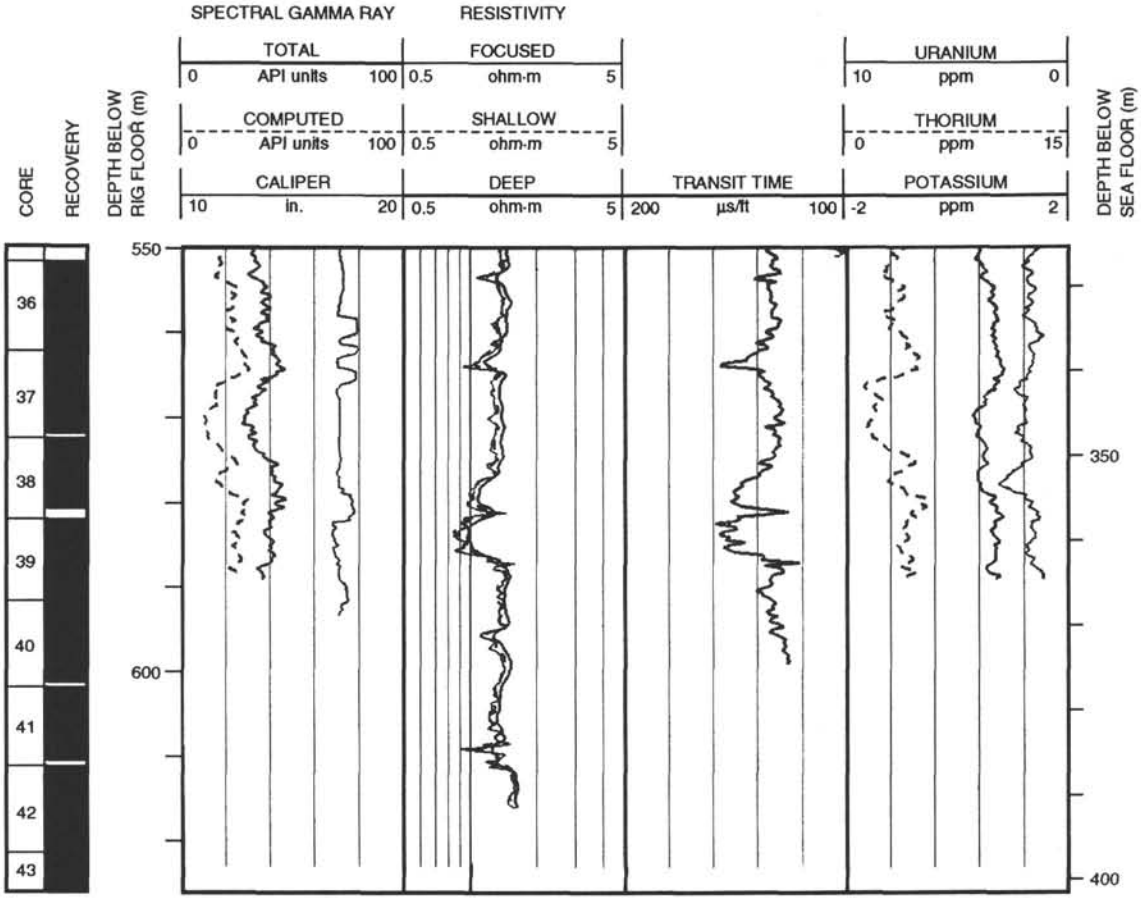

Hole 821A: Density-Natural Gamma Ray Log Summary

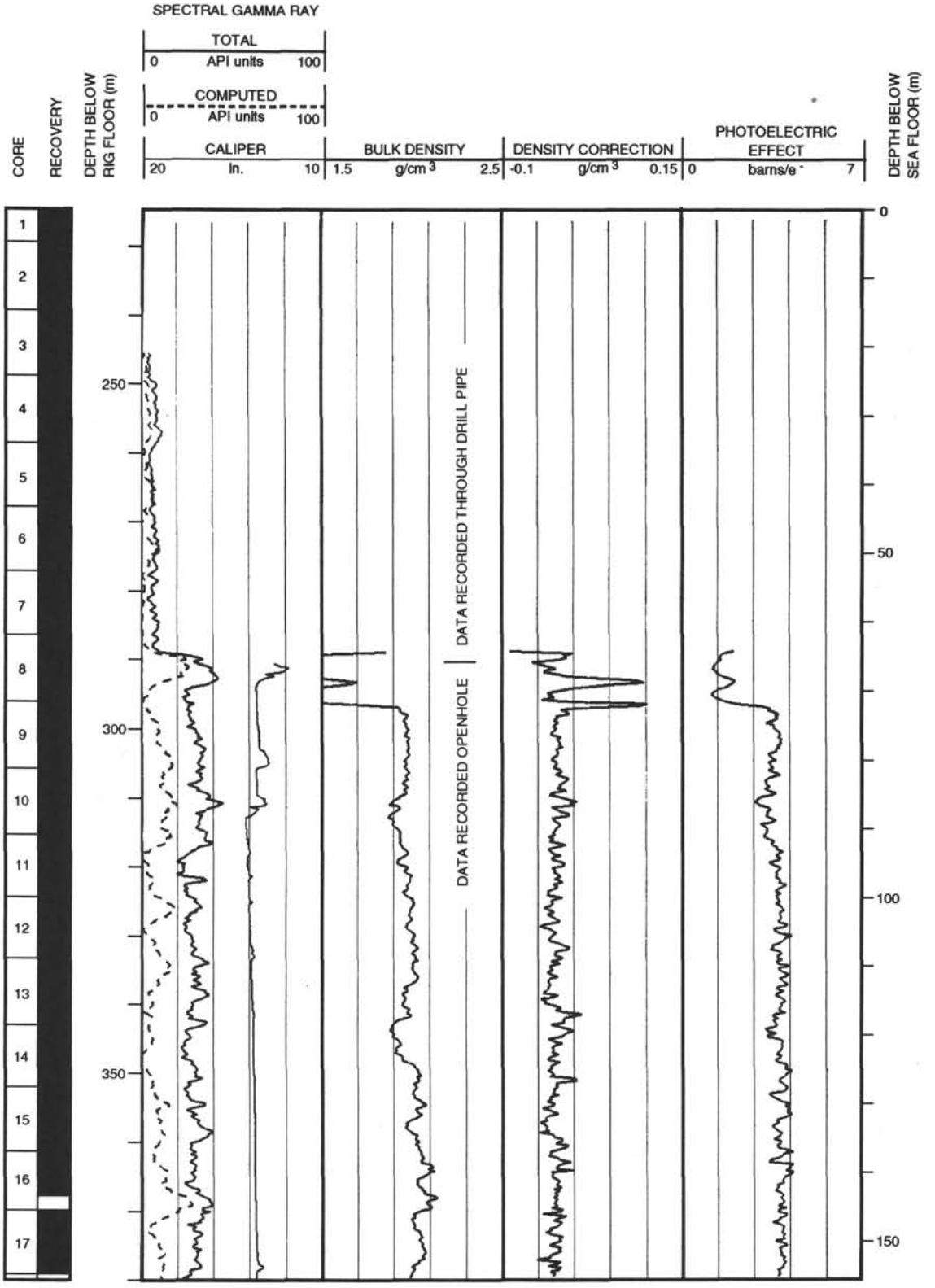

Hole 821A: Density-Natural Gamma Ray Log Summary (continued)

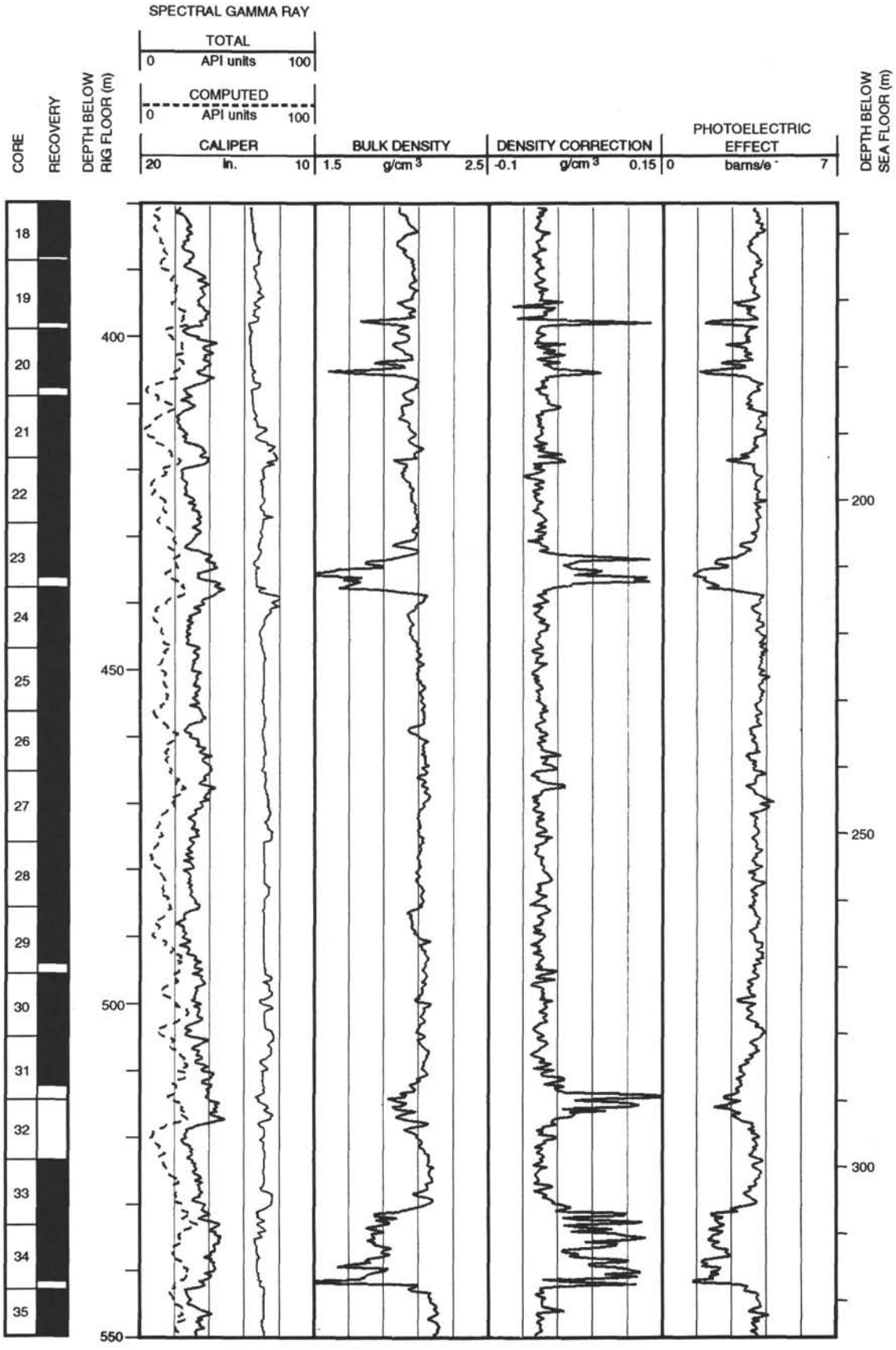

Hole 821A: Density-Natural Gamma Ray Log Summary (continued)